



Time Domain Version of the Uniform Geometrical Theory of Diffraction

P.R. Rousseau and P.H. Pathak

The Ohio State University

ElectroScience Laboratory

Department of Electrical Engineering
Columbus, Ohio 43212

Technical Report 721564-3
Contract No. N00014-89-J-1007 P00008
February 1996

Department of the Navy
Office of Naval Research
800 N. Quincy St.
Arlington, VA 22217-5000

19960325 127

DTIC QUALITY INSPECTED 5

NOTICES

When Government drawings, specifications, or other data are used for any purpose other than in connection with a definitely related Government procurement operation, the United States Government thereby incurs no responsibility nor any obligation whatsoever, and the fact that the Government may have formulated, furnished, or in any way supplied the said drawings, specifications, or other data, is not to be regarded by implication or otherwise as in any manner licensing the holder or any other person or corporation, or conveying any rights or permission to manufacture, use, or sell any patented invention that may in any way be related thereto.

REPORT DOCUMENTATION PAGE	1. REPORT NO.	2.	3. Recipient's Accession No.
4. Title and Subtitle Time Domain Version of the Uniform Geometrical Theory of Diffraction		5. Report Date February 1996	
7. Author(s) P.R. Rousseau and P.H. Pathak		8. Performing Org. Rept. No. 721564-3	
9. Performing Organization Name and Address The Ohio State University ElectroScience Laboratory 1320 Kinnear Road Columbus, OH 43212		10. Project/Task/Work Unit No.	
		11. Contract(C) or Grant(G) No. (C) N00014-89-J-1007 P00008 (G)	
12. Sponsoring Organization Name and Address Department of the Navy, Office of Naval Research 800 N. Quincy St. Arlington, VA 22217-5000		13. Report Type/Period Covered Technical Report	
		14.	
15. Supplementary Notes			
16. Abstract (Limit: 200 words) <p>A time domain (TD) version of the uniform geometrical theory of diffraction which is referred to as the TD-UTD is developed to analyze the transient electromagnetic scattering from perfectly conducting objects that are large in terms of pulse width. In particular, the scattering from a perfectly conducting arbitrary curved wedge and an arbitrary smooth convex surface are treated in detail. Note that the canonical geometries of a circular cylinder and a sphere are special cases of the arbitrary smooth convex surface. These TD-UTD solutions are obtained in the form of relatively simple analytical expressions valid for early to intermediate times. The geometries treated here can be used to build up a transient solution to more complex radiating objects via space-time localization, in exactly the same way as is done by invoking spatial localization properties in the frequency domain UTD. The TD-UTD provides the response due to an excitation of a general astigmatic impulsive wavefront with any polarization. This generalized impulse response may then be convolved with other excitation time pulses, to find even more general solutions due to other excitation pulses. Since the TD-UTD uses the same rays as the frequency domain UTD, it provides a simple picture for transient radiation or scattering and is therefore just as physically appealing as the frequency domain UTD.</p> <p>The formulation of an analytic time transform (ATT), which produces an analytic time signal given a frequency response function, is given here. This ATT is used because it provides a very efficient method of inverting the asymptotic high frequency UTD representations to obtain the corresponding TD-UTD expressions even when there are special UTD transition functions which may not be well behaved at the low frequencies; also, using the ATT avoids the difficulties associated with the inversion of UTD ray fields that traverse line or smooth caustics. Another useful aspect of the ATT is the ability to perform an efficient convolution with a broad class of excitation pulse functions, where the frequency response of the excitation function must be expressed as a summation of complex exponential functions.</p>			
17. Document Analysis a. Descriptors <div style="display: flex; justify-content: space-between;"> <div> ASYMPTOTIC ELECTROMAGNETIC PULSE </div> <div> SCATTERING UTD (UNIFORM THEORY OF DIFFRACTION) </div> </div> b. Identifiers/Open-Ended Terms c. COSATI Field/Group			
18. Availability Statement A. Approved for public release; Distribution is unlimited.		19. Security Class (This Report) Unclassified	21. No. of Pages 163
		20. Security Class (This Page) Unclassified	22. Price

Contents

List of Figures	v
List of Tables	ix
1 Introduction	1
2 Analytic Time Functions	9
2.1 Definitions	11
2.2 Properties of the Analytic Time Transform (ATT)	16
2.2.1 Properties of Analytic Time Functions for Real Time	16
2.3 Some Important Analytic Time Functions	18
2.4 Representations of Analytic Time Functions	19
2.4.1 Analytic Time Transform of Low Frequency Power Series	21
2.4.2 Analytic Time Transform of High Frequency Asymptotic Series	21
2.4.3 Example: The TD-UTD Edge Diffraction Transition Function	26
2.5 Efficient Time Convolution	30
3 TD-UTD for a Curved Wedge	32
3.1 The Frequency Domain UTD Solution for Scattering from a Curved Wedge	34
3.1.1 The Frequency Domain Geometrical Optics (GO) Fields	35
3.1.2 The Frequency Domain UTD Edge Diffracted Field	37
3.1.3 The Frequency Domain UTD Slope Edge Diffraction	37
3.2 The TD-UTD Impulse Response for a PEC Curved Wedge	40
3.2.1 The TD-UTD Geometrical Optics Field	40
3.2.2 The TD-UTD Edge Diffracted Field	42
3.2.3 The TD-UTD Slope Diffraction	47
3.3 Some Numerical Examples	49
3.4 Conclusions	63
4 TD-UTD for a Smooth Convex Surface	67
4.1 General Formulation in the Frequency Domain	71
4.2 Deep Lit Region	75
4.3 Deep Shadow Region	76
4.4 Observer Near the Shadow Boundary	77
4.5 Uniform TD-UTD Surface Diffraction	79

4.6 Numerical Example	81
4.7 Conclusions	82
5 Conclusions	94
A Synthesis of an Arbitrary Finite Energy Time Pulse for Efficient Convolution	99
APPENDICES	
B Exact Time Domain Field of an Arbitrarily Oriented Electric or Magnetic Dipole in the Presence of a Perfectly Conducting Wedge	101
B.1 Electric Dipole Case	101
B.2 Magnetic Dipole Case	107
C Derivation of Two TD-UTD Slope Diffraction Coefficients, One Based on Veruttipong's Work and the Other on Hwang's Work	111
C.1 Hwang's Slope Diffraction Coefficient	112
C.2 Veruttipong's Slope Diffraction Coefficient	114
D Computation of the Time Domain Creeping Wave Function	117
D.1 Definitions and Properties	117
D.2 Numerical Algorithm	121
E Computation of Special Function Used in TD-UTD Surface Diffraction	132
E.1 Shadow Region	133
E.2 Lit Region	137
E.3 Numerical Algorithm	142
Bibliography	149

List of Figures

2.1	Diagram showing the relationship between the Laplace transform (LT), Fourier transform (FT) and analytic time transform (ATT). Notice that $F(t)$ can be obtained directly from an inverse Laplace transform only if $F(t)$ is one-sided since the one-sided Laplace transform is used here.	15
3.1	An incident geometrical optics (GO) ray tube.	35
3.2	A reflected geometrical optics (GO) ray.	36
3.3	Coordinate systems for the TD-UTD dyadic diffraction coefficient. . .	38
3.4	Two dimensional parabolic strip geometry. The focus is located at $F(x=0, z=4)$, the width of the aperture is 8, and the observation point is $P(x=4, z=8)$. All linear dimensions are in centimeters.	53
3.5	The TD-UTD scattered field at the observation point P when the 2-D parabolic strip in Figure 5 is excited by an impulsive plane wave. The time axis is shifted by ρ/c for convenience where ρ is the distance of P from the origin and c is the speed of light.	53
3.6	The impulse response for each scattering mechanism is plotted here separately, where $E^r(t)$, $E^{d1}(t)$ and $E^{d2}(t)$ correspond to the impulse response of the reflected ray, the edge-diffracted ray from edge (1) and the edge-diffracted ray from edge (2), respectively. The time axis is shifted by ρ/c for convenience.	54
3.7	Same as in Figure 6 except that the incident temporal excitation is a finite energy time waveform.	54
3.8	A waterfall plot showing the space-time behavior of the total field when an electric dipole illuminates a PEC wedge. The observer is in the far zone and the incident field at the edge is rapidly varying so slope diffraction is significant.	56
3.9	A waterfall plot showing the space-time behavior of the first order diffracted field when an electric dipole illuminates a PEC wedge and the observer is in the far zone. The field here is multiplied by a factor of 10 as compared with Figure 3.8.	57
3.10	A waterfall plot showing the space-time behavior of the slope diffracted field (Hwang's version) when an electric dipole illuminates a PEC wedge. The observer is in the far zone. The field here is multiplied by a factor of 10 as compared with Figure 3.8.	58

3.11	The TD-UTD impulse response is compared with an exact result. The infinitesimal electric current has a unit step time behavior which approximately illuminates the wedge with an impulsive spherical wave. .	59
3.12	The TD-UTD impulse response is compared with an exact result. The infinitesimal electric current has a unit step time behavior which approximately illuminates the wedge with an impulsive spherical wave. The slope diffraction is zero when the dipole is oriented perpendicular to the incident direction.	60
3.13	The two versions of the TD-UTD slope diffraction are compared with an exact result. The infinitesimal electric current has a unit step time behavior which approximately illuminates the wedge with an impulsive spherical wave.	61
3.14	The two versions of the TD-UTD slope diffraction are compared with an exact result. The infinitesimal electric current has a unit step time behavior which approximately illuminates the wedge with an impulsive spherical wave.	62
3.15	The two versions of the TD-UTD slope diffraction are compared with an exact result. The infinitesimal magnetic current has a unit step time behavior which approximately illuminates the wedge with an impulsive spherical wave.	64
3.16	The two versions of the TD-UTD slope diffraction are compared with an exact result. The infinitesimal magnetic current has a unit step time behavior which approximately illuminates the wedge with an impulsive spherical wave.	65
4.1	Geometry of the smooth surface scattering situation where the source and observer are off the surface.	72
4.2	Ray vectors for surface diffraction.	73
4.3	Excitation pulse $w(t)$ and corresponding frequency response (or frequency window) $W(f)$ used for the scattering from a 2-D cylinder example.	82
4.4	Comparison of the TD-UTD solution and an eigenfunction reference solution (eigen) which is transformed into time domain with the IFFT after the window in Figure 4.3 is applied. The far zone backscatter from a 2-D circular cylinder, for TE_z (hard) polarization and the radius is $r = 1$ meter.	83
4.5	Comparison of the TD-UTD versus a reference eigenfunction solution ("eigen") which is transformed into the time domain with the IFFT after the window in Figure 4.3 is applied. The far zone bistatic scattering (at bistatic angle $\psi = 90^\circ$) from 2-D cylinder, for TE_z (hard) polarization and radius $r = 1$ meter.	84

4.6	Comparison of the TD-UTD versus a reference eigenfunction solution ("eigen") which is transformed into the time domain with the IFFT after the window in Figure 4.3 is applied. The far zone bistatic scattering (at bistatic angle $\psi = 135^\circ$) from 2-D cylinder, for TE_z (hard) polarization and radius $r = 1$ meter.	85
4.7	Comparison of the TD-UTD versus a reference eigenfunction solution ("eigen") which is transformed into the time domain with the IFFT after the window in Figure 4.3 is applied. The far zone bistatic scattering (at bistatic angle $\psi = 165^\circ$) from 2-D cylinder, for TE_z (hard) polarization and radius $r = 1$ meter.	86
4.8	Comparison of the TD-UTD versus a reference eigenfunction solution ("eigen") which is transformed into the time domain with the IFFT after the window in Figure 4.3 is applied. The far zone bistatic scattering (at bistatic angle $\psi = 175^\circ$) from 2-D cylinder, for TE_z (hard) polarization and radius $r = 1$ meter.	87
4.9	Comparison of the TD-UTD versus a reference eigenfunction solution ("eigen") which is transformed into the time domain with the IFFT after the window in Figure 4.3 is applied. The far zone backscatter from 2-D cylinder, for TM_z (soft) polarization and radius $r = 1$ meter.	88
4.10	Comparison of the TD-UTD versus a reference eigenfunction solution ("eigen") which is transformed into the time domain with the IFFT after the window in Figure 4.3 is applied. The far zone bistatic scattering (bistatic angle $\psi = 90^\circ$) from 2-D cylinder, for TM_z (soft) polarization and radius $r = 1$ meter.	89
4.11	Comparison of the TD-UTD versus a reference eigenfunction solution ("eigen") which is transformed into the time domain with the IFFT after the window in Figure 4.3 is applied. The far zone bistatic scattering (bistatic angle $\psi = 135^\circ$) from 2-D cylinder, for TM_z (soft) polarization and radius $r = 1$ meter.	90
4.12	Comparison of the TD-UTD versus a reference eigenfunction solution ("eigen") which is transformed into the time domain with the IFFT after the window in Figure 4.3 is applied. The far zone bistatic scattering (bistatic angle $\psi = 165^\circ$) from 2-D cylinder, for TM_z (soft) polarization and radius $r = 1$ meter.	91
4.13	Comparison of the TD-UTD versus a reference eigenfunction solution ("eigen") which is transformed into the time domain with the IFFT after the window in Figure 4.3 is applied. The far zone bistatic scattering (bistatic angle $\psi = 175^\circ$) from 2-D cylinder, for TM_z (soft) polarization and radius $r = 1$ meter.	92
B.1	An electric (or magnetic) dipole radiating in the presence of a PEC wedge. The dipole is in the $z = 0$ plane but the observer may be out of this plane.	102

D.1	Comparison between a numerical calculation of the real part of the creeping wave time function in (D.1) ("Exact") and the asymptotic early time approximation in (D.7) ("Asymptotic"), where $\alpha = 1$. . .	119
D.2	The integration contour in the complex y plane. The shaded regions are valleys where the integral in (D.18) is convergent and the saddle points at $y = \pm 1$ are shown. The ϕ in this figure is the phase angle of the complex time variable $t = t e^{j\phi}$	122
D.3	The slowly varying factor in the integrand of $\tilde{I}_1(t)$ in (D.34), where $B = 2.7$	125
D.4	The time domain creeping wave function $\tilde{F}_{cw}^+(\alpha, t)$ when $\alpha = 1$, plotted for $t \in [-10, 10]$	129
D.5	The time domain creeping wave function $\tilde{F}_{cw}^+(\alpha, t)$ when $\alpha = 1$, plotted for $t \in [-1, 1]$	130
D.6	The time domain creeping wave function $\tilde{F}_{cw}^+(\alpha, t)$ when $\alpha = 1$, plotted for $t \in [-0.1, 0.1]$	131
E.1	The special function $\tilde{F}_h^{+P}(\Xi, t)$ when the observer is in the shadow region and $\Xi = 1$. The polarization is hard. Comparison between (a) the "early time" creeping wave mode series in (E.5) and (b) the "late time" representation in (E.17) with (E.18).	145
E.2	The special function $\tilde{F}_s^{+P}(\Xi, t)$ when the observer is in the shadow region and $\Xi = 1$. The polarization is soft. Comparison between (a) the "early time" creeping wave mode series in (E.5) (plus $-\pi^{-0.5}$ times (E.33)) and (b) the "late time" representation in (E.17) with (E.18). .	146
E.3	The special function $\tilde{F}_s^{+P}(\Xi, t)$ when the observer is in the lit region and $\Xi = -1$. The polarization is soft. Comparison between (a) the "early time" representation in (E.25) and (b) the "late time" representation in (E.17) with (E.18).	147
E.4	The special function $\tilde{F}_h^{+P}(\Xi, t)$ when the observer is in the lit region and $\Xi = -1$. The polarization is hard. Comparison between (a) the "early time" representation in (E.25) and (b) the "late time" representation in (E.17) with (E.18).	148

List of Tables

2.1	Properties of the analytic time transform (ATT)	16
2.2	Properties of the Hilbert transform. The Hilbert transform of $F(t)$ is denoted by $\mathcal{H}F(t)$ or $\hat{F}(t)$ and similarly for $G(t)$	17
2.3	Relationship between some Laplace domain functions, $\tilde{F}(s)$ and corresponding frequency (or Fourier) domain functions, $\tilde{F}(\omega)$	19
2.4	The analytic time transform (ATT) of some useful functions. In this table, n is a non-negative integer, $\mu > -1$ is not an integer, and η is not an integer.	20
D.1	The exponential factors for the series of exponentials approximation to the $g(u)$ function in (D.40). These parameters are the result from using the extended Prony's method with 100 sample points.	127
D.2	Coefficients for the series of exponentials approximation to the $g(u)$ function in (D.40). These parameters are the result from using the extended Prony's method with 100 sample points.	128
E.1	Zeros of the Airy function and associated values of the Airy function.	134
E.2	Constants used in the power series expansion of the Pekeris functions $p(x)$ and $q(x)$ and therefore also in the expansion of $\tilde{F}_{p,q}(\Xi, \omega)$ and $\tilde{F}_{p,q}^+(\Xi, t)$	135
E.3	Coefficients $\{B_n^s\}$ used in the early time representation in (E.25) used in the lit region $\Xi < 0$ and for soft polarization	140
E.4	Coefficients $\{B_n^h\}$ used in the early time representation in (E.25) used in the lit region $\Xi < 0$ and for hard polarization	141

Chapter 1

Introduction

A time domain version of the uniform geometrical theory of diffraction (UTD), henceforth abbreviated as TD-UTD, is developed in this study for describing in relatively simple form the transient radiation and scattering from a class of perfectly conducting configurations when they are excited by an electromagnetic pulse. In particular, a TD-UTD formulation is obtained for describing the scattering from an arbitrary curved wedge, and also the scattering from an arbitrary convex surface. Due to the fact that the TD-UTD is developed via an analytical inversion into the time domain (TD) of the corresponding high frequency asymptotic results obtained previously in the frequency domain based UTD, the TD-UTD therefore provides an “early time” asymptotic representation that is valid close to the arrival times of each of the various wave fronts. More specifically, each term in the TD-UTD formulation is asymptotically valid at and near a particular arrival time associated with the path length of the corresponding ray (i.e. incident ray, reflected ray, diffracted ray, etc.) which contributes at a given observation point. Due to this “early time” asymptotic nature of the TD-UTD representation, each TD ray field may not have a causal impulse response since there may be information in the time domain occurring after and before the arrival time of the ray. This is an important observation since earlier attempts at the interpretation of approximate impulse responses of scattering targets did not fully understand the possible non-causal nature of “early time” solutions [1]. Since the TD-UTD employs the same rays as the corresponding frequency domain UTD,

it provides a clear physical picture for radiation and scattering in exactly the same manner as does the UTD on which it is based.

The development of the TD-UTD is based on an integral transform which is called the analytic time transform (ATT) in this report. The ATT is a one-sided transform which transforms a frequency domain function (which is a function of a real frequency variable ω) into an analytic time function which is analytic in the upper half time plane ($\text{Im}(t) > 0$). By construction, the real part of the analytic time function when evaluated for real time ($\text{Im}(t) = 0$) is exactly the inverse Fourier transform of the frequency domain function whenever the frequency domain function obeys the conjugate symmetry relationship ($\tilde{F}(-\omega) = \tilde{F}^*(\omega)$) which guarantees that the inverse Fourier transform is a real time function. The imaginary part of the analytic time function is the Hilbert transform of the real part as expected from complex function theory since the analytic time function is analytic in the upper half time plane.

The ATT is developed because the traditional Fourier transform and Laplace transform are not convenient for transforming the asymptotic high frequency UTD results into the time domain. The main reason for the difficulty in using the traditional Fourier or Laplace transforms on the frequency domain UTD results lies in the fact that the resulting time functions may not be one-sided (i.e. may not be causal). Such a difficulty can occur for even the simplest of examples, such as an incident geometrical optics ray which is reflected from a smooth concave surface and passes through one caustic before reaching the observer. The reflected ray field after the caustic has an extra factor of $e^{j\pi/2}$ in the frequency domain which makes the use of the conventional inverse Laplace or Fourier transforms inconvenient. In principle, a two-sided Laplace transform or a Fourier transform can be used to derive the results in this report, but would require a much greater effort and the resulting time domain formulas would have been much more complicated.

In addition to the convenience of using the ATT on the frequency domain UTD results, there is the added benefit of the ability of performing efficient convolutions with a broad class of excitation pulses. An algorithm is developed to convolve any analytic time function obtained by using the ATT with an excitation with a frequency

response which can be written as a series of complex exponentials. This is a very general description of an excitation pulse, but it is especially useful when the pulse has a narrow temporal width and a broad banded frequency response. When this is the case, the excitation pulse can be modeled with only a few basis functions (around 10 or 15 basis functions for many practical cases) and the convolution is a simple summation over a few terms.

Although the term "UTD" encompasses a number of different asymptotic solutions for various special geometries, only two specific but most often required geometries are analyzed here; namely, an arbitrary curved wedge, and an arbitrary smooth convex surface. These geometries can be used to build up the solution to a more general complex configuration (in terms of wedges, plates, and cylinders or ellipsoids, etc.) when the standard assumption of localization of UTD fields is invoked. A TD-UTD formulation for the transient scattering from a pulse excited general curved wedge is accomplished by applying the ATT to the well understood frequency domain UTD formulas that have been obtained previously by Kouyoumjian and Pathak [2]. In particular, the transient response of the various ray mechanisms—such as incident, reflected and diffracted rays—is explicitly obtained in closed form when the excitation is a time impulsive, general astigmatic wavefront. There are explicit and easy to calculate formulas for the TD-GO rays, both incident and reflected, for the first order diffracted ray and also for the slope diffracted ray. The slope diffraction contribution is important when the incident field at the edge is rapidly varying with respect to space (not time). Likewise, the TD-UTD solution for the diffraction by a smooth convex surface is developed via the ATT, by analytical inversion of the corresponding frequency domain UTD solution obtained previously by Pathak et al. [3, 4]. The analytic time functions obtained from this transformation can not be obtained completely in closed form, but efficient algorithms are developed for their calculation where new special functions are defined for the computation of the TD-UTD convex surface diffraction. The scattering case where the observer and the source are removed from the surface is analyzed here; on the other hand, the case of a source

(pulsed antenna) and/or the observer located on the surface can be dealt with in a similar manner in the future.

The interest in transient electromagnetic analysis where the excitation is a relatively short pulse has been increasing over the years and it constitutes an area of research which will continue to receive attention. This is mainly due to the increased use of ultra-wide band radars and the development of impulse radiating systems. Also, there has been a long time interest in the effects of natural and manmade short electromagnetic pulses (EMPs) on communication and radar systems. It is most natural to analyze such transient problems directly in the time domain. This is especially true when the scattering objects are large in terms of pulse width.

To analyze the scattering or radiation from complex structures, one could alternatively perform a frequency domain UTD analysis at a series of frequencies, then simply apply an appropriate window and use the inverse fast Fourier transform (IFFT) to obtain the scattered field due to a transient pulse excitation. However, a direct TD-UTD analysis of the same problem is more efficient when the pulse is very narrow (for example a pulse with a frequency response with more than 100 percent bandwidth). Also, the TD-UTD can be used to compute an approximate impulse response which can usually provide more insight since the impulse response is essentially independent of the excitation, whereas the response to a particular excitation is obtained from the convolution operation. The TD-UTD provides a new way of examining electromagnetic radiating and scattering phenomena as compared to what has been done in the past, and it therefore could lead to new insights for other applications. Some other applications which may result from this TD-UTD development are parametric models used for radar data analysis [5, 6] and also the development of a new hybrid time domain integral equation based numerical method.

There exist various methods for the numerical analysis of transient electromagnetic problems such as the finite difference time domain (FDTD) method or the time domain integral equation (TD-IE) approaches. These methods have been found to be very useful for a great many problems, but become very cumbersome or even intractable for problems where the geometry is large in terms of pulse width (or in terms

of the smallest wavelength of interest). Because of this, the TD-UTD should provide a very useful complement to these more robust numerical methods when analyzing general problems. Also, the robust numerical methods such as the FDTD and the TD-IE are not well suited for computing approximate impulse responses.

There is an abundance of research which has been done in the past on transient electromagnetic (or acoustic) analysis. In fact, there are some books dedicated to this subject [7, 8, 9]. There is also a large amount of literature on the subject of numerical time domain methods which are not discussed here. There is some work on the formulation of a time domain version of the UTD for wedge diffraction [10, 11, 12], but this previous work concentrates on the time domain analysis of the diffraction from a straight perfectly conducting wedge. Unfortunately, this analysis uses an inverse Laplace transform to obtain the time domain formulas and is thus limited to simple excitations and straight wedges. In contrast, the work in this report can easily handle general astigmatic incident ray fields which may have passed through a caustic before arriving at the edge of the wedge. Also, in this report, the wedge is a general curved wedge which can have curved faces or a curved edge. Other research which is most similar to the TD-UTD development in this report is the spectral theory of transients (STT) [13, 14, 15, 16, 17, 18, 19]. In the STT, an analytic time transform is used which is essentially the same as the ATT of this report except that their time convention for the frequency domain fields is $e^{-i\omega t}$ whereas the time convention used in this report is $e^{j\omega t}$. The important difference between the STT and the TD-UTD is that the STT is used to find the exact time domain solution to canonical geometries which can then be approximated for "early time", whereas the TD-UTD obtains an "early time" solution directly by using the ATT on the frequency domain UTD formulas. In principle, the STT is a very powerful and accurate method but unfortunately the "early time" solutions obtained by the STT method are not generalized to handle relatively arbitrary geometries such as the arbitrary curved wedge analyzed in Chapter 3 of this report. Furthermore, it appears to be rather complicated to extend the STT to deal with smooth convex surfaces as are analyzed in Chapter 4 of this report. The STT has been used to obtain some interesting solutions for straight wedge diffraction

due to a collimated pulsed beam type illumination. It should be mentioned that the STT also provides inspiration especially for the use of the analytic time transform in the present research which may not have been accomplished otherwise.

This report is organized as follows. Chapter 2 discusses the analytic time transform (ATT). The general properties of the ATT and its relations to the traditional Fourier and Laplace transforms are given. The ATT of a frequency domain function produces a complex time function which is analytic in the upper half t -plane, where t is the complex time variable. But there are special properties of the analytic time function when it is evaluated on its boundary of analyticity, the real time axis. These special properties are explained in Chapter 2. There are times when the ATT of a particular frequency domain function can not be obtained in closed form and therefore it is important to be able to calculate the analytic time function for complex time values. For some functions, an early time representation can be obtained from an asymptotic high frequency domain expansion; while, a late time representation can be obtained from a frequency domain power series (i.e. low frequency) expansion. When these two representations overlap for intermediate time values, then these representations can be used to calculate the ATT of the original function. This procedure is explained in Chapter 2 and a particular example is provided for demonstration. Finally, a method for performing an efficient convolution on a broad class of excitation functions with the analytic time impulse response is presented. Further, Appendix A presents a simple method for synthesizing a given smooth transient pulse function in terms of a set of special basis functions which provide the efficient closed form convolution.

Chapter 3 presents the derivation of the TD-UTD analysis of the scattering from a perfectly conducting curved wedge where the curved wedge may have curved faces and also a curved edge. There are four important scattering mechanisms for this geometry; namely, the geometrical optics (GO) ray fields (an incident ray field and a reflected ray field), the first order edge diffracted field, and the higher order slope diffracted field. The incident GO ray may have any polarization including circular polarization or in general elliptical polarization and the ray tube may be an astigmatic

ray tube which has possibly passed through some caustics. The impulse response in Chapter 3 is defined in terms of the temporal behavior of the incident field (which is an analytic delta function for the impulse response computation); while, the geometrical and polarization properties of the incident field are completely general. Two versions of the TD-UTD slope diffraction coefficient are derived; one is based on the frequency domain slope diffraction coefficient by Veruttipong and Kouyoumjian [20]; while, the other is based on the frequency domain slope diffraction coefficient by Hwang and Kouyoumjian [21]. The details of the derivation of these slope diffraction coefficients are presented in Appendix C. These two slope diffraction formulations are compared in the numerical examples in Chapter 3. An exact solution for the scattering from a straight wedge when it is illuminated by an electric or magnetic dipole is used as a reference here. This exact solution is based on Felsen's work [22] and is summarized in Appendix B. The numerical examples also reveal how the impulse response approximated by the asymptotic "early time" TD-UTD may not be causal.

Chapter 4 presents the derivation of the TD-UTD analysis for the scattering from a smooth convex surface. The scattering case is the only one considered here where the source and observer are removed from the boundary. Smooth convex surface diffraction can be modeled by creeping wave modes when the observer is in the deep shadow region, or for multiple encirclements around closed bodies. These creeping wave modes are dispersive in the frequency domain and therefore their impulse response is effectively delayed in time. In other words, the impulse response of a creeping wave mode starts with zero amplitude and gradually builds up to a peak value occurring after the arrival time corresponding to a simple surface diffracted ray path. The ATT of the frequency domain fields for smooth surface diffraction is not obtained in closed form, so a numerical procedure is developed to compute the ATT of the creeping wave mode with extreme efficiency. This numerical algorithm is presented in Appendix D. Chapter 4 also includes the development of a uniform TD-UTD formulation which is valid in the lit region, the shadow region, and across the shadow boundary. To obtain this uniform result, the ATT of the Fock type functions $\frac{1}{(j\omega)^{1/6}} \tilde{P}_{s,h}(\omega^{1/3}\Xi)$ occurring in the corresponding frequency domain UTD

representation are needed. These transforms are not obtained in closed form, but instead approximate expansions for early, late and intermediate time values are obtained, and the ATT of the Fock type functions are thus calculated using an algorithm which chooses the appropriate representation depending on the time variable. This numerical algorithm is presented in Appendix E

Finally, some conclusions are made in Chapter 5. This chapter also discusses some ideas for continuing the development of the TD-UTD so that even more general geometries can be analyzed. The possible impact of the present TD-UTD development along with the use of the ATT is also discussed. In particular, one of the possible applications which might benefit from the TD-UTD is the use of parametric models in the time domain for the analysis of radar scattering data.

An $e^{j\omega t}$ time convention for the frequency domain fields is assumed and suppressed in the following analysis.

Chapter 2

Analytic Time Functions

The Analytic Time Transform (ATT) is fully explained in this chapter. Since many texts define the conventional Fourier Transform (FT) or the Laplace Transform (LT) in slightly different ways, these conventional transforms are explicitly defined here. Also, the relationship between all three transforms is presented. The properties of the ATT are then explored including the important time convolution formula. When the analytic time function obtained from the ATT is evaluated on the real time axis ($\text{Im } t = 0$), some very useful properties arise and these real time properties are explained. Some important examples of analytic time functions which are useful in the TD-UTD are presented in an easy to use table. Also, the ATT of a generic asymptotic high frequency series and a generic low frequency power series are investigated. The ATT of an asymptotic high frequency series or a low frequency power series produces an early time or late time representation, respectively. These “early” time and “late” time representations are sometimes useful in the calculation of special functions. A method for efficiently computing the time convolution of two analytic time functions is also presented. This efficient convolution is especially important for the implementation of the TD-UTD.

It is appropriate at this juncture to describe some of the notation used in this chapter. Throughout this chapter, time domain functions which are real functions of real time, are written in the usual way, for example

$$F(t) \text{ for real } t.$$

Note that these real time functions (when used with the Fourier transform) may be two sided (i.e. not causal). The topic of causality is further discussed later. On the other hand, the analytic time functions obtained from the ATT are analytic (complex) functions of complex time and are denoted by a '+' sign on top, such as

$$\overset{+}{F}(t) \text{ for complex } t.$$

The frequency (or Fourier) domain and Laplace domain functions are denoted by a '~' on top. A Laplace domain function is an analytic function of a complex variable s , for example

$$\tilde{F}(s) \text{ for complex } s = \sigma + j\omega.$$

where σ and ω are real. In many instances, the frequency domain function $\tilde{F}(\omega)$ can be obtained from an evaluation of the Laplace domain function $\tilde{F}(s)$ at imaginary s values (i.e. $\sigma = 0$), which motivates the use of similar notation for the frequency domain functions, such as

$$\tilde{F}(\omega) \text{ for real } \omega.$$

Although the notation for $\tilde{F}(s)$ and $\tilde{F}(\omega)$ appear the same, there are many instances when the functions are different. For example, if $\tilde{F}(s) = 1/s$ then $\tilde{F}(\omega) = \pi\delta(\omega) + \text{pv } [1/(j\omega)]$ where "pv" denotes Cauchy's principle value. Nonetheless, the same notation is used for convenience, and it is obvious from the context whether the function is a Laplace domain function $\tilde{F}(s)$ or a frequency (Fourier) domain function $\tilde{F}(\omega)$.

The word "function" is used loosely here since $F(t)$, or $\tilde{F}(\omega)$, may in general be a distribution (or what is sometimes called a generalized function). Although most mathematicians will not be happy with the use of the word "function", it is nevertheless used in this loose sense throughout this report. This is consistent with much of the engineering literature which, for example, calls the impulse distribution $\delta(t)$ as an impulse function.

All of the frequency domain functions, such as $\tilde{F}(\omega)$, are assumed to be of exponential order α where $\alpha \leq 0$. This means that α is the largest constant such that $\tilde{F}(\omega)e^{\alpha|\omega|} \rightarrow 0$ when $|\omega| \rightarrow \infty$. Notice that there may be times when α is arbitrarily

less than 0 but not equal to zero. For example, when $\tilde{F}(\omega) = \omega$ then $\alpha = \epsilon < 0$ where ϵ is a constant arbitrarily close to 0.

2.1 Definitions

The Fourier transform as used in this report is defined as follows. The Fourier transform is an integral transform that relates a time domain function $F(t)$, which is a function of a real time variable t , to a frequency domain function $\tilde{F}(\omega)$ which is a function of a real frequency variable ω . This transform is defined as

$$\tilde{F}(\omega) = \int_{-\infty}^{\infty} F(t) e^{-j\omega t} dt \quad (2.1)$$

and the inverse Fourier transform is

$$F(t) = \frac{1}{2\pi} \int_{-\infty}^{\infty} \tilde{F}(\omega) e^{j\omega t} d\omega \quad (2.2)$$

The above convention for the Fourier transform is what is typically used in engineering texts. The Fourier transform may also be written as an operator \mathcal{F} as in

$$\tilde{F}(\omega) = \mathcal{F}[F(t)]$$

and the inverse Fourier transform denoted by

$$F(t) = \mathcal{F}^{-1}[\tilde{F}(\omega)]$$

or one can write the relationship between the pair of functions simply as

$$F(t) \xleftrightarrow{\mathcal{F}} \tilde{F}(\omega).$$

It should be kept in mind, for the Fourier transform, that the time domain function $F(t)$ and the frequency domain function $\tilde{F}(\omega)$ are actually distributions. Also, although in general the Fourier transform is defined for complex time functions, in this report the time domain functions (without the $+$ on top) is always assumed real. This implies the following conjugate symmetry relationship for the frequency domain function

$$\tilde{F}(-\omega) = \tilde{F}^*(\omega) \quad (2.3)$$

where $*$ denotes a complex conjugate. This conjugate symmetry relationship is used when finding the connection between the ATT and the Fourier transform. Finally, notice that $F(t)$ may be a two-sided function; this fact turns out to be an important property when one transforms asymptotic high frequency solutions into the time domain which is examined later in this chapter.

The Laplace transform is defined as follows. In this report, only the one-sided Laplace transform is discussed. Although there are some benefits from using the two-sided Laplace transform (such as the ability to transform two-sided time functions) only the one-sided version is used here for two reasons. The first reason is that there is not a sufficient benefit from using the two-sided Laplace transform on the applications discussed in this report. On the other hand, the ATT is far more versatile especially when dealing with asymptotic high frequency results. The second reason is that the one-sided version of the Laplace transform is more widely used and understood. The Laplace transform is defined by

$$\tilde{F}(s) = \int_0^{\infty} F(t)e^{-st}dt \quad \text{for } \text{Re } s > \delta \quad (2.4)$$

and the inverse Laplace transform is

$$F(t) = \frac{1}{2\pi j} \int_{\epsilon-j\infty}^{\epsilon+j\infty} \tilde{F}(s)e^{st}ds \quad (2.5)$$

where $\epsilon > \delta$ and $F(t)$ is of exponential order δ (i.e. δ is the largest value such that $F(t)e^{\delta|t|} \rightarrow 0$ when $t \rightarrow \infty$). The Laplace transform is defined whenever the integral in Equation (2.4) exists, and can be extended to include distributions for which the integral will not, in general, exist in the usual sense [23]. The Laplace transform may also be written as an operator \mathcal{L} as in

$$\tilde{F}(s) = \mathcal{L}[F(t)]$$

and the inverse Laplace transform denoted by

$$F(t) = \mathcal{L}^{-1}[\tilde{F}(s)]$$

or one can write the relationship between the pair of functions simply as

$$F(t) \xleftrightarrow{\mathcal{L}} \tilde{F}(s).$$

Now the analytic time transform (ATT) is defined as follows. There are two versions of this transform. One version transforms a frequency domain function $\tilde{F}(\omega)$ into a complex analytic time function $\tilde{F}^+(t)$, while the other version transforms a real time domain function $F(t)$ into a complex analytic time function $\tilde{F}^+(t)$. When $\tilde{F}(\omega)$ is the Fourier transform of $F(t)$ then both versions produce the same $\tilde{F}^+(t)$. The first version is defined as follows

$$\tilde{F}^+(t) = \frac{1}{\pi} \int_{-\infty}^{\infty} \tilde{F}(\omega) u(\omega) e^{j\omega t} d\omega \quad \text{for } \text{Im } t > \alpha \quad (2.6)$$

When $\tilde{F}(\omega)$ contains no impulses at $\omega = 0$, the above integral can be written as

$$\tilde{F}^+(t) = \frac{1}{\pi} \int_0^{\infty} \tilde{F}(\omega) e^{j\omega t} d\omega \quad \text{for } \text{Im } t > \alpha \quad (2.7)$$

The corresponding inverse ATT is

$$\tilde{F}(\omega) u(\omega) = \frac{1}{2} \int_{-\infty+j\epsilon}^{\infty+j\epsilon} \tilde{F}^+(t) e^{-j\omega t} dt \quad \text{for } \epsilon > \alpha \quad (2.8)$$

where $u(\omega)$ is the Heaviside unit step function defined as

$$u(\omega) = \begin{cases} 0 & \omega < 0 \\ 1/2 & \omega = 0 \\ 1 & \omega > 0 \end{cases} \quad (2.9)$$

This first version of the ATT may be also written as an operator \mathcal{A}_ω as in

$$\tilde{F}^+(t) = \mathcal{A}_\omega [\tilde{F}(\omega)]$$

and the inverse ATT is

$$\tilde{F}(\omega) u(\omega) = \mathcal{A}_\omega^{-1} [\tilde{F}^+(t)]$$

or one can write the relationship between the pair of functions simply as

$$\tilde{F}^+(t) \xleftrightarrow{\mathcal{A}_\omega} \tilde{F}(\omega).$$

The second version of the ATT is defined by

$$\tilde{F}^+(t) = \frac{j}{\pi} \int_{-\infty}^{\infty} \frac{F(\tau)}{t - \tau} d\tau \quad \text{for } \text{Im } t > 0 \quad (2.10)$$

(where $\alpha \leq 0$ has been assumed). Equation (2.10) is sometimes called the Cauchy Representation [24]. The inverse ATT for the second version is

$$F(t) = \text{Re} \left[\overset{+}{F}(t) \right] \quad \text{for } \text{Im } t = 0 \quad (2.11)$$

where $\text{Re}(z)$ denotes the real part of a complex z . Notice that (2.11) uses $\overset{+}{F}(t)$ at $\text{Im } t = 0$ even though in (2.10) it is only defined for $\text{Im } t > 0$. If $\overset{+}{F}(t)$ turns out to be analytic at $\text{Im } t = 0$ then this poses no difficulty, on the other hand, if $\overset{+}{F}(t)$ is not analytic on the real time axis ($\text{Im } t = 0$) then $\overset{+}{F}(t)$ at $\text{Im } t = 0$ is the distribution defined by $\overset{+}{F}(t)$ ($\text{Im } t > 0$) on its boundary of analyticity [24, 25]. One may refer to the book by Beltrami and Wohlers for a thorough explanation of the connection between distributions and analytic functions evaluated on their boundaries of analyticity [25]. The second version of the ATT in (2.10) may also be written as an operator \mathcal{A}_t as in

$$\overset{+}{F}(t) = \mathcal{A}_t[F(t)]$$

and the inverse ATT is

$$F(t) = \mathcal{A}_t^{-1} \left[\overset{+}{F}(t) \right]$$

or one can write the relationship between the pair of functions simply as

$$\overset{+}{F}(t) \xleftrightarrow{\mathcal{A}_t} F(t).$$

Whenever it is obvious from the context which version of the ATT is being used, the subscript on the operator \mathcal{A} is dropped.

Figure 2.1 shows the relationship between the Laplace transform, Fourier transform and the ATT. The \mathcal{H} operator in the figure represents a Hilbert transform which is defined shortly. Notice that the transformation from $\overset{+}{F}(t)$ ($\text{Im } t > 0$) to $F(t) + j\mathcal{H}F(t)$ ($\text{Im } t = 0$) is simply evaluating $\overset{+}{F}(t)$ on the real time axis ($\text{Im } t = 0$). But, the function $\overset{+}{F}(t)$ may not be analytic for $\text{Im } t = 0$. In fact, $\overset{+}{F}(t)$ at ($\text{Im } t = 0$) may be a distribution which appears quite different from the analytic function $\overset{+}{F}(t)$ at $\text{Im } t > 0$. An important example of this is the analytic delta function defined by

$$\overset{+}{\delta}(t) = \begin{cases} \frac{j}{\pi t} & \text{Im } t > 0 \\ \delta(t) + \text{pv } \frac{j}{\pi t} & \text{Im } t = 0 \end{cases} \quad (2.12)$$

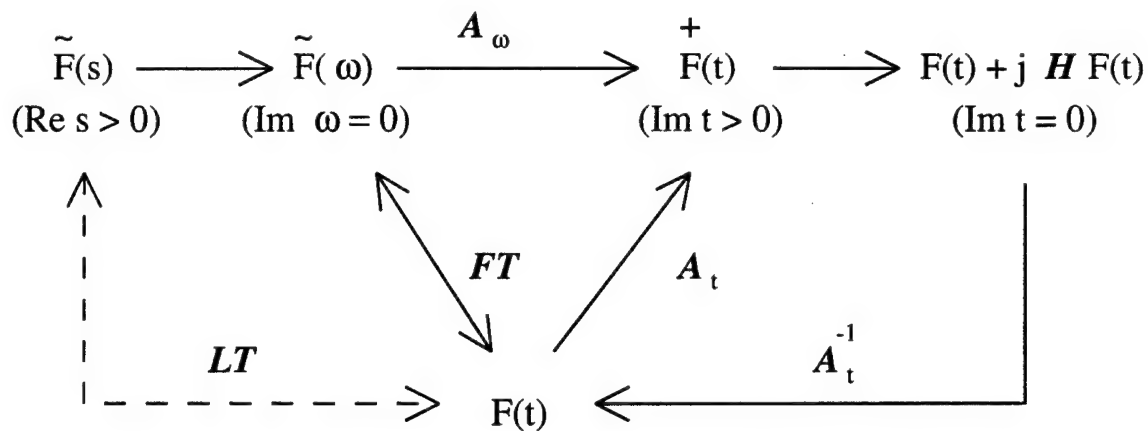


Figure 2.1: Diagram showing the relationship between the Laplace transform (LT), Fourier transform (FT) and analytic time transform (ATT). Notice that $F(t)$ can be obtained directly from an inverse Laplace transform only if $F(t)$ is one-sided since the one-sided Laplace transform is used here.

where “pv” denotes that a Cauchy principal value is understood when integrating over this function. Notice that the frequency response corresponding to the analytic delta function is $\tilde{F}(\omega) = 1$. Also notice that the inverse Fourier transform of $\tilde{F}(\omega) = 1$, which is the Dirac delta function $\delta(t)$, is properly obtained from $\text{Re} [\delta^+(t)]$ when $\text{Im } t = 0$.

An obvious yet very useful observation is now made. The ATT defined by the integral (2.6) is proportional to a one-sided Laplace transform of the frequency domain function $\tilde{F}(\omega)$ where the frequency variable ω acts as the time variable in (2.4) and the Laplace variable s in (2.4) is related to the complex time variable t in (2.6) by $s = -jt$. This is a very useful observation because it allows one to use the extensive tables of one-sided Laplace transforms that exist to evaluate the ATT. This relationship can be written symbolically as

$$\tilde{F}^+(t) = \frac{1}{\pi} \mathcal{L}_x [\tilde{F}(x)] \Big|_{s=-jt} \quad (2.13)$$

where the subscript x on the Laplace operator signifies that x is the variable of integration. This relationship is also used to find the ATT of distributions which are not typically included in Laplace transform theory, but can be found within the context of distribution theory [23].

Table 2.1: Properties of the analytic time transform (ATT)

$\frac{1}{\pi} \int_{-\infty}^{\infty} \tilde{F}(\omega) u(\omega) e^{j\omega t} d\omega$	$\tilde{F}(\omega)$
$\overset{+}{F}(t)$	$\frac{1}{2} \int_{-\infty+j\epsilon}^{\infty+j\epsilon} \overset{+}{F}(t) e^{-j\omega t} dt$
$\frac{1}{a} \overset{+}{F}\left(\frac{t}{a}\right)$	$\tilde{F}(a\omega), a > 0$
$\overset{+}{F}(t-a)$ $\text{Im}(t) > \alpha + \text{Im}(a)$	$e^{-j\omega a} \tilde{F}(\omega)$
$e^{j\beta t} \overset{+}{F}(t)$ $\beta > 0$	$\tilde{F}(\omega - \beta) u(\omega - \beta)$
$e^{j\beta t} \left[\overset{+}{F}(t) + \frac{1}{\pi} \int_{-\beta}^0 \tilde{F}(\omega) e^{j\omega t} d\omega \right]$	$\tilde{F}(\omega - \beta)$
$\frac{\partial}{\partial t} \overset{+}{F}(t)$	$j\omega \tilde{F}(\omega)$
$\frac{\partial^n}{\partial t^n} \overset{+}{F}(t)$	$(j\omega)^n \tilde{F}(\omega)$
$-jt \overset{+}{F}(t) - \frac{1}{\pi} \tilde{F}(0)$	$\frac{\partial}{\partial \omega} \tilde{F}(\omega)$
$(-jt)^n \overset{+}{F}(t) - \frac{1}{\pi} (-jt)^{n-1} \tilde{F}(0) - \dots - \frac{1}{\pi} \tilde{F}^{(n-1)}(0)$	$\frac{\partial^n}{\partial \omega^n} \tilde{F}(\omega)$
$\frac{1}{2} \overset{+}{F}(t) * \overset{+}{G}(t) = \frac{1}{2} \int_{-\infty+j\epsilon}^{\infty+j\epsilon} \overset{+}{F}(\tau) \overset{+}{G}(t-\tau) d\tau$ $\text{Im } t > \alpha_f + \alpha_g$ $\text{Im}(t) - \alpha_g > \epsilon > \alpha_f$	$\tilde{F}(\omega) \tilde{G}(\omega)$

2.2 Properties of the Analytic Time Transform (ATT)

Some important properties of the analytic time transform (ATT) are presented in this section. Also, some useful special properties of the analytic time function when it is evaluated for real time ($\text{Im } t = 0$) are explored.

Table 2.1 summarizes the properties of the ATT. Most of these properties can be easily derived using a change of variables as in (2.13) and a good reference on Laplace transforms [26, 23].

2.2.1 Properties of Analytic Time Functions for Real Time

The properties of the analytic time functions evaluated on the real time axis ($\text{Im } t = 0$) are now examined. During this discussion, it is assumed that $F(t)$ and $\tilde{F}(\omega)$

Table 2.2: Properties of the Hilbert transform. The Hilbert transform of $F(t)$ is denoted by $\mathcal{H}F(t)$ or $\hat{F}(t)$ and similarly for $G(t)$.

$\mathcal{H}[\mathcal{H}F(t)] = -F(t)$
$\mathcal{H}[F(t+a)] = (\mathcal{H}F)(t+a)$
$\mathcal{H}[F(t) * G(t)] = [\mathcal{H}F(t)] * G(t) = F(t) * [\mathcal{H}G(t)]$
$[\mathcal{H}F(t)] * [\mathcal{H}G(t)] = -F(t) * H(t)$
$\mathcal{H}\left[\frac{\partial}{\partial t}F(t)\right] = \frac{\partial}{\partial t}[\mathcal{H}F(t)]$
$\int_{-\infty}^{\infty} F(t)G(t)dt = \int_{-\infty}^{\infty} \hat{F}(t)\hat{G}(t)dt$
$\int_{-\infty}^{\infty} F^2(t)dt = \int_{-\infty}^{\infty} \hat{F}^2(t)dt$

are square integrable functions unless specified otherwise. Nonetheless, many of the properties discussed here can be easily generalized for the case when $F(t)$ and $\tilde{F}(\omega)$ are distributions [25, 23].

When the analytic time function $\tilde{F}^+(t)$ is evaluated on the real time axis, $\text{Im } t = 0$, it can be written as

$$\tilde{F}^+(t) = F(t) + j\mathcal{H}F(t) \quad \text{for } \text{Im } t = 0 \quad (2.14)$$

where $F(t)$ is the inverse Fourier transform of $\tilde{F}(\omega)$

$$F(t) = \mathcal{F}^{-1}[\tilde{F}(\omega)] \quad (2.15)$$

assuming that $\tilde{F}(-\omega) = \tilde{F}^*(\omega)$ where $*$ denotes a complex conjugate. The \mathcal{H} operator denotes a Hilbert transform

$$\mathcal{H}F(t) = \mathcal{F}^{-1}[-j\text{sgn}(\omega)\tilde{F}(\omega)] \quad (2.16)$$

$$= \frac{1}{\pi} \text{pv} \int_{-\infty}^{\infty} \frac{F(x)}{t-x} dx \quad (2.17)$$

Table 2.2 shows a list of useful properties of the Hilbert transform [27]. Another notation which is used for the Hilbert transform is

$$\hat{F}(t) = \mathcal{H}F(t)$$

The following Fourier transform pairs

$$\overset{+}{F}(t) \xleftrightarrow{\mathcal{F}} 2\tilde{F}(\omega)u(\omega) \quad (2.18)$$

$$F(t) \xleftrightarrow{\mathcal{F}} \tilde{F}(\omega) \quad (2.19)$$

$$\hat{F}(t) \xleftrightarrow{\mathcal{F}} -j\text{sgn}(\omega)F(\omega) \quad (2.20)$$

(and similarly for $\overset{+}{G}(t)$, $G(t)$ and $\hat{G}(t)$) can be used to derive some additional interesting relationships, such as

$$\int_{-\infty}^{\infty} F(t)G(t)dt = \frac{1}{2} \text{Re} \int_{-\infty}^{\infty} \overset{+}{F}(t) \overset{+}{G}^*(t)dt \quad (2.21)$$

$$\int_{-\infty}^{\infty} F^2(t)dt = \frac{1}{2} \int_{-\infty}^{\infty} |\overset{+}{F}(t)|^2 dt \quad (2.22)$$

$$\begin{aligned} \frac{1}{2} \overset{+}{F}(t) * \overset{+}{G}(t) &= \overset{+}{F}(t) * G(t) \\ &= F(t) * \overset{+}{G}(t) \end{aligned} \quad (2.23)$$

$$\frac{1}{2} \text{Re} [\overset{+}{F}(t) * \overset{+}{G}(t)] = F(t) * G(t) \quad (2.24)$$

for real time, $\text{Im } t = 0$, and $*$ here denotes a convolution along the real time axis.

2.3 Some Important Analytic Time Functions

Table 2.4 summarizes some useful ATT transform pairs. Most of the transforms in Table 2.4 can be derived by using (2.13) along with a good table of Laplace transforms [28, 23]. Nonetheless, some care must be taken when using this table, especially if one is applying the ATT to an asymptotic high frequency representation. This is discussed in more detail later in this chapter. If one is working with a Laplace domain function then Table 2.3 can be used to find the corresponding Fourier domain function before using Table 2.4. Note that the “Pf” in Table 2.3 stands for pseudofunction as defined by Zemanian [23]. When one integrates over a pseudofunction, one takes Hadamard’s finite part of the integral which may be thought of qualitatively as a generalization of Cauchy’s principle value for higher order singular integrands. For the Laplace domain function $\tilde{F}(s) = s^\eta$ where η is not an integer, the branch cut is chosen to lie on the negative real s axis ($\text{Re } s < 0$, $\text{Im } s = 0$) as usual. For the analytic time

Table 2.3: Relationship between some Laplace domain functions, $\tilde{F}(s)$ and corresponding frequency (or Fourier) domain functions, $\tilde{F}(\omega)$

$\tilde{F}(s)$ $s = \sigma + j\omega$	$\tilde{F}(\omega)$ (ω is real)
$\frac{1}{s}$	$\pi\delta(\omega) + \text{pv} \frac{1}{j\omega}$
$\frac{1}{s^{n+1}}$ $n=0,1,2,\dots$	$\frac{j\pi}{n!}\delta^n(\omega) + \text{Pf} \frac{1}{(j\omega)^{n+1}}$
$\frac{1}{s^{\mu+1}}$ $\mu > -1$ $\mu \neq \text{integer}$	$\text{Pf} \frac{1}{(j\omega)^{\mu+1}}$
s^n $n=0,1,2,\dots$	$(j\omega)^n$
s^η $\eta \neq \text{integer}$	$(j\omega)^\eta$
$\frac{1}{s+a}, a > 0$	$\frac{1}{j\omega+a}$
$\frac{e^{-s(t_0 - \frac{T}{2})}}{s} - \frac{e^{-s(t_0 + \frac{T}{2})}}{s}$ $t_0 \geq \frac{T}{2}$	$T e^{j\omega t_0} \text{sinc}(\frac{\omega T}{2})$

function $(-jt)^{-\eta-1}$, the branch cut is on the negative real axis in the $-jt$ plane, which corresponds to the negative imaginary axis in the t plane ($\text{Re } t = 0, \text{Im } t < 0$).

The notation for special functions in Table 2.4, such as $E_1(z)$ to denote the exponential integral or $\text{erfc}(z)$ to denote the complementary error function follows the notation in the standard reference of Abramowitz and Stegun [29].

2.4 Representations of Analytic Time Functions

This section is concerned with various representations of analytic time functions which may be useful for both analytical and computational reasons. A late time series in terms of inverse powers of time, $(1/t)$, is derived by the ATT from a low frequency

Table 2.4: The analytic time transform (ATT) of some useful functions. In this table, n is a non-negative integer, $\mu > -1$ is not an integer, and η is not an integer.

$\tilde{F}(\omega)$	$\tilde{F}^+(t)$ $\text{Im } t > 0$	$F(t) + j\mathcal{H}F(t)$ $\text{Im } t = 0$
1	$\frac{j}{\pi t}$	$\delta(t) + \text{pv} \frac{j}{\pi t}$
$\pi\delta(\omega) + \text{pv} \frac{1}{j\omega}$	$\frac{1}{2} - \frac{1}{\pi} \arg(-jt)$ $+ \frac{j}{\pi} [\ln t + \gamma]$	$u(t) + \frac{j}{\pi} [\ln t + \gamma]$
$\frac{j\pi}{n!} \delta^n(\omega)$ $+ \text{Pf} \frac{1}{(j\omega)^{n+1}}$	$\frac{t^n}{n!} \left[\frac{1}{2} - \frac{1}{\pi} \arg(-jt) \right]$ $+ j \frac{t^n}{\pi n!} [\ln t - \psi(n+1)]$	$\frac{t^n}{n!} u(t)$ $+ j \frac{t^n}{\pi n!} [\ln t - \psi(n+1)]$
$\text{Pf} \frac{1}{(j\omega)^{\mu+1}}$	$\frac{\Gamma(-\mu)}{\pi j^{\mu+1}} (-jt)^\mu$	$\frac{t^\mu}{\Gamma(\mu+1)} (1 + j \cot \pi \mu) \quad t > 0$ $j \csc \pi \mu \frac{(-t)^\mu}{\Gamma(\mu+1)} \quad t < 0$
$(j\omega)^n$	$\frac{j^n n!}{\pi (-jt)^{n+1}}$	$\delta^n(t) + \frac{(-1)^{n+1} n!}{j \pi t^{n+1}}$
$(j\omega)^\eta$	$\frac{j^\eta \Gamma(\eta+1)}{\pi (-jt)^{\eta+1}}$	$\frac{\Gamma(\eta+1)}{\pi t^{\eta+1}} j e^{j\pi\eta}, \quad t > 0$ $\frac{-j \Gamma(\eta+1)}{\pi (-t)^{\eta+1}}, \quad t < 0$
$\frac{1}{j\omega+a}$	$\frac{1}{j\pi} e^{-at} E_1(-at)$	$e^{-at} [1 + \frac{j}{\pi} E_i(at)], \quad t > 0$ $-e^{-at} \frac{j}{\pi} E_1(-at), \quad t < 0$
$\sigma\sqrt{2\pi} e^{-\sigma^2\omega^2/2}$	$e^{-t^2/(2\sigma^2)} \text{erfc}(\frac{-jt}{\sigma\sqrt{2}})$	$e^{-t^2/(2\sigma^2)}$ $+ \frac{j}{\pi} \text{pv} \int_{-\infty}^{\infty} \frac{e^{-x^2}}{t-x} dx$
$T e^{j\omega t_0} \text{sinc}(\frac{\omega T}{2})$	$\frac{j}{\pi} \ln \left(\frac{t-t_0+\frac{T}{2}}{t-t_0-\frac{T}{2}} \right)$	$u(t-t_0+\frac{T}{2}) - u(t-t_0-\frac{T}{2})$ $+ \frac{j}{\pi} \ln \left \frac{t-t_0+\frac{T}{2}}{t-t_0-\frac{T}{2}} \right $
$e^{-a \omega }$ $a > 0$	$\frac{j}{\pi(t+ja)}$	$\frac{a}{\pi(t^2+a^2)} + j \frac{t}{\pi(t^2+a^2)}$

power series. Then an early time series in terms of powers of time, t , is derived by the ATT from a high frequency asymptotic series. It is shown, by an example, that an early time series obtained by a term-by-term application of the ATT may be incomplete. The mathematical justification for these representations may be found in [26, 30, 31] where the roles of time and frequency are switched as compared to here.

2.4.1 Analytic Time Transform of Low Frequency Power Series

The ATT of a series which is accurate at low frequencies produces a time representation which is asymptotically valid at late times. The mathematical basis for this fact is well known and can be found in texts on Laplace transform theory [30, 26] where the connection between the ATT and the Laplace transform in (2.13) is understood. In particular, the general theorem on the Laplace transform of asymptotic representations is on page 6 in Seigel [32].

Consider the following asymptotic representation

$$\tilde{F}(\omega) \sim \sum_{n=1}^N A_n (j\omega)^{\mu_n} \quad \text{for } \omega \rightarrow 0^+ \quad (2.25)$$

where $\mu_n > -1$ and $\mu_n \uparrow \infty$ as $n \rightarrow \infty$. Then the "early time" analytic time representation corresponding to this asymptotic low frequency representation is

$$\tilde{F}^+(t) \sim \frac{1}{\pi} \sum_{n=1}^N A_n \frac{j^{\mu_n} \Gamma(\mu_n + 1)}{(-jt)^{\mu_n + 1}} \quad \text{for } |t| \rightarrow \infty \quad (2.26)$$

where $\text{Im } t > 0$.

2.4.2 Analytic Time Transform of High Frequency Asymptotic Series

When solving for "early time" solutions to electromagnetic radiation or scattering problems, one may solve the frequency domain (FD) (i.e. time harmonic) problem first, then obtain a high frequency asymptotic expansion of this FD solution and finally perform an inverse Laplace transform to obtain a time domain power series [33, 34, 9]. Let the asymptotic expansion of the FD solution have the form

$$\tilde{F}(s) \sim e^{-st_0} \left[C_0 + \sum_{n=1}^N \frac{C_n}{s^{\nu_n + 1}} \right] \quad \text{Re } s > 0 \quad (2.27)$$

for $|s| \rightarrow \infty$, where $s = \sigma + j\omega$, C_0 and C_n are constant with respect to frequency, t_0 is some time delay dependent on the problem geometry and $\nu_n > -1$. Note that ν_n is not necessarily an integer. Also, notice that N in (2.27) is not the same as the N in (2.26). Typically, an inverse Laplace transform is applied to (2.27) to find the corresponding “early time” power series [33, 34]

$$F(t) \sim C_0 \delta(t - t_0) + \sum_{n=1}^N \frac{C_n}{\Gamma(\nu_n + 1)} (t - t_0)^{\nu_n} u(t - t_0) \quad (2.28)$$

for $t \rightarrow 0$, where $\delta(t)$ is the Dirac delta function, $\Gamma(z)$ is the Gamma function, and $u(t)$ is the Heaviside unit step function. This time domain series provides a satisfactory solution if the constants C_0 and $\{C_n\}$ are real, but unfortunately this is not always the case. Consider the extremely simple case of the plane wave reflection from a concave surface. The first term in the high frequency asymptotic expansion is the geometrical optics (GO) reflected field which may pass through a caustic and will then gain a factor of $e^{j\pi/2}$. This factor $e^{j\pi/2}$ makes the constant C_0 in the FD asymptotic expansion in (2.27) complex and then the time domain series in (2.28) no longer makes sense since the time domain solution should be a real function.

When the constants $\{C_0, C_n\}$ in (2.27) are complex, one can obtain a real time domain solution $F(t)$ by first evaluating $\tilde{F}(s)$ for $\text{Re}(s) = 0$ ($\sigma = 0$) to obtain $\tilde{F}(\omega)$ and then enforcing the relationship $\tilde{F}(-\omega) = \tilde{F}^*(\omega)$ for negative frequencies ($\omega < 0$) and applying an inverse Fourier transform, where the frequency variable ω and the time variable t are real. For example, the $\exp(j\pi/2)$ factor discussed above applies only for positive frequencies and more generally one would use a factor of $\exp(j\text{sgn}(\omega)\pi/2)$ to ensure that $F(t)$ is a real function. Notice that each term in (2.27) is not absolutely integrable (when $\text{Re}(s) = 0$), and therefore, each term must be considered a distribution, see Table 2.3, and one must resort to using the theory of distributions [23, 24] or generalized functions [35, 36] to find the inverse Fourier transform.

Alternatively, one could obtain a real time domain function $F(t)$ from the Laplace domain function $\tilde{F}(s)$ by enforcing the conjugate symmetry relationship $\tilde{F}(s^*) =$

$\tilde{F}^*(s)$ and applying an inverse two-sided Laplace transform. But this can be quite complicated even for a simple algebraic $\tilde{F}(s)$ function.

Instead of using an inverse Fourier transform or an inverse two-sided Laplace transform as just described, it may be easier to obtain the inverse Fourier transform via the analytic signal representation described earlier. First find the ATT of (2.27) to provide an analytic function of time. Then evaluate this analytic function for real time ($\text{Im } t = 0$) and take the real part to obtain the final real time function which equals the inverse Fourier transform [25, 37]. Note that the analytic time function is analytic for $\text{Im } t > 0$ and its boundary value at $\text{Im } t = 0$ is a distribution [25, 37].

The form of the early time asymptotic expansion obtained from the high frequency asymptotic expansion using the analytic time transform depends on the form of the high frequency expansion. Three particular cases are presented here. The following early time expansions are derived by using the results in Chapter 4 of Bleistein and Handelsman's book [31] and the relationship between Laplace transforms and the analytic time transform in (2.13).

Consider the following high frequency asymptotic expansion

$$\tilde{F}(\omega) \sim \sum_{m=0}^{\infty} A_m(j\omega)^{-r_m} \quad \text{for } \omega \rightarrow \infty \quad (2.29)$$

where r_m is not a positive integer here and $\text{Re}(r_m) \uparrow \infty$ as $m \rightarrow \infty$. Then the early time expansion corresponding to the function in (2.29) obtained from the asymptotic results in Bleistein and Handelsman [31] and (2.13) is

$$\begin{aligned} \tilde{F}^+(t) \sim & \frac{1}{\pi} \sum_{m=0}^{\infty} A_m j^{-r_m} \Gamma(1 - r_m) (-jt)^{r_m-1} \\ & + \frac{1}{\pi} \sum_{m=0}^{\infty} \frac{(-1)^m}{m!} \mathcal{M}[\tilde{F}; m+1] (-jt)^m \end{aligned} \quad (2.30)$$

where $\mathcal{M}[\tilde{F}; m+1]$ is the generalized Mellin transform of $\tilde{F}(\omega)$ which is defined shortly. Notice that the first summation in (2.30) is exactly what would be obtained if the analytic time transform in (2.6) is applied to the frequency domain asymptotic expansion in (2.29) term-by-term. Also, notice that Tables 2.3 and 2.4 are very useful for this term-by-term transformation. But the second summation in (2.30)

is not predicted by applying the analytic time transform term-by-term and yet it is obviously important. In fact, the example in the next section demonstrates this fact.

The ordinary (i.e. not generalized) Mellin transform, denoted by the operator symbol \mathcal{M} is defined as

$$\mathcal{M}[\tilde{F}; z] = \int_0^\infty \tilde{F}(\omega) \omega^{z-1} d\omega \quad (2.31)$$

The generalized Mellin transform is defined by

$$\mathcal{M}[\tilde{F}; z] = \mathcal{M}[\tilde{F}_1; z] + \mathcal{M}[\tilde{F}_2; z] \quad (2.32)$$

where

$$\mathcal{M}[\tilde{F}_1; z] = \int_0^1 \tilde{F}(\omega) \omega^{z-1} d\omega \quad (2.33)$$

which can usually be analytically extended as a meromorphic function into the entire z -plane and

$$\mathcal{M}[\tilde{F}_2; z] = \int_1^\infty \tilde{F}(\omega) \omega^{z-1} d\omega \quad (2.34)$$

which can usually also be analytically extended as a meromorphic function into the entire z -plane. So the expression in (2.32) should be interpreted as a meromorphic function in the z -plane even though the integral expressions in (2.33) and (2.34) may not converge for the same z values. See Chapter 4 of [31] for more information on the generalized Mellin transform.

Now consider the following possible high frequency asymptotic expansion

$$\tilde{F}(\omega) \sim e^{-\omega^\nu d} \sum_{m=0}^{\infty} A_m (j\omega)^{-r_m} \quad \text{for } \omega \rightarrow \infty \quad (2.35)$$

where $\text{Re}(d) \geq 0$, $\nu > 0$ and $\text{Re}(r_m) \uparrow \infty$ as $m \rightarrow \infty$. The early time asymptotic expansion corresponding to (2.35) is

$$\tilde{F}^+(t) \sim \frac{1}{\pi} \sum_{m=0}^{\infty} \frac{(-1)^m}{m!} \mathcal{M}[\tilde{F}; m+1] (-jt)^m \quad (2.36)$$

where $\mathcal{M}[\tilde{F}; m+1]$ is the generalized Mellin transform of $\tilde{F}(\omega)$. If the Mellin transform $\mathcal{M}[\tilde{F}; m+1]$ exists in the ordinary sense (i.e. the integral in (2.31) is convergent) for $m = 0, 1, 2, \dots$ then the expansion in (2.36) is an “expansion by moments”. This expansion is used in Appendix D to derive (D.12).

Finally, consider a third possible high frequency expansion which has the form

$$\tilde{F}(\omega) \sim \sum_{m=0}^{\infty} A_m(j\omega)^{-r_m} \quad \text{for } \omega \rightarrow \infty \quad (2.37)$$

where $\text{Re}(r_m) \uparrow \infty$ as $m \rightarrow \infty$. This is the same as the high frequency expansion in (2.29) and for the terms where r_m is not an integer one could use the result in (2.30). However if r_m is an integer, there exists a different corresponding m^{th} term in the early time series. So, consider the case when r_m is an integer (say $r_m = n + 1$ where n is an integer), then the corresponding term in the early time expansion has the form

$$\begin{aligned} -A_m j^{-n-1} \frac{(-1)^n}{n!} (-jt)^n [\ln(-jt) - \psi(n+1)] \\ + j^{-n-1} \frac{(-1)^n}{n!} (-jt)^n C_n \end{aligned} \quad (2.38)$$

where

$$C_n = \lim_{z \rightarrow (n+1)} \left\{ \frac{\partial}{\partial z} (z - 1 - n) \mathcal{M}[\tilde{F}; z] \right\} \quad (2.39)$$

and

$$\psi(1) = -\gamma = -0.577216 \dots \quad (2.40)$$

$$\psi(n+1) = -\gamma + \sum_{l=1}^n \frac{1}{l} \quad \text{for } n \geq 1 \quad (2.41)$$

where γ is Euler's constant. For example, consider the following high frequency expansion

$$\tilde{F}(\omega) \sim \sum_{m=0}^{\infty} A_m(j\omega)^{-m-1} \quad \text{for } \omega \rightarrow \infty \quad (2.42)$$

where m is an integer, then the corresponding early time expansion is

$$\begin{aligned} \tilde{F}^+(t) \sim \frac{1}{\pi} \sum_{m=0}^{\infty} \left\{ -A_m j^{-m-1} \frac{(-1)^m}{m!} (-jt)^m [\ln(-jt) - \psi(m+1)] \right. \\ \left. + j^{-m-1} \frac{(-1)^m}{m!} C_m (-jt)^m \right\} \end{aligned} \quad (2.43)$$

Notice that if one assumes that the expansion in (2.42) can be transformed term-by-term and uses the results in Table 2.4 for each term, then the constant C_m in (2.43) would be $C_m = j^{\frac{\pi}{2}} A_m$. Further, notice that if the one sided inverse Laplace transform is applied to a function with the following asymptotic series, which has a finite radius of convergence [30],

$$\tilde{F}(s) \sim \sum_{m=0}^{\infty} A_m s^{-m-1} \quad \text{for } |s| \rightarrow \infty \quad (2.44)$$

where $|\arg(s)| < \pi/2$, then one obtains a corresponding early time expansion

$$F(t) \sim \sum_{m=0}^{\infty} \frac{A_m}{m!} t^m u(t) \quad (2.45)$$

Now, if one uses $C_m = j\frac{\pi}{2}A_m$ in (2.43) and takes the real part of $\tilde{F}^+(t)$ than one recovers the result in (2.45). It is now reasonable to conjecture that the formula in (2.39) for C_n could be simplified to $C_n = j\frac{\pi}{2}A_n$ (where $r_m = n+1$) although this result has yet to be shown.

2.4.3 Example: The TD-UTD Edge Diffraction Transition Function

An example is now examined to demonstrate some of the formulas presented in the previous section. The particular function which is examined is the TD-UTD edge diffraction transition function which is used in Chapter 3. This function is well understood and the analytic time transform is known in closed form. So, although one would normally not need the early or late time expansions of this function for computations, it is an interesting example since the early and late time expansions can be verified by examining the closed form time domain function.

The frequency domain function of interest is

$$\tilde{F}(\omega) = \sqrt{\pi x} e^{j\omega x/c} \operatorname{erfc} \left(\sqrt{\frac{j\omega x}{c}} \right) \quad (2.46)$$

$$= \sqrt{\frac{c}{j\omega}} \tilde{F}_{tr} \left(\frac{\omega x}{c} \right) \quad (2.47)$$

$$= \frac{x e^{j\pi/4}}{\sqrt{\pi}} \int_{-\infty+j\epsilon}^{\infty+j\epsilon} \frac{e^{-\omega \mu^2/c}}{\mu^2 + jx} d\mu \quad (2.48)$$

where $\epsilon > 0$ and $\tilde{F}_{tr}(z)$ is the usual frequency domain UTD transition function defined in (3.33). For now, simply assume that x and c are positive constants. Their physical meaning is fully explained in Chapter 3. The analytic time transform of (2.46) can be obtained in closed form as

$$\tilde{F}^+(t) = \frac{\sqrt{x/\pi}}{\sqrt{-jt} (\sqrt{-jt} + \sqrt{jx/c})} \quad (2.49)$$

Now, a low frequency power series expansion of (2.46) which happens to be convergent for all finite values of ω is

$$\tilde{F}(\omega) = \sqrt{\pi x} e^{j\omega x/c} \left[1 - \frac{2}{\sqrt{\pi}} \sum_{n=0}^{\infty} \frac{(-1)^n (j\omega x/c)^{n+1/2}}{n!(2n+1)} \right] \quad (2.50)$$

Using (2.26), one can write down the corresponding late time expansion of the analytic time transform of (2.50)

$$\tilde{F}^+(t) \sim \frac{1}{\sqrt{\pi}} \left[\frac{\sqrt{x}}{-j\tau} - \frac{x}{\sqrt{c}} \frac{j^{1/2}}{(-j\tau)^{3/2}} + \frac{x^2}{2c^{3/2}} \frac{j^{3/2}}{(-j\tau)^{5/2}} \dots \right] \quad (2.51)$$

where

$$\tau = t + x/c$$

Notice that (2.51) is convergent for $|x/(c\tau)| < 1$. Now, the late time expansion in (2.51) can also be obtained directly from the closed form result in (2.49). First rewrite (2.49) as

$$\tilde{F}^+(t) = \frac{\sqrt{x}}{\sqrt{\pi}(-j\tau)} - \frac{x\sqrt{j/c}}{\sqrt{\pi}(-j\tau)^{3/2}} \left[1 + \left(\frac{jx}{-j\tau c} \right) \right]^{-1/2} \quad (2.52)$$

and then use

$$(1+z)^{-1/2} = 1 - \frac{1}{2}z + \frac{1 \cdot 3}{2 \cdot 4}z^2 \dots \quad \text{for } |z| < 1$$

to obtain (2.51). Although, using the closed form time domain function to obtain the late time expansion is trivial for this particular function one should keep in mind that for some other frequency domain functions one doesn't have a closed form time domain formula and may need the late time expansion to perform computations.

An alternate late time expansion whose convergence is centered at $t = 0$ (instead of $t = -x/c$ as in (2.51)) can be obtained. To obtain this alternate expansion, first substitute

$$e^{j\omega x/c} = \sum_{m=0}^{\infty} \frac{1}{m!} \left(\frac{j\omega x}{c} \right)^m$$

into (2.50) and after a good deal of algebra obtain

$$\begin{aligned} \tilde{F}(\omega) = & \sqrt{\pi x} \left[1 - \frac{2}{\sqrt{\pi}} \left(\frac{j\omega x}{c} \right)^{1/2} + \left(\frac{j\omega x}{c} \right) \right. \\ & \left. - \frac{4}{3\sqrt{\pi}} \left(\frac{j\omega x}{c} \right)^{3/2} + \frac{1}{2} \left(\frac{j\omega x}{c} \right)^2 \dots \right] \end{aligned} \quad (2.53)$$

Now use (2.25) and (2.26) to obtain the alternate late time expansion

$$\begin{aligned} \tilde{F}^+(t) = & \sqrt{\frac{x}{\pi}} \frac{1}{(-jt)} \left[1 - j^{1/2} \left(\frac{x}{-jtc} \right)^{1/2} + j \left(\frac{x}{-jtc} \right) \right. \\ & \left. - j^{3/2} \left(\frac{x}{-jtc} \right)^{3/2} + j^2 \left(\frac{x}{-jtc} \right)^2 \dots \right] \end{aligned} \quad (2.54)$$

where this series is convergent for $|x/(ct)| < 1$. The late time series in (2.54) can also be obtained directly from the closed form time function in (2.49). Rewrite (2.49) as

$$\tilde{F}^+(t) = \frac{\sqrt{x/\pi}}{-jt} \left[1 + \left(\frac{jx}{-jtc} \right)^{1/2} \right]^{-1} \quad (2.55)$$

and then use

$$(1+z)^{-1} = 1 - z + z^2 - z^3 + z^4 \dots \quad \text{for } |z| < 1$$

to derive the late time series in (2.54).

Now an early time expansion is derived from a high frequency asymptotic expansion of $\tilde{F}(\omega)$ in (2.46), which can be written as

$$\begin{aligned} \tilde{F}(\omega) \sim & \left(\frac{c}{j\omega} \right)^{1/2} - \frac{1}{2x} \left(\frac{c}{j\omega} \right)^{3/2} + \frac{3}{4x^2} \left(\frac{c}{j\omega} \right)^{5/2} \\ & - \frac{15}{8x^3} \left(\frac{c}{j\omega} \right)^{7/2} + \frac{105}{16x^4} \left(\frac{c}{j\omega} \right)^{9/2} \dots \end{aligned} \quad (2.56)$$

for $\omega \rightarrow \infty$, or more generally,

$$\tilde{F}(\omega) \sim \sqrt{\frac{c}{j\omega}} \left[1 + \sum_{m=1}^{\infty} (-1)^m \frac{1 \cdot 3 \dots (2m-1)}{2^m} \left(\frac{c}{j\omega x} \right)^m \right] \quad (2.57)$$

To obtain the early time expansion of $\tilde{F}^+(t)$ from (2.57), use (2.30). Notice that if the ATT is applied to the asymptotic expansion in (2.57) term-by-term then only the first summation in (2.30) is obtained. But, the second summation is obviously important as will be seen shortly. Using (2.30) on (2.57), the first summation is

$$\frac{1}{\sqrt{\pi}\sqrt{-jt}} \sqrt{\frac{c}{j}} \sum_{m=0}^{\infty} \left(\frac{-jct}{jx} \right)^m$$

which is the result which could be obtained by a term-by-term transformation. The second summation in (2.30) contains the Mellin transform of the frequency domain

function $\tilde{F}(\omega)$. This can be evaluated as follows

$$\mathcal{M}[\tilde{F}; m+1] = \int_0^\infty \frac{x e^{j\pi/4}}{\sqrt{\pi}} \int_{-\infty+j\epsilon}^{\infty+j\epsilon} \frac{e^{-\omega\mu^2/c}}{\mu^2 + jx} d\mu \omega^m d\omega \quad (2.58)$$

$$= \frac{x e^{j\pi/4}}{\sqrt{\pi}} \int_{-\infty+j\epsilon}^{\infty+j\epsilon} \frac{1}{\mu^2 + jx} \int_0^\infty \omega^m e^{-\omega\mu^2/c} d\omega d\mu \quad (2.59)$$

$$= \frac{x e^{j\pi/4}}{\sqrt{\pi}} c^{m+1} \Gamma(m+1) \int_{-\infty+j\epsilon}^{\infty+j\epsilon} \frac{1}{(\mu^2 + jx)(\mu^2)^{m+1}} d\mu \quad (2.60)$$

$$= \frac{x e^{j\pi/4}}{\sqrt{\pi}} c^{m+1} \Gamma(m+1) 2\pi j \frac{1}{2e^{-j\pi/4}\sqrt{x}} \frac{1}{(-jx)^{m+1}} \quad (2.61)$$

$$= -m! \sqrt{\pi x} \frac{c^{m+1}}{(-jx)^{m+1}} \quad (2.62)$$

and then the second summation in (2.30) is

$$j \frac{c}{\sqrt{\pi x}} \sum_{m=0}^{\infty} \left(\frac{c}{jx} \right)^m (-jt)^m$$

Finally, the total early time expansion can now be written as

$$\tilde{F}^+(t) \sim \frac{1}{\sqrt{\pi} \sqrt{-jt}} \sqrt{\frac{c}{j}} \sum_{m=0}^{\infty} \left(\frac{-jct}{jx} \right)^m + j \frac{c}{\sqrt{\pi x}} \sum_{m=0}^{\infty} \left(\frac{c}{jx} \right)^m (-jt)^m \quad (2.63)$$

Notice that this series is convergent for $|ct/x| < 1$. If the time variable is allowed to be real $\text{Im}(t) = 0$ then it is more convenient to write (2.63) as

$$\tilde{F}^+(t) \sim \frac{\sqrt{c}}{\sqrt{\pi t}} \sum_{m=0}^{\infty} \left(-\frac{ct}{x} \right)^m + j \frac{c}{\sqrt{\pi x}} \sum_{m=0}^{\infty} \left(-\frac{ct}{x} \right)^m \quad (2.64)$$

Recall that a term-by-term transformation would provide the first summation in (2.64) and therefore for this example a term-by-term transformation correctly predicts the early time behavior of the real part of $\tilde{F}^+(t)$ when evaluated for real time ($\text{Im}(t) = 0$) but the imaginary part of $\tilde{F}^+(t)$ can not be correctly obtained from a term-by-term transformation. Now, the early time expansion in (2.63) can also be derived directly from the closed form result in (2.49). First, write the closed form formula in (2.49) as

$$\frac{1}{\sqrt{\pi}} \frac{1}{\sqrt{-jt}} \sqrt{\frac{c}{j}} \left[1 + \sqrt{\frac{-jtc}{jx}} \right]^{-1} \quad (2.65)$$

and use

$$(1+z)^{-1} = \sum_{m=0}^{\infty} (-1)^m z^m \quad \text{for } |z| < 1$$

to obtain the early time expansion in (2.63).

The important observation to be made from this example is that one can not apply the analytic time transformation to a high frequency asymptotic series term by term. Instead one must use a more careful asymptotic analysis such as in Bleistein and Handelsman's book [31].

2.5 Efficient Time Convolution

Consider the problem of finding the ATT of the product of two frequency domain functions $\tilde{F}(\omega)\tilde{H}(\omega)$. The time convolution property can be used here

$$\tilde{F}(\omega)\tilde{H}(\omega) \xleftrightarrow{A} \frac{1}{2} \overset{+}{F}(t) * \overset{+}{H}(t) \quad (2.66)$$

where the time convolution integration path is placed above the real time axis in the complex time plane. If the frequency domain function $\tilde{F}(\omega)$ can be modeled using exponential functions

$$\tilde{F}(\omega) = \sum_{n=1}^N A_n e^{-\alpha_n \omega} \quad \text{for } \omega > 0 \quad (2.67)$$

or equivalently, if

$$\overset{+}{F}(t) = \frac{j}{\pi} \sum_{n=1}^N \frac{A_n}{t + j\alpha_n} \quad (2.68)$$

$$= \sum_{n=1}^N A_n \overset{+}{\delta}(t + j\alpha_n) \quad (2.69)$$

then the convolution can be evaluated in closed form as

$$\frac{1}{2} \overset{+}{F}(t) * \overset{+}{H}(t) = \sum_{n=1}^N A_n \overset{+}{H}(t + j\alpha_n) \quad (2.70)$$

where the shifting property of the analytic delta function

$$\frac{1}{2} \overset{+}{H}(t) * \overset{+}{\delta}(t + j\beta) = \overset{+}{H}(t + j\beta) \quad (2.71)$$

was used.

A useful approximate formula for the convolution operation may be obtained when the frequency response of the excitation is bandlimited (i.e. $\tilde{F}_0^i(\omega)u(\omega) = 0$

when $\omega > \omega_m$ for some constant ω_m). This useful approximate formula is derived with the knowledge that $F_0^+(t)$ is analytic in the entire t -plane.

$$\frac{1}{2} F_0^+(t) * \dot{H}^+(t) = \frac{1}{2} \int_{-\infty+j\epsilon}^{\infty+j\epsilon} F_0^+(t-\alpha) \dot{H}^+(\alpha) d\alpha \quad (2.72)$$

$$= \frac{1}{2} \int_{-\infty}^{\infty} F_0^+(t-\beta-j\epsilon) \dot{H}^+(\beta+j\epsilon) d\beta \quad (2.73)$$

$$= \frac{1}{2} \int_{-\infty}^{\infty} F_0^+(\gamma-j\epsilon) \dot{H}^+(t-\gamma+j\epsilon) d\gamma \quad (2.74)$$

$$\approx \frac{d}{2} \sum_{m=-M}^M F_0^+(md-j\epsilon) \dot{H}^+(t-md+j\epsilon) \quad (2.75)$$

The above approximation is obviously the same as (2.70) with $A_n = \frac{d}{2} F_0^+(md-j\epsilon)$, $\alpha_n = \epsilon + jmd$ and $m = n - N + 1$.

Chapter 3

TD-UTD for a Curved Wedge

This chapter presents the development of the TD-UTD solution for the scattering from a perfectly electrically conducting (PEC) arbitrary curved wedge when it is illuminated by an analytic time impulsive astigmatic wavefront. This solution is obtained by an analytic time transform (ATT), as defined in the previous chapter, of the corresponding frequency domain UTD solution for a perfectly conducting curved wedge [2, 4, 38]. Thus, the present solution constitutes a time domain UTD (TD-UTD) for a curved wedge in which the transient fields propagate along the ray paths of the UTD. The TD ray solution (or TD-UTD) is only valid for “early to intermediate times” since the UTD is an asymptotic solution in the frequency domain that remains accurate for moderate to high frequencies. Thus, each TD-UTD ray contribution is most accurate in the neighborhood of the time required to traverse its geometric ray path length from the source to the observer (i.e. the ray arrival time). It is noted that the transient response in intervals close to ray arrival times of the TD-UTD are generally the strongest and are directly associated with the waves arriving from the local features of the radiating (scattering) object. The TD-UTD has the same geometrical ray paths as the frequency domain UTD except that each incident, reflected or diffracted TD ray is associated with its corresponding progressing wave in space-time. The TD-UTD fields are polarized transverse to their ray paths as in the conventional frequency domain UTD.

There have been many investigations on the TD diffraction by a straight wedge. Keller and Blank solve the problem of electromagnetic diffraction and reflection of

plane wave pulses by perfectly conducting wedges using the conical flow method [39]. Friedlander solves the corresponding acoustic problem of wedge diffraction [7]. Felsen derives the scattering from a straight wedge (and some other canonical geometries) with various types of illumination [34, 9, 22]. Nikoskinen et al. use a transient image theory to obtain the transient scattering from a PEC wedge [40]. Ianconescu and Heyman solve the pulsed electromagnetic field diffraction by a straight wedge using the Spectral Theory of Transients (STT) [19, 14, 15, 16]. Using the STT, they also extend their results for an incident field which is an astigmatic collimated wavepacket [18, 17]. The work by Ianconescu and Heyman is relevant to the work in this report since they use an analytic time function representation similar to the one used here. Veruttipong and Kouyoumjian obtain a time domain version of the UTD for a straight perfectly conducting wedge [12, 11, 10] by applying an inverse Laplace transform to the corresponding frequency domain UTD wedge diffraction coefficient [2]. Unfortunately, Veruttipong's solution is not easily generalized to the curved wedge case—where the reflected or diffracted rays may pass through smooth or line caustics.

The TD-UTD solution for a perfectly conducting wedge presented in this chapter differs from previous solutions in that the present solution is applicable to the more general problem of diffraction from an arbitrary curved wedge which may contain curved faces and/or a curved edge, while the incident time dependent wavefront is allowed to be astigmatic. It is noted that plane, cylindrical, conical and spherical wavefronts are all special cases of the general astigmatic wavefront which is characterized by two distinct radii of curvature. In fact, Veruttipong's TD diffraction coefficient for the straight wedge [12] can be found as a special case of the solution in this chapter. In addition, this work employs an analytic time function representation for the transient fields where the actual time response is simply the real part of the analytic function, as discussed in the previous chapter. It is shown in this TD-UTD development that the use of analytic time functions allows one to circumvent in a simple manner some complexities that arise when inverting into the TD the UTD ray fields which pass through caustics. These caustics may be produced by reflection and

edge diffraction from general curved geometries. The analytic time functions used here are closely related to the analytic time functions used in the STT [14, 15, 16]. The STT can in general provide an analytical TD impulse response which is valid at all times for some special canonical geometries, but the TD-UTD which is valid for early to intermediate times is immediately applicable to more general and relatively complex geometries due to its ray interpretation.

The format of this chapter is as follows. First the well known frequency domain UTD solution for the curved wedge is briefly presented. In the UTD, the dominant response from the PEC curved wedge is decomposed into the incident field, the reflected field and the edge diffracted field. The edge diffracted field may contain two terms, one is the first order diffracted field while the other is a higher order slope diffracted field. The slope diffracted field is significant when the field incident at the point of diffraction is rapidly varying as a function of space. Then the time domain analytic signal representation for each of these mechanisms is derived to obtain a TD-UTD for the curved wedge. This chapter does not include an analysis of the surface rays excited and diffracted by the edge of a wedge with convex faces, nor does it include the diffraction and excitation of whispering gallery type fields by the edge of a wedge with concave faces. Nonetheless, some curved surface diffraction effects for smooth surfaces are discussed in Chapter IV. The simplification of the TD-UTD wedge diffraction coefficient for some important special cases is also presented. The convolution of the TD-UTD curved wedge impulse response with a more general transient excitation is discussed. Some numerical examples are presented to illustrate the utility of these developments.

3.1 The Frequency Domain UTD Solution for Scattering from a Curved Wedge

The general forms in the frequency domain of the incident, reflected and edge diffracted UTD rays, illustrated in Figures 3.1, 3.2 and 3.3 respectively, are now presented [2, 4, 38].

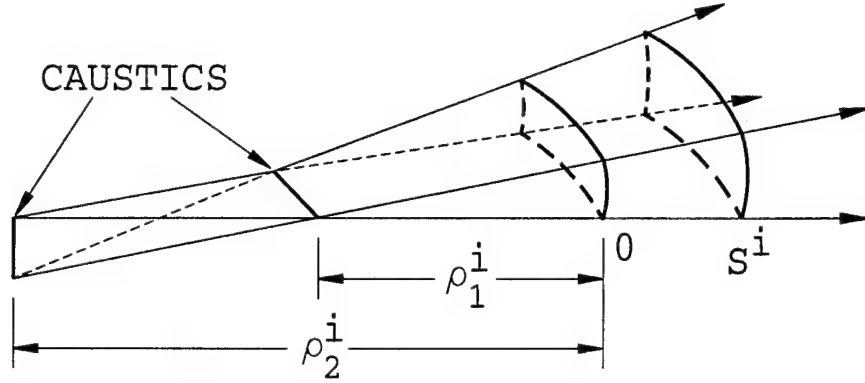


Figure 3.1: An incident geometrical optics (GO) ray tube.

3.1.1 The Frequency Domain Geometrical Optics (GO) Fields

The incident ray shown in Figure 3.1 is a diverging (i.e. convex) wavefront but one could also allow the wavefront to be convergent (i.e. concave) or even saddle shaped. The incident field at the point of reflection or point of diffraction is assumed to be ray optical and may be written as a geometrical optics (GO) ray field such that

$$\tilde{\mathbf{E}}^i(\omega) = \tilde{\mathbf{E}}_0^i(\omega) \left| A_i(s^i) \right| j^{n_i} e^{-jks^i} \quad (3.1)$$

where n^i is the number of line or smooth caustics that the incident GO ray has traversed as in Figure 3.1 and $A_i(s^i)$ is the spreading (or spatial divergence) factor which may be written as

$$A_i(s^i) = \sqrt{\left(\frac{\rho_1^i}{\rho_1^i + s^i} \right) \left(\frac{\rho_2^i}{\rho_2^i + s^i} \right)} \quad (3.2)$$

Note that ρ_1^i and ρ_2^i are the principal radii of curvature of the corresponding wavefront at the reference point O . A GO field reflected from the point Q_R as in Figure 3.2 may be written as

$$\tilde{\mathbf{E}}^r(\omega) = \tilde{\mathbf{E}}^i(\omega) \Big|_{Q_R} \cdot \bar{\mathbf{R}} \left| A_r(s^r) \right| j^{n_r} e^{-jks^r} \quad (3.3)$$

where the dyadic reflection coefficient $\bar{\mathbf{R}}$ is assumed to be independent of frequency and can be written as

$$\bar{\mathbf{R}} = \hat{\mathbf{e}}_{\parallel}^i \hat{\mathbf{e}}_{\parallel}^r R_h + \hat{\mathbf{e}}_{\perp}^i \hat{\mathbf{e}}_{\perp}^r R_s \quad (3.4)$$

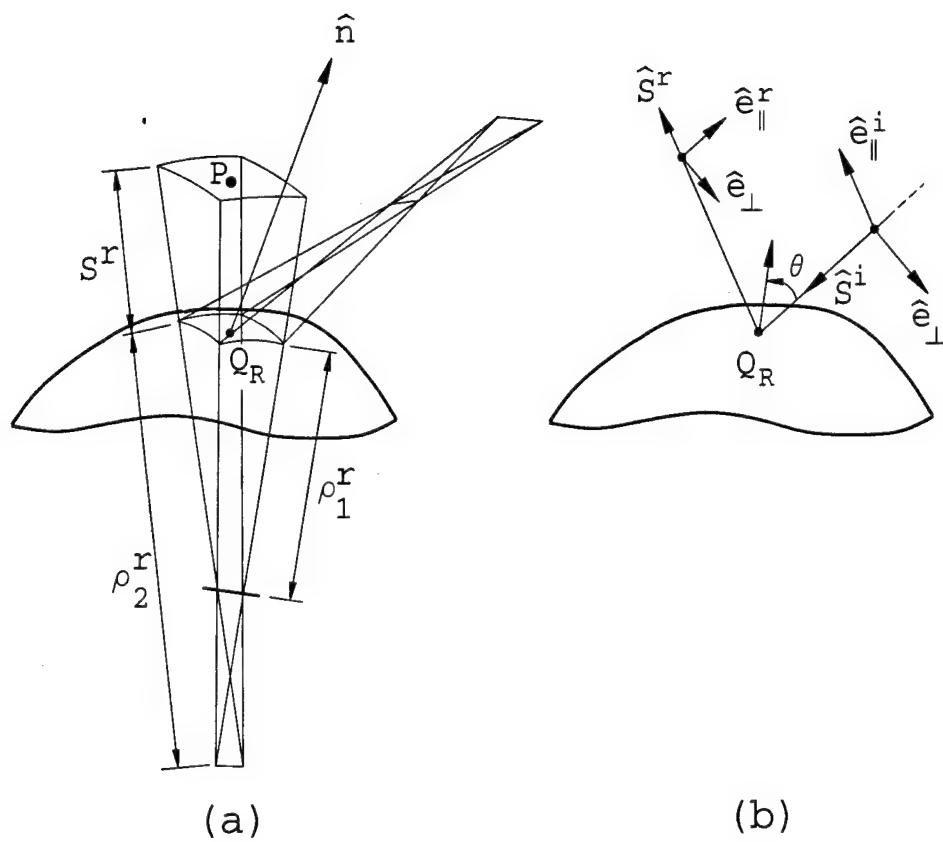


Figure 3.2: A reflected geometrical optics (GO) ray.

where $R_s = -1$ and $R_h = 1$ for a perfect electric conductor. The $A_r(s^r)$ is the spreading factor for the reflected ray which is given by (3.2) with the superscript i replaced by r , and n_r is the number of smooth or line caustics that the reflected ray has traversed after leaving the reflection point Q_R . It is assumed in the UTD that (3.3) represents the field reflected from the unperturbed surface formed by a smooth extension of the original surface past the edge (so that there is no edge effect present in the evaluation of (3.3) as in Figure 3.2).

3.1.2 The Frequency Domain UTD Edge Diffracted Field

The edge diffracted field may be modeled by an edge-diffracted ray as

$$\tilde{\mathbf{E}}^d(\omega) = \tilde{\mathbf{E}}^i(\omega)|_{Q_E} \cdot \tilde{\mathbf{D}}(\omega) |A_d(s^d)| j^{n_d} e^{-jks^d} \quad (3.5)$$

where $A_d(s^d)$ is the spreading factor for the edge diffracted ray, $\tilde{\mathbf{D}}$ is the UTD dyadic diffraction coefficient [4, 2] and n_d is the number of line or smooth caustics that the edge diffracted ray has traversed after leaving the diffraction point Q_E . Note that Equation (3.5) does not include slope diffraction [38, 4].

3.1.3 The Frequency Domain UTD Slope Edge Diffraction

The UTD Slope diffraction is a higher order term which must be added to the edge diffraction term described above when the incident field at the point of diffraction is rapidly varying in a direction transverse to the direction of incidence. In the frequency domain, the slope diffraction is proportional to a spatial derivative of the incident field at the point of edge diffraction. Two versions of the slope diffraction are used here. The first one is by Y. M. Hwang [21, 4]. While the other one is by Veruttipong [20]. The slope diffraction by Hwang is more widely used than Veruttipong's formulation since Hwang's result has a more compact form. Nonetheless, it is interesting to compare these two solutions in the time domain as is done later in this chapter.

The UTD slope diffracted field for both versions has the same form, only the slope diffraction coefficient is different. In general, one can write the total UTD edge

diffracted field as the sum of two terms

$$\tilde{\mathbf{E}}^{dt}(\omega) = \tilde{\mathbf{E}}^d(\omega) + \tilde{\mathbf{E}}^{sd}(\omega) \quad (3.6)$$

where the first order term $\tilde{\mathbf{E}}^d(\omega)$ is given in (3.5) and $\tilde{\mathbf{E}}^{sd}(\omega)$ is the higher order slope diffraction term. The slope diffracted field for a curved wedge can be written as $\tilde{\mathbf{E}}^{sd} = \hat{\beta}_0 \tilde{E}_{\beta_0}^{sd} + \hat{\phi} \tilde{E}_{\phi}^{sd}$ with

$$\begin{bmatrix} \tilde{E}_{\beta_0}^{sd} \\ \tilde{E}_{\phi}^{sd} \end{bmatrix} = \begin{bmatrix} -\tilde{D}^{si} \frac{\partial \tilde{E}_{\beta_0}^i}{\partial n^i} & -\tilde{D}_s^{sr} \frac{\partial \tilde{E}_{\beta_0}^r}{\partial n^r} \\ -\tilde{D}^{si} \frac{\partial \tilde{E}_{\phi}^i}{\partial n^i} & -\tilde{D}_h^{sr} \frac{\partial \tilde{E}_{\phi}^r}{\partial n^r} \end{bmatrix} \left| A_d(s^d) \right| j^{n_d} e^{-jks^d}. \quad (3.7)$$

The extra superscript s on the diffraction coefficients indicates slope diffraction. The result in (3.7) assumes that the incident and reflected field vary rapidly at the edge in the n^i and the n^r directions, respectively. On the other hand, if the diffracted field spreading factor $A_d(s^d)$ is a rapidly varying function then the result in (3.7) is not accurate.

For a straight wedge, this can be simplified to

$$\begin{bmatrix} \tilde{E}_{\beta_0}^{sd} \\ \tilde{E}_{\phi}^{sd} \end{bmatrix} = \begin{bmatrix} -\tilde{D}_s^s \frac{\partial \tilde{E}_{\beta_0}^i}{\partial n^i} \\ -\tilde{D}_h^s \frac{\partial \tilde{E}_{\phi}^i}{\partial n^i} \end{bmatrix} \left| A_d(s^d) \right| j^{n_d} e^{-jks^d}. \quad (3.8)$$

where $\tilde{D}_s^s = \tilde{D}^{si} + \tilde{D}_s^{sr}$ and $\tilde{D}_h^s = \tilde{D}^{si} + \tilde{D}_h^{sr}$. The expressions for the slope diffraction coefficient for both Hwang's and Veruttipong's versions are given in Appendix C where the time domain version of these quantities are derived.

For more information about the parameters in the UTD ray expressions, one may consult the literature [2, 38, 4]. It should be noted that there are also edge excited surface diffracted rays or whispering gallery effects present for a curved wedge geometry; however, the present chapter does not deal with these surface diffracted and whispering gallery type ray fields. Surface diffraction by smooth convex surfaces is addressed in Chapter 4.

3.2 The TD-UTD Impulse Response for a PEC Curved Wedge

The TD-UTD analytic impulse response for a PEC Curved Wedge (not including surface diffracted rays and whispering gallery effects) may be written as

$$\mathbf{E}_I^{\text{UTD}}(t) = \mathbf{E}_I^{\dagger i}(t)U_i + \mathbf{E}_I^{\dagger r}(t)U_r + \mathbf{E}_I^{\dagger d}(t) + \mathbf{E}_I^{\dagger sd}(t) \quad (3.9)$$

where $\mathbf{E}_I^{\dagger i}(t)$, $\mathbf{E}_I^{\dagger r}(t)$, $\mathbf{E}_I^{\dagger d}(t)$ and $\mathbf{E}_I^{\dagger sd}(t)$ are the analytic signal representations for the incident field, the reflected field, the first order edge diffracted field and the slope edge diffracted field, respectively. The field in (3.9) results from an impulsive transient illumination of the wedge as denoted by the subscript I . The analytic impulse response is defined as the response which results when the incident field $\mathbf{E}_I^{\dagger i}(t)$ has an analytic delta function, $\delta^{\dagger}(t)$, time behavior. The spatial unit step functions U_i and U_r are 1 on the lit side of the incident shadow boundary and the reflection shadow boundary, respectively, and 0 otherwise.

Specifically, it is noted that the TD-UTD analytic impulse response of the curved wedge is the response due to an excitation of an astigmatic wavefront with an analytic delta function time behavior. This analytic impulse response is found by setting $\tilde{\mathbf{E}}_0^i(\omega) = \mathbf{E}_0^i$ in (3.1), (3.3), and (3.5), where \mathbf{E}_0^i is a complex constant with respect to frequency, and then applying the analytic time transform in (2.6) to these equations. Finally, these results are combined as shown in (3.9). This procedure provides analytic functions of time where the actual real time responses are found from the real part of these functions evaluated for real time, as discussed in Chapter 2. The response to any desired finite energy pulsed excitation is obtained by performing a convolution of the finite pulsed field excitation with the TD-UTD analytic impulse response.

3.2.1 The TD-UTD Geometrical Optics Field

The incident GO ray field with an analytic impulse time behavior is obtained from (3.1) and (2.6)

$$\mathbf{E}_I^{\dagger i}(t) = \mathbf{E}_0^i j^{n_i} |A_i(s^i)| \delta^{\dagger}(t - s^i/c) \quad (3.10)$$

with the understanding that the actual real time incident field $\mathbf{E}_I^i(t)$ is given by

$$\mathbf{E}_I^i(t) = \text{Re} \left[\mathbf{E}_I^i(t) \right] \quad \text{for } \text{Im } t = 0 \quad (3.11)$$

It is important to note that in general \mathbf{E}_0^i is a complex vector which is constant with respect to frequency for the analytic impulse response and n_i may not be zero; it therefore becomes necessary to define the incident field excitation more precisely as a generalized impulse (or analytic delta function), $\delta^+(t)$. As long as the analytic signal representation of the incident field is a complex constant times the analytic delta function, then the transient response is called the "impulse response". This is consistent when using the analytic time signals, since any transient response due to any other excitation can be found by convolution. The analytic delta function $\delta^+(t)$ was discussed earlier and is given in (2.12). One of the benefits of using the analytic time representation, which is now clearly evident from equations (3.10) and (2.12), is that the analytic time function automatically represents the TD ray field before and after the ray has traversed a caustic or any number of caustics. For example, if the incident ray has not traversed any caustics then $n_i = 0$ and, assuming \mathbf{E}_0^i is real, the real time incident field behavior is

$$\mathbf{E}_I^i(t) = \mathbf{E}_0^i |A_i(s^i)| \delta(t - s^i/c) \quad (3.12)$$

but if the incident ray has traversed one smooth or line caustic then $n_i = 1$ and the real time behavior, assuming \mathbf{E}_0^i is real, is

$$\mathbf{E}_I^i(t) = -\mathbf{E}_0^i |A_i(s^i)| \text{pv} \frac{1}{\pi(t - s^i/c)} \quad (3.13)$$

When the analytic signal representation in (3.10) is used, one does not* have to be concerned about the number of caustics that the ray has traversed, and it avoids the need to do a separate analysis for each case; this is especially important in inverting the diffracted field $\tilde{\mathbf{E}}^d(\omega)$ when a ray caustic is traversed making the analysis of this case rather complicated to get $\mathbf{E}_I^d(t)$ if the analytic signal representation is not used. Note that the ray field description (3.10) breaks down if the observation point is located near a caustic. The reflected ray contribution to the TD-UTD impulse

response is

$$\mathbf{E}_I^+(t) = \mathbf{E}_0^i \cdot \bar{\mathbf{R}} j^{n_i+n_r} |A_i(s^i) A_r(s^r)| \overset{+}{\delta}(\tau_r) \quad (3.14)$$

where $\tau_r = t - s^i/c - s^r/c$. Note that the variable s^i in (3.14) is the distance from the source to the point of reflection Q_R ; whereas, s^i in (3.10) is the straight line distance from the source to the observer. Also, note that the convolution

$$\frac{1}{2} \overset{+}{\delta}(t - s^i/c) * \overset{+}{\delta}(t - s^r/c) = \overset{+}{\delta}(t - s^i/c - s^r/c) \quad (3.15)$$

is used to obtain (3.14).

3.2.2 The TD-UTD Edge Diffracted Field

The first order edge diffracted ray contribution to the TD-UTD impulse response is

$$\mathbf{E}_I^+(t) = \mathbf{E}_0^i \cdot \overset{+}{\mathbf{D}}(\tau_d) j^{n_i+n_d} |A_i(s^i) A_d(s^d)| \quad (3.16)$$

where $\tau_d = t - s^i/c - s^d/c$, and s^i in (3.16) denotes the distance from the source to the point of edge diffraction Q_E . The TD-UTD dyadic diffraction coefficient for a PEC curved wedge is

$$\overset{+}{\mathbf{D}}(t) = -\hat{\beta}'_0 \hat{\beta}_0 \overset{+}{D}_s(t) - \hat{\phi}' \hat{\phi} \overset{+}{D}_h(t) \quad (3.17)$$

where the unit vectors in (3.17) are depicted in Figure 3.3.

Derivation of the TD-UTD Wedge Diffraction Coefficient

The derivation of the TD-UTD dyadic diffraction coefficient for a PEC curved wedge is now presented. The corresponding time harmonic dyadic diffraction coefficient [2] can be written in the following form [11]

$$\tilde{\mathbf{D}}(\omega) = -\hat{\beta}'_0 \hat{\beta}_0 \tilde{D}_s(\omega) - \hat{\phi}' \hat{\phi} \tilde{D}_h(\omega) \quad (3.18)$$

where

$$\tilde{D}_{s,h}(\omega) = -\frac{1}{2n\sqrt{2\pi} \sin \beta_0} \sum_{m=1}^4 K_m^{s,h} \tilde{F}(x_m, \omega) \quad (3.19)$$

The parameters $K_m^{s,h}$ are given by

$$K_1^{s,h} = \cot \left(\frac{\pi + \beta^-}{2n} \right) \quad (3.20)$$

$$K_2^{s,h} = \cot \left(\frac{\pi - \beta^-}{2n} \right) \quad (3.21)$$

$$K_3^{s,h} = \mp \cot \left(\frac{\pi + \beta^+}{2n} \right) \quad (3.22)$$

$$K_4^{s,h} = \mp \cot \left(\frac{\pi - \beta^+}{2n} \right) \quad (3.23)$$

with $\beta^\pm = \phi \pm \phi'$. The x_m are defined by

$$x_1 = L_1 a^+(\beta^-) \quad (3.24)$$

$$x_2 = L_2 a^-(\beta^-) \quad (3.25)$$

$$x_3 = L_3 a^+(\beta^+) \quad (3.26)$$

$$x_4 = L_4 a^-(\beta^+) \quad (3.27)$$

where the L_m parameters are related to the L parameters in [2, 38, 4] by

$$L_1 = L^i \quad (3.28)$$

$$L_2 = L^i \quad (3.29)$$

$$L_3 = L^{rn} \quad (3.30)$$

$$L_4 = L^{ro} \quad (3.31)$$

and $a^\pm(\beta) = 2 \cos^2[(2n\pi N^\pm - \beta)/2]$ where N^\pm is the nearest integer solution of $2\pi n N^\pm - \beta = \pm\pi$. For a thorough explanation of the parameters used in the UTD edge diffraction coefficient, one is referred to the literature [2, 38, 4]. All of the frequency dependence has been collected in the function

$$\tilde{F}(x_m, \omega) = \sqrt{\frac{c}{j\omega}} \tilde{F}_{tr} \left(\frac{\omega x_m}{c} \right) \quad (3.32)$$

where $\tilde{F}_{tr}(z)$ is the conventional UTD transition function defined by

$$\tilde{F}_{tr}(z) = 2j\sqrt{z}e^{jz} \int_{\sqrt{z}}^{\infty} e^{-j\tau^2} d\tau \quad (3.33)$$

The $\tilde{F}(x_m, \omega)$ function can also be written as

$$\tilde{F}(x_m, \omega) = \sqrt{\pi x_m} e^{j\omega x_m/c} \operatorname{erfc} \left(\sqrt{\frac{j\omega x_m}{c}} \right) \quad (3.34)$$

where the complement of the error function is defined as

$$\operatorname{erfc}(z) = \frac{2}{\sqrt{\pi}} \int_z^\infty e^{-t^2} dt \quad (3.35)$$

Note that the function $\tilde{F}(x_m, \omega)$ is not the same as the transition function defined in [2].

The analytic time transform of the frequency domain function $\tilde{F}(x_m, \omega)$ is now derived. The following integral (which may be found in a table of Laplace transforms [28]) is used

$$\int_0^\infty e^{a\tau} \operatorname{erfc}(\sqrt{a\tau}) e^{-p\tau} d\tau = \frac{1}{\sqrt{p}(\sqrt{p} + \sqrt{a})} \quad (3.36)$$

where $-\pi < \arg(p) \leq \pi$ and $-\pi < \arg(a) \leq \pi$. Note that $-\pi < \arg(jx_m) \leq \pi$ and therefore $-3\pi/2 < \arg(x_m) \leq \pi/2$. Now, using the integral in (3.36), the analytic signal corresponding to the frequency domain function $\tilde{F}(x_m, \omega)$ is

$$\tilde{F}^+(x_m, t) = \frac{\sqrt{x_m/\pi}}{\sqrt{-jt}(\sqrt{-jt} + \sqrt{jx_m/c})} \quad (3.37)$$

for $\operatorname{Im} t \geq 0$ where $-\pi < \arg(-jt) \leq \pi$. Notice that the singularity on the real time axis ($\operatorname{Im} t = 0$) is only a branch point singularity and not a pole, and that there is no difficulty in using the expression for $\tilde{F}^+(x_m, t)$ in (3.37) for real time ($\operatorname{Im} t = 0$). Paying close attention to the Riemann sheet on which the parameter x_m is defined (i.e. $-3\pi/2 < \arg(x_m) \leq \pi/2$), (3.37) may be recast into a more convenient form

$$\tilde{F}^+(x_m, t) = \frac{-j\sqrt{-x_m/\pi}}{\sqrt{-jt}(\sqrt{-jt} + e^{-j\pi/4}\sqrt{-x_m/c})} \quad (3.38)$$

for $\operatorname{Im} t \geq 0$ where

$$\sqrt{-x_m} = \begin{cases} j\sqrt{x_m}, & x_m > 0 \\ \sqrt{-x_m}, & x_m < 0 \end{cases} \quad (3.39)$$

and $\operatorname{Re}(\sqrt{-jt}) > 0$. The form in (3.38) is more convenient for numerical computations since most calculators and computer programming languages choose the branch

cut of the square root function to be the negative real axis and then (3.38) may be directly implemented without any "if-then" conditions. Finally, the TD-UTD dyadic diffraction coefficient is given by

$$\overset{\pm}{\mathbf{D}}(t) = -\hat{\beta}'_0 \hat{\beta}_0 \overset{\pm}{D}_s(t) - \hat{\phi}' \hat{\phi} \overset{\pm}{D}_h(t) \quad (3.40)$$

where

$$\overset{\pm}{D}_{s,h}(t) = \frac{-1}{2n\sqrt{2\pi} \sin \beta_0} \sum_{m=1}^4 K_m^{s,h} \overset{\pm}{F}(x_m, t) \quad (3.41)$$

The dyadic diffraction coefficient in (3.17) can be applied to the general geometry of a PEC curved wedge which may have curved faces and a curved edge. Nevertheless, it is interesting to examine some special cases such as a straight wedge and a straight half plane.

Simplification of TD-UTD Diffraction Coefficient for Some Important Special Cases

First, the behavior of the diffraction coefficient near a shadow boundary (SB) is investigated, then the special case geometries of a straight wedge and flat but possibly curved screen are examined.

There are four possible SB locations corresponding to the four terms in (3.41). Define four corresponding angles

$$\epsilon_1 = \pi + (\phi - \phi') \quad (3.42)$$

$$\epsilon_2 = \pi - (\phi - \phi') \quad (3.43)$$

$$\epsilon_3 = \pi + (\phi + \phi') - 2n\pi \quad (3.44)$$

$$\epsilon_4 = \pi - (\phi + \phi'). \quad (3.45)$$

When $\epsilon_m \rightarrow 0^+$ the observer is approaching the m^{th} SB from the lit side. When $\epsilon_m \rightarrow 0$ then $x_m \rightarrow 0$ and it can be shown

$$K_m^{s,h} \sqrt{x_m \pi} \sim C_m^{s,h} n \sqrt{2\pi L_m \text{sgn}(\epsilon_m)} \quad (3.46)$$

where $C_m^{s,h} = 1$ if $m = 1, 2$ and $C_m^{s,h} = \mp 1$ if $m = 3, 4$. Using (3.46), it can be shown that the TD-UTD wedge solution has the same behavior near a SB as the

exact solution in [19] (where Δ_i in Equation (27) in [19] is related to x_2 in this report by $\Delta_i \approx \sqrt{x_2/c}$ near the SB). By using

$$\overset{+}{F}(x_m, t) \sim \sqrt{x_m \pi} \overset{+}{\delta}(t) \quad \text{for } x_m \rightarrow 0 \quad (3.47)$$

with (3.46), it can be shown that the TD-UTD diffracted field has the proper discontinuity which when added to the GO field produces a continuous total field across the SB. This is expected since the same behavior across a SB occurs in the frequency domain UTD.

Assume the two faces of the wedge are flat and the incident GO field is a real impulse in time (i.e. $\delta(t)$) so that all of the L parameters are positive and therefore $x_m > 0$. Now, the analytic time function in (3.38) may be simplified to

$$\overset{+}{F}(x_m, t) = \frac{\sqrt{x_m/\pi}(j\sqrt{t} + \sqrt{x_m/c})}{\sqrt{t}(t + x_m/c)} \quad (3.48)$$

for $\text{Im } t \geq 0$, and the corresponding real time function is

$$F(x_m, t) = \text{Re} \left[\overset{+}{F}(x_m, t) \right] = \frac{x_m/\sqrt{\pi c}}{\sqrt{t}(t + x_m/c)} u(t) \quad (3.49)$$

at $\text{Im } t = 0$ where $u(t)$ is the Heaviside unit step function. Equation (3.49) along with (3.41) is exactly the TD-UTD diffraction coefficient derived by Veruttipong [12], which therefore is a special case of the more general TD-UTD diffraction coefficient presented in this report. The solution may be further simplified by letting $|x_m/(ct)| \rightarrow \infty$, which is justified when the observation point is far away from any SB. When this is done the result in (3.49) may be further simplified to

$$F(t) = \frac{\sqrt{c}}{\sqrt{\pi t}} u(t) \quad (3.50)$$

Equation (3.50) together with (3.41) is what one obtains by taking the inverse Fourier transform of Keller's frequency domain GTD diffraction coefficient [12].

The TD-UTD diffraction coefficient for a flat screen (which may be curved) is found by setting $n = 2$ in (3.41) to obtain

$$\overset{+}{D}_{s,h}(t) = \frac{-1}{2\sqrt{2\pi} \sin \beta_0} \left[\frac{\overset{+}{F}(x_A, t)}{\cos\left(\frac{\phi - \phi'}{2}\right)} \mp \frac{\overset{+}{F}(x_B, t)}{\cos\left(\frac{\phi + \phi'}{2}\right)} \right] \quad (3.51)$$

where

$$x_A = 2L^i \cos^2 \left(\frac{\phi - \phi'}{2} \right) \quad (3.52)$$

$$x_B = 2L^r \cos^2 \left(\frac{\phi + \phi'}{2} \right) \quad (3.53)$$

and

$$L^i = \frac{s^d \rho^i}{\rho^i + s^d} \sin^2 \beta_0 \quad (3.54)$$

$$L^r = \frac{s^d \rho^r}{\rho^r + s^d} \sin^2 \beta_0 \quad (3.55)$$

3.2.3 The TD-UTD Slope Diffraction

The analytic time transform (ATT) can be applied to the higher order frequency domain UTD slope diffraction term in (3.7) to obtain a TD-UTD slope diffraction in closed form.

The TD response corresponding to slope diffraction is

$$\begin{bmatrix} \overset{+}{E}_{\beta_0}^{sd}(t) \\ \overset{+}{E}_{\phi}^{sd}(t) \end{bmatrix} = \frac{1}{2} \begin{bmatrix} -\overset{+}{D}^{si}(t) * \frac{\partial \overset{+}{E}_{\beta_0'}(t)}{\partial n^i} - \overset{+}{D}_s^{sr}(t) * \frac{\partial \overset{+}{E}_{\beta_s'}(t)}{\partial n^r} \\ -\overset{+}{D}^{si}(t) * \frac{\partial \overset{+}{E}_{\phi'}(t)}{\partial n^i} - \overset{+}{D}_h^{sr}(t) * \frac{\partial \overset{+}{E}_{\phi_s'}(t)}{\partial n^r} \end{bmatrix} A_d(s^d) \quad (3.56)$$

with $\overset{+}{E}_I^{sd}(t) = \hat{\beta}_0 \overset{+}{E}_{\beta_0}^{sd}(\tau_d) + \hat{\phi} \overset{+}{E}_{\phi}^{sd}(\tau_d)$. The $*$ denotes a TD convolution. The analytic impulse response is obtained by letting the incident field (and therefore also the reflected field) in (3.56) be impulsive in time.

The TD-UTD slope diffraction coefficient obtained from Hwang's formulation for a straight wedge is derived in Appendix C. Here is the same coefficient generalized for a curved wedge

$$\overset{+}{D}^{si}(t) = \frac{-1}{4n^2 \sqrt{2\pi} \sin^2 \beta_0} [C_1 \overset{+}{F}_s(x_1, t) - C_2 \overset{+}{F}_s(x_2, t)] \quad (3.57)$$

$$\overset{+}{D}_{s,h}^{sr}(t) = \frac{\mp 1}{4n^2 \sqrt{2\pi} \sin^2 \beta_0} [C_3 \overset{+}{F}_s(x_3, t) - C_4 \overset{+}{F}_s(x_4, t)], \quad (3.58)$$

$$\overset{+}{F}_s(x_m, t) = \sqrt{\frac{c}{\pi}} \frac{2x_m e^{-j\pi/4}}{\sqrt{-jt} + e^{-j\pi/4} \sqrt{-x_m/c}}, \quad (3.59)$$

$$C_1 = \csc^2 \left(\frac{\pi + \beta^-}{2n} \right) \quad (3.60)$$

$$C_2 = \csc^2 \left(\frac{\pi - \beta^-}{2n} \right) \quad (3.61)$$

$$C_3 = \csc^2 \left(\frac{\pi + \beta^+}{2n} \right) \quad (3.62)$$

$$C_4 = \csc^2 \left(\frac{\pi - \beta^+}{2n} \right) \quad (3.63)$$

The TD-UTD slope diffraction coefficient for a straight wedge obtained from Veruttipong's formulation is derived in Appendix C. Here is the same coefficient generalized for a curved wedge

$$\overset{+}{D}^{si}(t) = \frac{-1}{4n^2 \sqrt{2\pi} \sin^2 \beta_0} \sum_{m=1}^2 A_m \overset{+}{F}_{vs}(x_m, t) + B_m \overset{+}{F}_s(x_m, t) \quad (3.64)$$

$$\overset{+}{D}_{s,h}^{sr}(t) = \frac{\mp 1}{4n^2 \sqrt{2\pi} \sin^2 \beta_0} \sum_{m=3}^4 A_m \overset{+}{F}_{vs}(x_m, t) + B_m \overset{+}{F}_s(x_m, t) \quad (3.65)$$

where $\overset{+}{F}_s(x_m, t)$ is defined in (3.59),

$$A_1 = \csc^2 \left(\frac{\pi + \beta^-}{2n} \right) - B_1 \quad (3.66)$$

$$A_2 = \csc^2 \left(\frac{\pi - \beta^-}{2n} \right) - B_2 \quad (3.67)$$

$$A_3 = \csc^2 \left(\frac{\pi + \beta^+}{2n} \right) - B_3 \quad (3.68)$$

$$A_4 = \csc^2 \left(\frac{\pi - \beta^+}{2n} \right) - B_4 \quad (3.69)$$

and

$$B_1 = + \frac{n\dot{a}^+(\beta^-)}{a^+(\beta^-)} \cot \left(\frac{\pi + \beta^-}{2n} \right) \quad (3.70)$$

$$B_2 = - \frac{n\dot{a}^-(\beta^-)}{a^-(\beta^-)} \cot \left(\frac{\pi - \beta^-}{2n} \right) \quad (3.71)$$

$$B_3 = + \frac{n\dot{a}^+(\beta^+)}{a^+(\beta^+)} \cot \left(\frac{\pi + \beta^+}{2n} \right) \quad (3.72)$$

$$B_4 = - \frac{n\dot{a}^-(\beta^+)}{a^-(\beta^+)} \cot \left(\frac{\pi - \beta^+}{2n} \right) \quad (3.73)$$

with

$$a^\pm(\beta) = 2 \cos^2 \left(\frac{2\pi n N^\pm - \beta}{2} \right) \quad (3.74)$$

$$\dot{a}^{\pm}(\beta) = \sin(2n\pi N^{\pm} - \beta) \quad (3.75)$$

The other analytic time function is

$$\begin{aligned} \overset{+}{F}_{vs}(x_m, t) = & \frac{2c\sqrt{-x_m}}{\sqrt{\pi}} \left[\ln \left| \frac{e^{j\pi/4}\sqrt{-jct} + \sqrt{-x_m}}{\sqrt{-x_m}} \right| \right. \\ & \left. + j \arg \left(e^{j\pi/4}\sqrt{-jct} + \sqrt{-x_m} \right) - j\frac{\pi}{2} \right] \end{aligned} \quad (3.76)$$

where $\arg(z)$ is the argument (phase angle) of the complex number z , $\sqrt{-x_m}$ is defined in (3.39) and $\text{Re } \sqrt{-jt} > 0$.

Although the slope diffraction coefficients in (3.57) and (3.58) (or (3.64) and (3.65)) have been generalized for a curved wedge, one must be careful when the illuminated wedge face is curved. In fact, the slope diffracted field presented here will not fully compensate for the discontinuous spatial derivative in the reflected field when the reflecting surface is curved. Nonetheless, the slope diffracted field presented here will provide a good approximation for many practical situations. For a more detailed discussion on this problem one is referred to the thesis by Zheng [41].

3.3 Some Numerical Examples

First, this section presents a convenient expansion of a general transient wave excitation which can be convolved in closed form with the TD-UTD impulse response of the curved wedge, next some numerical examples are included to illustrate the utility of the concepts developed in this chapter. In this section, Hwang's version of slope diffraction (instead of Veruttipong's version) is used unless stated otherwise.

Convolution of the TD-UTD Impulse Response with a General Pulsed Astigmatic Wave Excitation

It is easy to examine the impulse response provided by the TD-UTD formulas derived in the last section, but there are two important reasons why one should be interested in different types of excitations besides an impulsive wavefront. The first reason is because the TD-UTD is based on the asymptotic (high frequency) formulas of the time harmonic UTD and therefore the "late time" behavior of the TD-UTD impulse

response is expected to be erroneous. On the other hand, if the TD-UTD impulse response is convolved with an excitation waveform which has a frequency spectrum, $\tilde{\mathbf{E}}_0^i(\omega)$ as in (3.1), dominated by frequencies for which the time harmonic UTD solution is expected to be accurate then the transient waveforms predicted by the TD-UTD should be very accurate also. The second reason is because in real physical situations the frequency spectrum of pulsed fields which can propagate without dispersion is limited. Also, there is typically a lower limit on the frequency which a source can radiate. Therefore the response due to an excitation waveform which has an effectively band limited frequency spectrum, $\tilde{\mathbf{E}}_0^i(\omega)$, and of finite time duration is more realistic. Furthermore, one must convolve the TD-UTD impulse response with a more realistic excitation in order to predict or compare with measurements or other numerical calculations.

Numerical convolution of any given excitation time waveform with the impulse response formulas in the previous section is always possible, but it may not be the most efficient approach. A different approach which is typically more efficient for narrow pulse (i.e. wide band) excitations is to express the excitation waveform as a sum of a small number of simple expansion functions which can be convolved with the TD-UTD impulse response in closed form. One choice of a very simple expansion function is a waveform whose analytic signal representation is a simple pole in the complex time plane. First, assume that the frequency response of each vector component in the excitation $\tilde{\mathbf{E}}_0^i(\omega)$ is the same, so that

$$\tilde{\mathbf{E}}_0^i(\omega) = \hat{\mathbf{p}} \tilde{F}_0^i(\omega) \quad (3.77)$$

where $\hat{\mathbf{p}}$ is a polarization unit vector, and $\tilde{F}_0^i(\omega)$ is the Fourier transform of the excitation time waveform $F_0^i(t)$. Let

$$F_0^i(t) = \text{Re} \left[\tilde{F}_0^i(t) \right] = \text{Re} \left[\frac{j}{\pi} \sum_{n=1}^N \frac{A_n}{t + j\alpha_n} \right] \quad (3.78)$$

with a frequency response of

$$\tilde{F}_0^i(\omega) = \sum_{n=1}^N A_n e^{-\alpha_n \omega}, \quad \omega \geq 0 \quad (3.79)$$

The parameters $\{A_n\}$ and $\{\alpha_n\}$ are in general complex. Now, suppose the analytic impulse response is $\tilde{\mathbf{E}}_I^{\text{UTD}}(t)$, then using the convolution property in Table 2.1 and the excitation in (3.78), the response of the curved wedge to a pulsed astigmatic wave is

$$\tilde{\mathbf{E}}^{\text{UTD}}(t) = \frac{1}{2} \tilde{F}_0^i(t) * \tilde{\mathbf{E}}_I^{\text{UTD}}(t) \quad (3.80)$$

$$= \sum_{n=1}^N A_n \tilde{\mathbf{E}}_I^{\text{UTD}}(t + j\alpha_n) \quad (3.81)$$

and the real response $\mathbf{E}^{\text{UTD}}(t)$ is the real part of (3.80) with $\text{Im } t = 0$. Notice that as long as $\text{Re } \alpha_n > 0$ for all n , the analytic function resulting from the convolution in (3.80) is analytic on the real time axis ($\text{Im } t = 0$) and therefore $\mathbf{E}^{\text{UTD}}(t)$ is bounded and well behaved.

A convenient frequency domain window function, which satisfies the more general form in (3.79), is

$$\tilde{F}_0^i(\omega) = C_0(1 - e^{-\omega T})^N e^{-\omega MT} \quad (3.82)$$

where

$$T = \frac{1}{2\pi f_c} \ln \left(\frac{M + N}{M} \right) \quad (3.83)$$

and f_c is the center frequency. The peak of the window $\tilde{F}_0^i(\omega)$ is normalized to one by choosing

$$C_0 = \left(\frac{M + N}{M} \right)^M \left(\frac{M + N}{N} \right)^N \quad (3.84)$$

An Example: Scattering from a Two-dimensional Curved Strip

Figure 3.4 shows the geometry of a two dimensional curved parabolic strip. The strip is excited by an incident plane wave with the electric field polarized perpendicular to the plane of the paper. The observation point P , as shown in Figure 3.4, is near the reflection shadow boundary (RSB) of edge (1). Figure 3.5 shows the impulse response calculated using the TD-UTD when the dominant three scattering mechanisms are included. Figure 3.6 shows the impulse response corresponding to each scattering mechanism separately, namely the reflected field, the diffracted field from edge (1)

and the diffracted field from edge (2). Notice that the contribution to the impulse response from the edge diffracted ray from edge (1) appears to be very close to -0.5 times the reflected ray contribution to the impulse response. This is to be expected since the observation point is very near to the RSB of edge (1). For verification, the impulse response predicted by the TD-UTD is convolved with a finite (band limited) excitation and then compared with a reference solution. For the frequency domain window shown in the inset in Figure 3.7, the parameters in the window function of (3.82) are $f_c = 20$ GHz, $M = 1$ and $N = 2$.

The reference solution is based on a frequency domain method of moments (MM) analysis which has been weighted by the appropriate frequency window and transformed numerically into the time domain using an inverse fast Fourier transform (FFT). As can be seen in Figure 3.7, the reference solution MM+FFT and the TD-UTD result are almost indistinguishable from each other.

Electric Dipole Illuminating a Wedge

Figure 3.8 shows the space-time behavior of the total far zone field as predicted by the TD-UTD when a PEC wedge is illuminated by an infinitesimal electric current element. The curves are calculated by a convolution of the TD-UTD impulse response with a smooth finite energy time pulse with a frequency response described by

$$\tilde{F}(\omega) = C e^{-\alpha\omega} (1 - e^{-\alpha\omega}) \quad \text{for } \omega > 0 \quad (3.85)$$

where C and α are constants. The dipole is pointed just 5 degrees off the direction to the edge, so that the incident field is non-zero and rapidly varying at the edge. This is done so that both the first order and slope diffraction are significant. The diffracted field is much smaller than the incident or reflected field and is difficult to see in Figure 3.8. Nonetheless, notice that the total field is a smooth and continuous function of both space and time. This is expected since the TD-UTD diffracted field corrects the discontinuities of the geometrical optics (GO) field at the shadow boundaries.

Figure 3.9 is similar to Figure 3.8 except it shows the first order diffracted field. The field is also multiplied by a factor of 10 to make it visible on this plot scale.

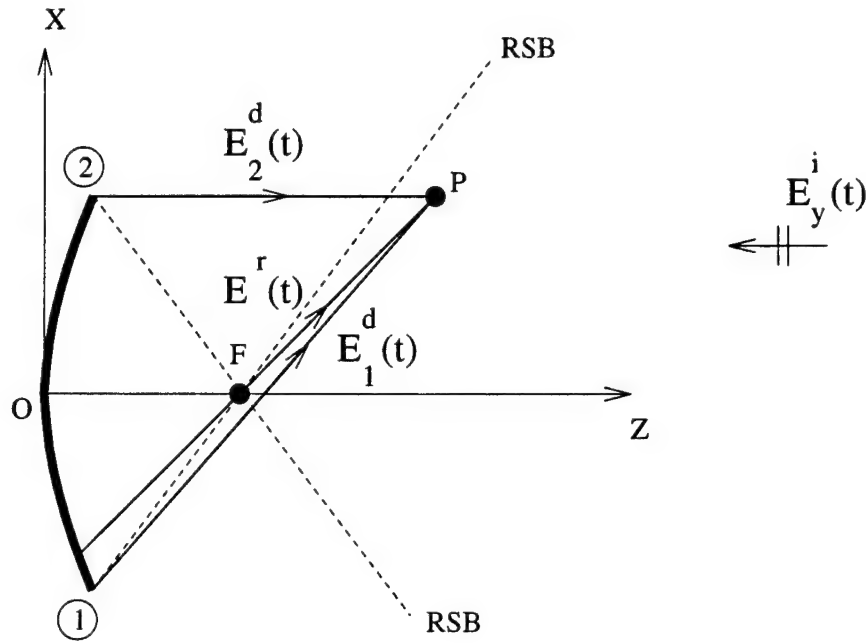


Figure 3.4: Two dimensional parabolic strip geometry. The focus is located at $F(x=0, z=4)$, the width of the aperture is 8, and the observation point is $P(x=4, z=8)$. All linear dimensions are in centimeters.

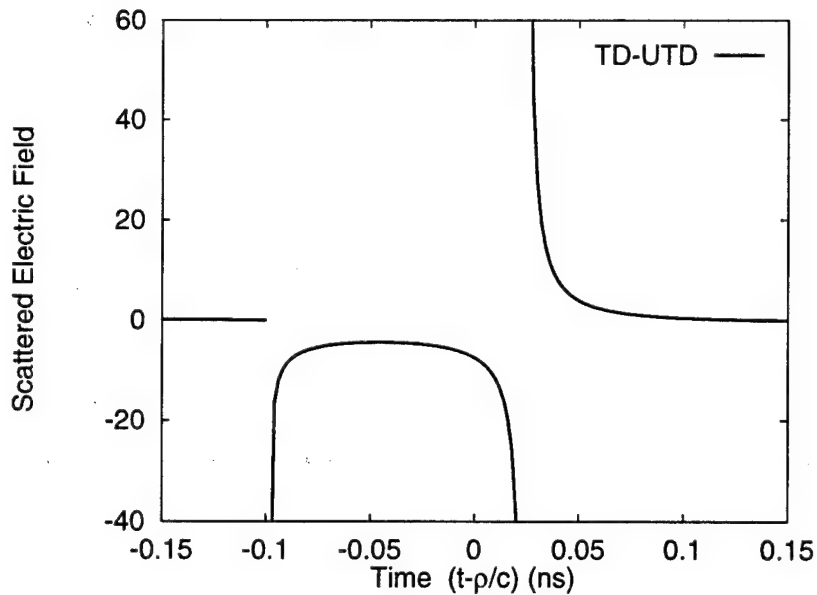


Figure 3.5: The TD-UTD scattered field at the observation point P when the 2-D parabolic strip in Figure 5 is excited by an impulsive plane wave. The time axis is shifted by ρ/c for convenience where ρ is the distance of P from the origin and c is the speed of light.

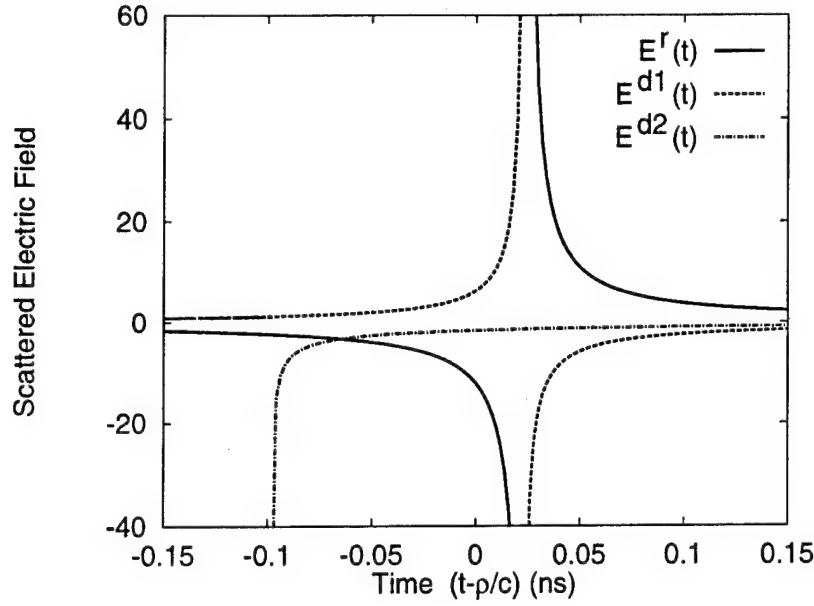


Figure 3.6: The impulse response for each scattering mechanism is plotted here separately, where $E^r(t)$, $E^{d1}(t)$ and $E^{d2}(t)$ correspond to the impulse response of the reflected ray, the edge-diffracted ray from edge (1) and the edge-diffracted ray from edge (2), respectively. The time axis is shifted by ρ/c for convenience.

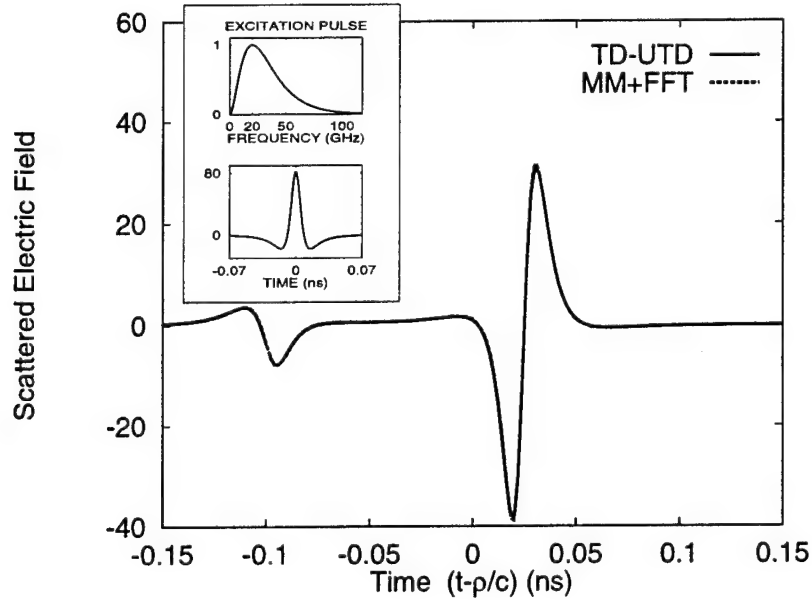


Figure 3.7: Same as in Figure 6 except that the incident temporal excitation is a finite energy time waveform.

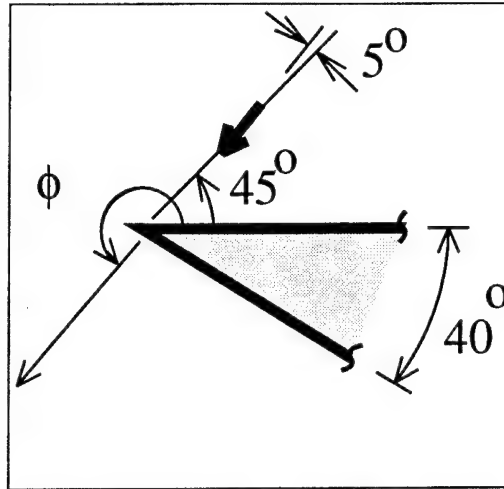
Notice that the first order diffracted field is discontinuous as a function of angle at the shadow boundaries. This discontinuity corrects the discontinuous GO field at these boundaries.

Figure 3.10 is similar to Figures 3.9 and 3.8, except it shows the slope diffracted field. Notice that the slope diffracted field is a smooth function of both space (angle) and time, but it does have a discontinuous derivative as a function of angle at the shadow boundaries, which corrects the discontinuous derivative of the GO plus first order diffracted field.

Figures 3.11, 3.12 and 3.13 compare the TD-UTD impulse response with an exact solution. The exact solution is presented in Appendix B and is based on Felsen's work [22]. The PEC wedge is illuminated by a infinitesimal current element where the current has a unit step function time dependence. This illuminates the wedge with a spherical wave, and the first order term in $(1/r)$ has an impulsive time dependence. The TD-UTD solution assumes that the incident field is a time impulsive spherical wave with a $(1/r)$ distance dependence. Figure 3.14 is a closeup view of the plots in Figure 3.13. The TD-UTD based on Veruttipong's work is labeled "TD-UTD (Ver)" and the one based on Hwang's work is labeled "TD-UTD (Hwa)". Notice that the TD-UTD slope diffraction solution based on Veruttipong's work is more accurate for early time, whereas the TD-UTD slope diffraction based on Hwang's work is more accurate for intermediate to late time. This is anticipated from the equations since the formulation based on Veruttipong's work contains an approximation for a higher order term in the frequency domain asymptotic expansion. Nonetheless, it appears from these simple examples that the solution based on Hwang's work is adequate for many applications and is still a simple and more compact formulation. *

Magnetic Dipole Illuminating a Wedge

The comparison in Figures 3.15 and 3.16 is similar to Figures 3.13 and 3.14 except the wedge is excited by an infinitesimal magnetic current element. Figure 3.16 is simply a close up view of the bottom plot in Figure 3.15. The TD-UTD slope diffraction based on Veruttipong's work is labeled "TD-UTD (Ver)" and the one based on Hwang's



Electric Dipole and PEC Wedge, Total Field

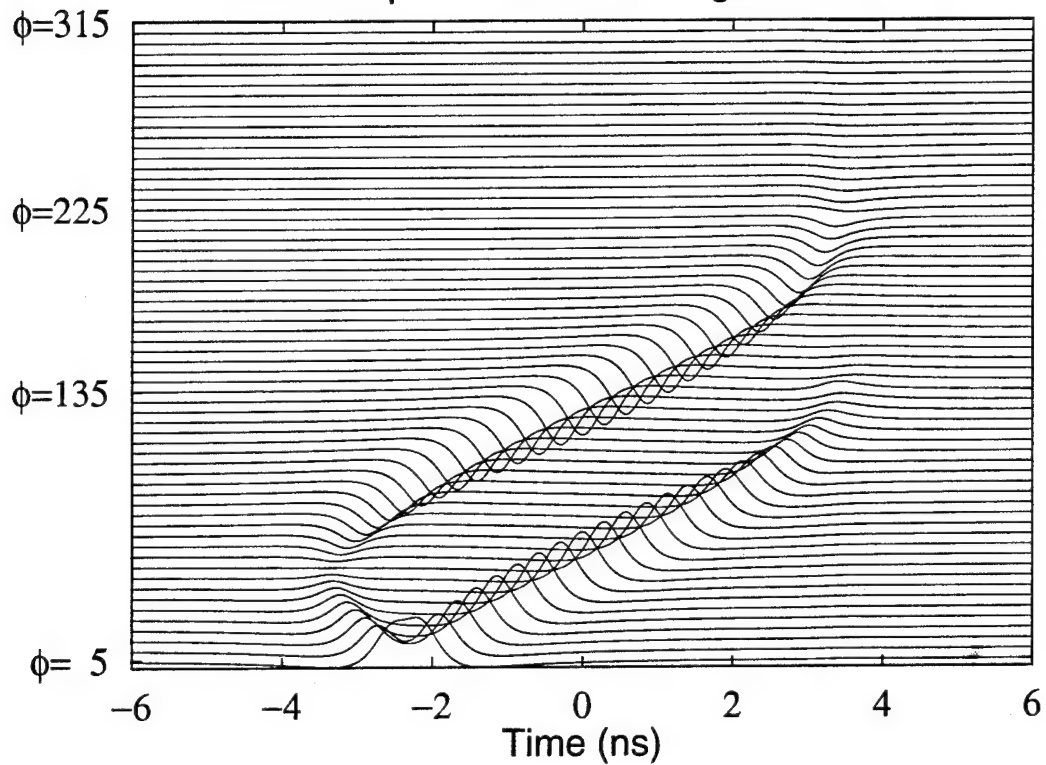
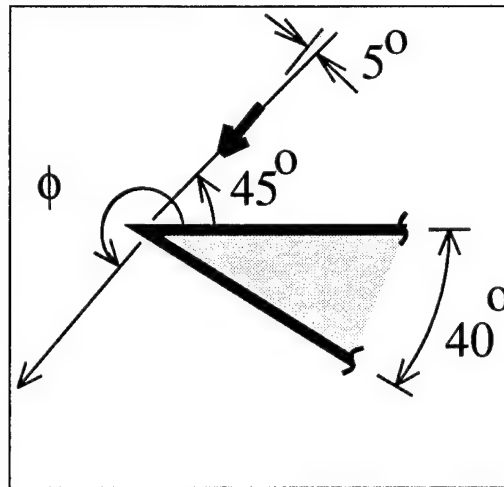


Figure 3.8: A waterfall plot showing the space-time behavior of the total field when an electric dipole illuminates a PEC wedge. The observer is in the far zone and the incident field at the edge is rapidly varying so slope diffraction is significant.



Electric Dipole and PEC Wedge, Diffracted Field (10x)

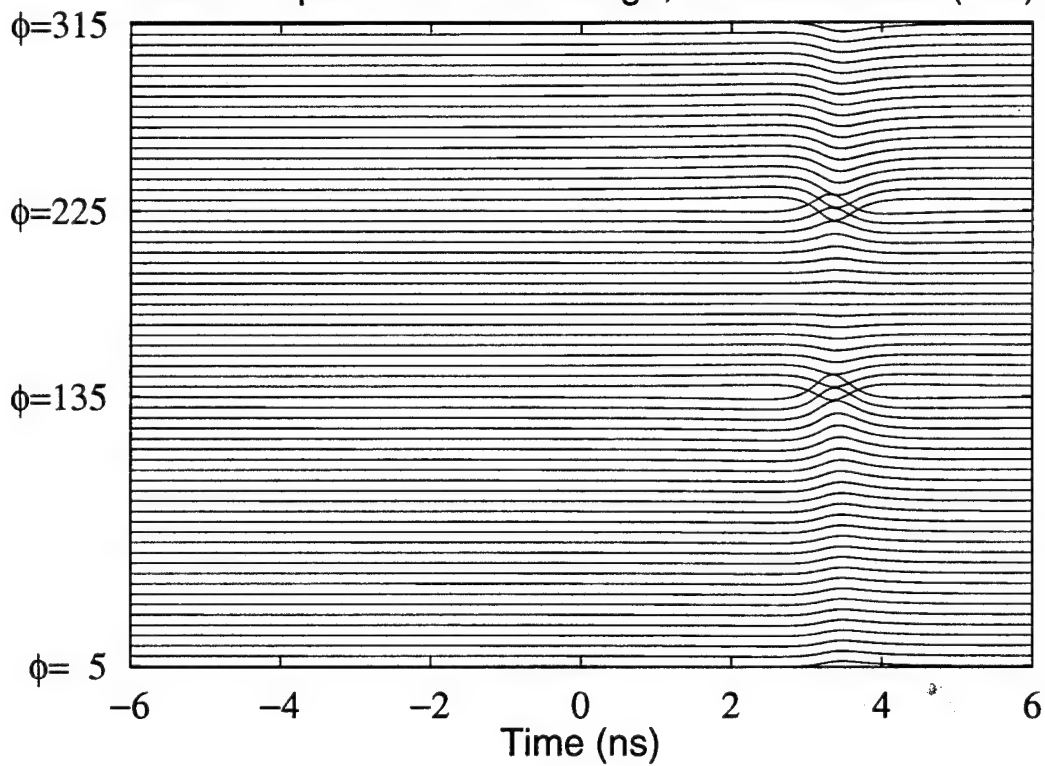
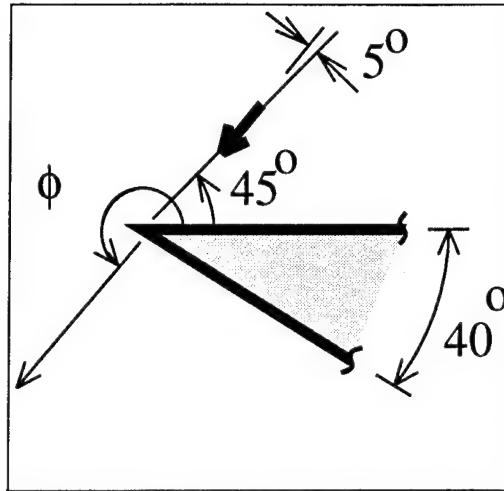


Figure 3.9: A waterfall plot showing the space-time behavior of the first order diffracted field when an electric dipole illuminates a PEC wedge and the observer is in the far zone. The field here is multiplied by a factor of 10 as compared with Figure 3.8.



Electric Dipole and PEC Wedge, Slope Diffraction (10x)

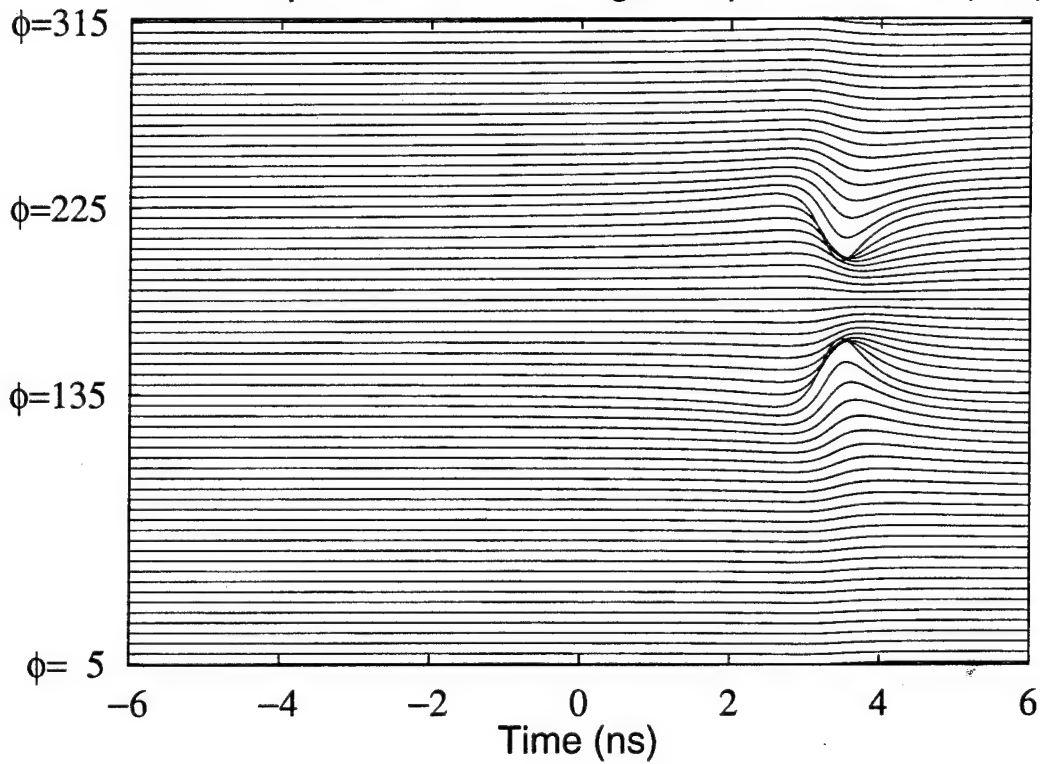


Figure 3.10: A waterfall plot showing the space-time behavior of the slope diffracted field (Hwang's version) when an electric dipole illuminates a PEC wedge. The observer is in the far zone. The field here is multiplied by a factor of 10 as compared with Figure 3.8.

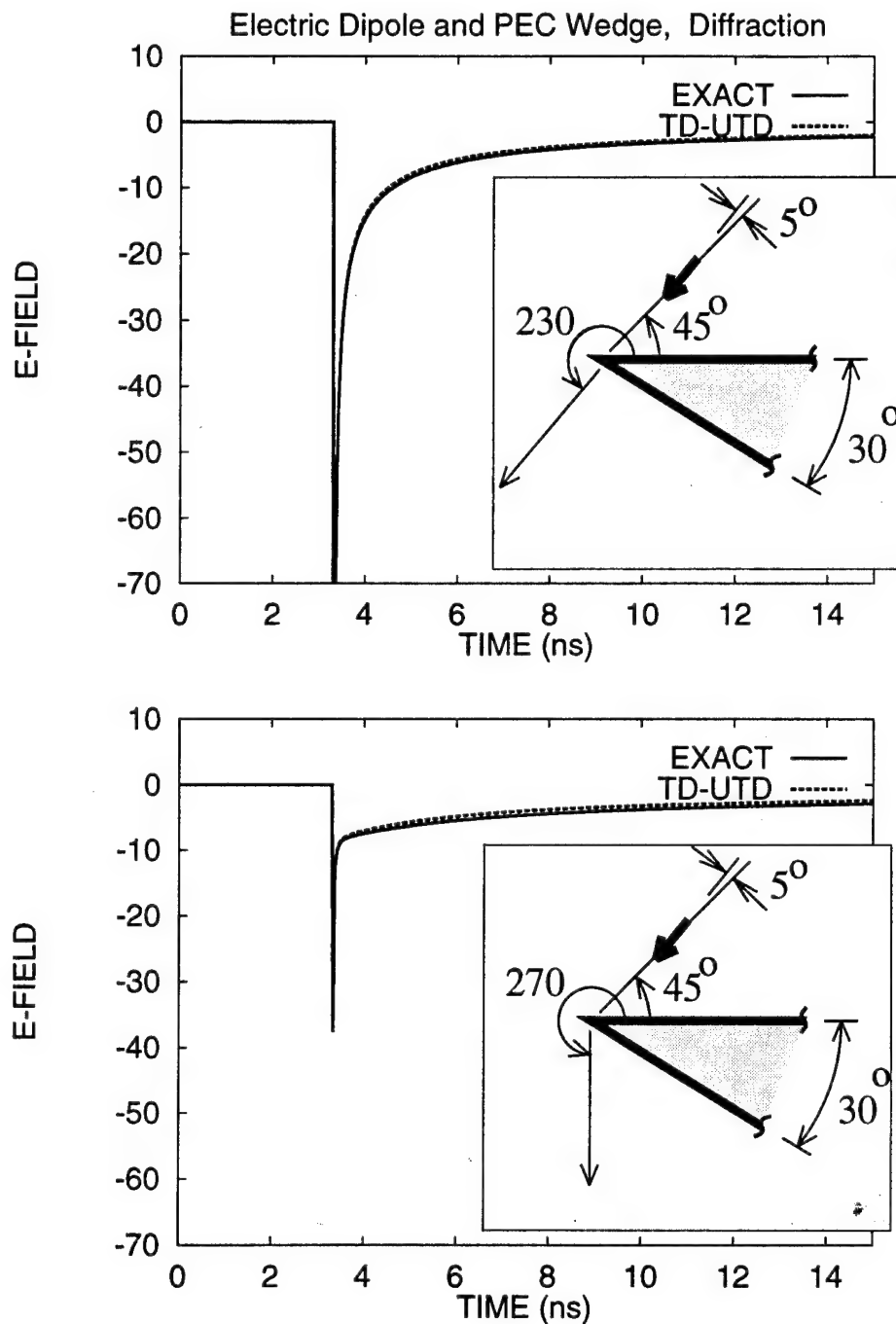


Figure 3.11: The TD-UTD impulse response is compared with an exact result. The infinitesimal electric current has a unit step time behavior which approximately illuminates the wedge with an impulsive spherical wave.

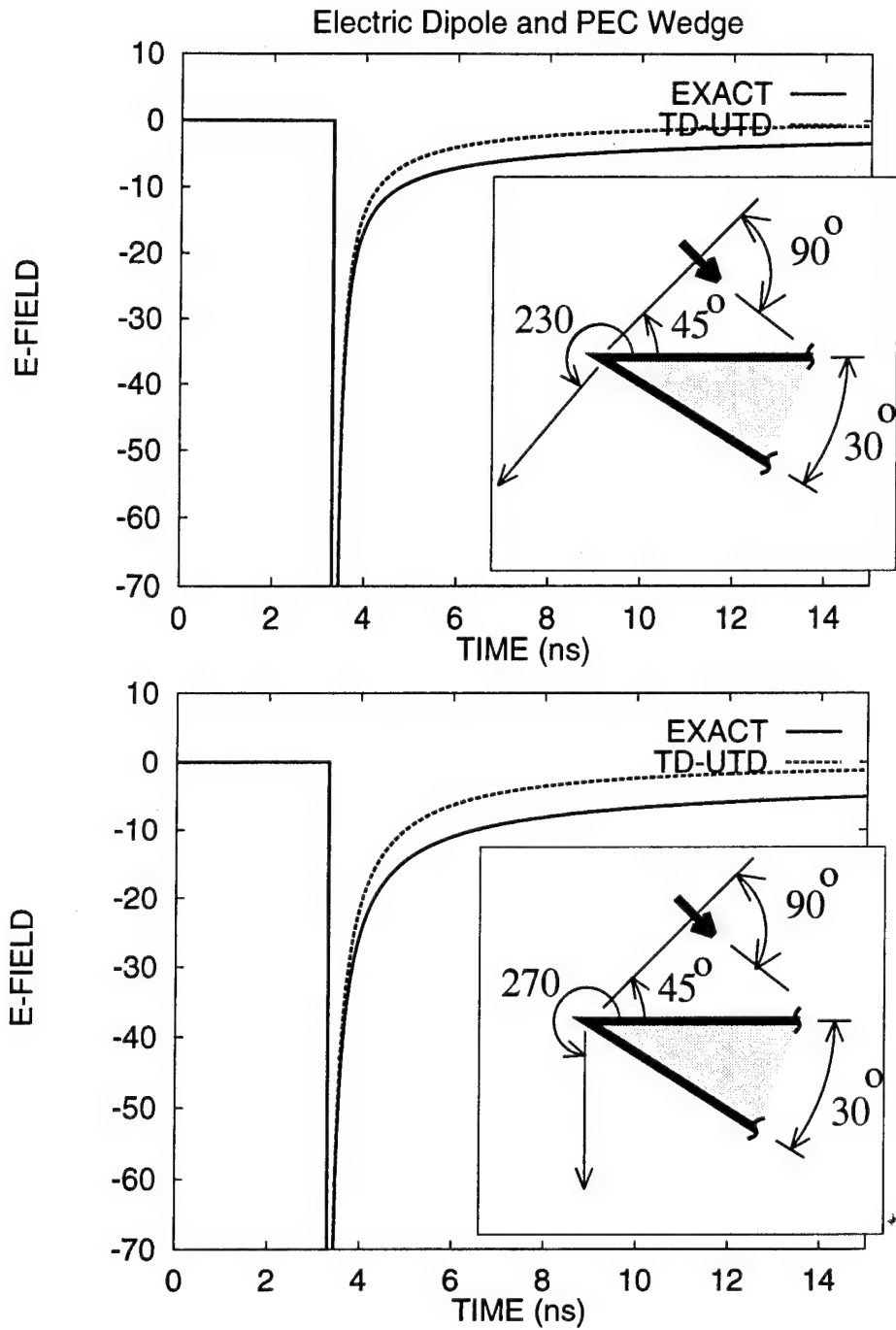


Figure 3.12: The TD-UTD impulse response is compared with an exact result. The infinitesimal electric current has a unit step time behavior which approximately illuminates the wedge with an impulsive spherical wave. The slope diffraction is zero when the dipole is oriented perpendicular to the incident direction.

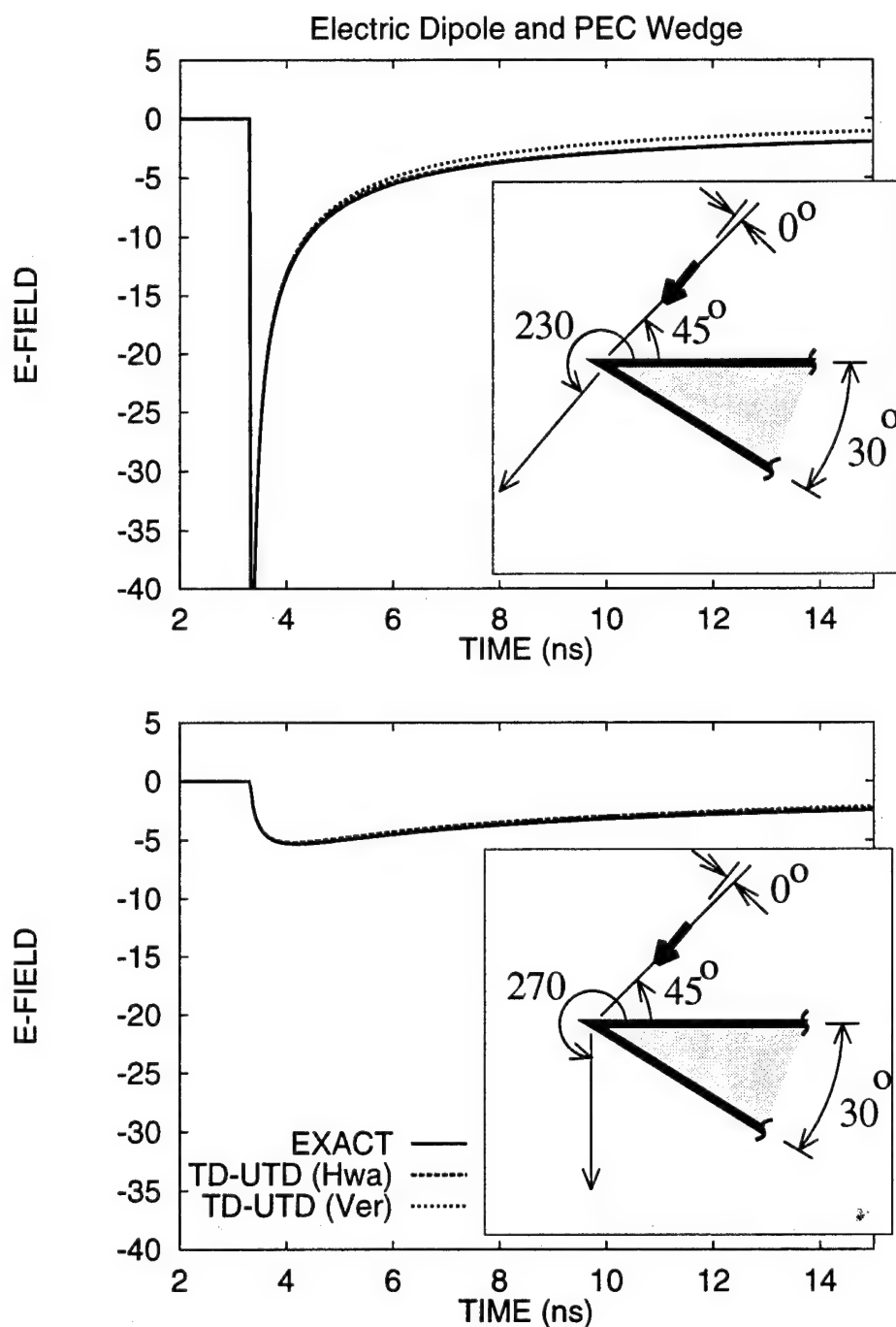


Figure 3.13: The two versions of the TD-UTD slope diffraction are compared with an exact result. The infinitesimal electric current has a unit step time behavior which approximately illuminates the wedge with an impulsive spherical wave.

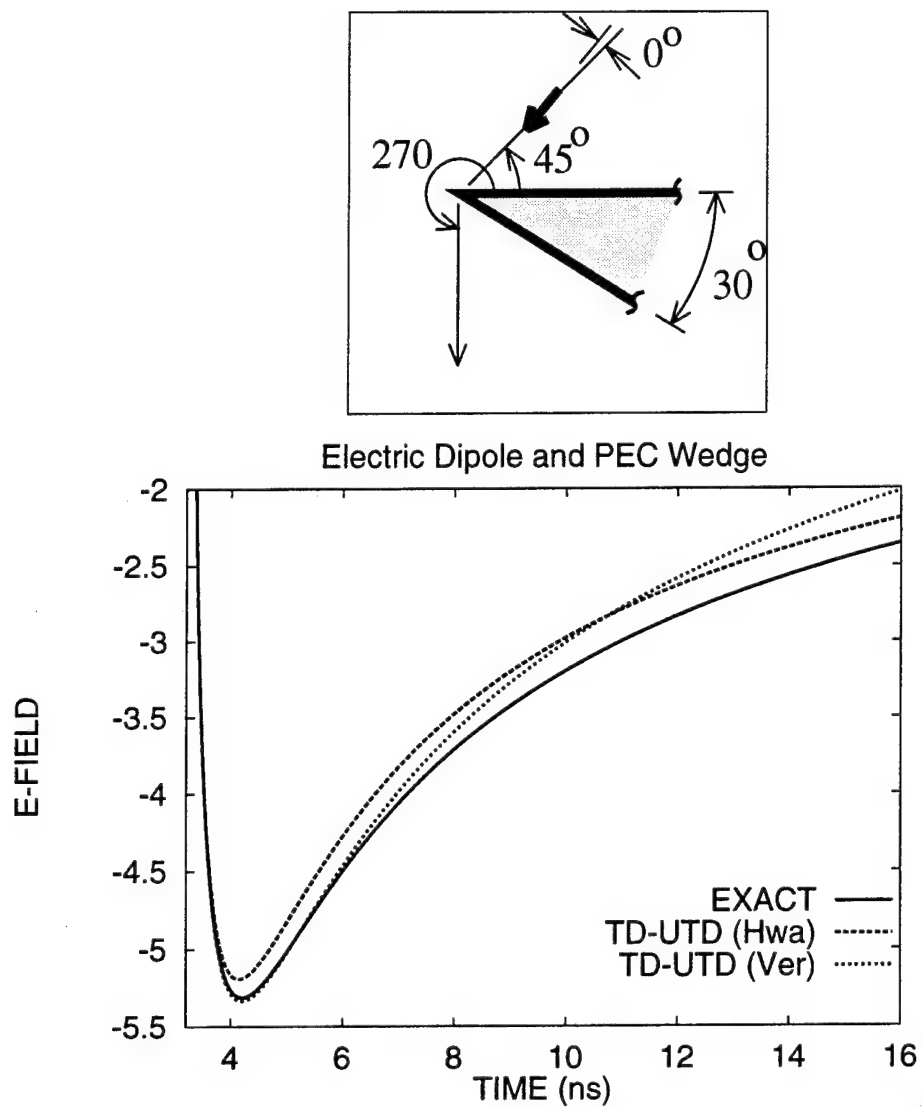


Figure 3.14: The two versions of the TD-UTD slope diffraction are compared with an exact result. The infinitesimal electric current has a unit step time behavior which approximately illuminates the wedge with an impulsive spherical wave.

work is labeled "TD-UTD (Hwa)". The magnetic current element is placed directly on one of the wedge faces, since this could be used to model a small slot antenna. Notice that there is excellent agreement for an observer near the shadow boundary and far from the shadow boundary. Also, notice that once again the TD-UTD based on Veruttipong's work is more accurate for early time; whereas, the formulation based on Hwang's work is more accurate for intermediate to late time as expected.

3.4 Conclusions

The TD-UTD solution for the scattered field from a general curved wedge is summarized as follows. The TD-UTD impulse response for the field in the presense of a general curved wedge may be written as

$$\mathbf{E}_I^{\text{UTD}}(t) = \mathbf{E}_I^i(t)U_i + \mathbf{E}_I^r(t)U_r + \mathbf{E}_I^d(t) + \mathbf{E}_I^{sd}(t) \quad (3.86)$$

where the spatial unit step functions U_i and U_r are 1 on the lit side of the incident shadow boundary and the reflection shadow boundary, respectively, and 0 otherwise. The TD-UTD incident GO field $\mathbf{E}_I^i(t)$ is in (3.10) and the TD-UTD reflected field $\mathbf{E}_I^r(t)$ is in (3.14). The first order TD-UTD edge diffracted field $\mathbf{E}_I^d(t)$ is in (3.16) where the TD-UTD dyadic diffraction coefficient is defined in (3.40) and (3.41). The higher order edge diffracted field called the slope diffracted field $\mathbf{E}_I^{sd}(t)$ is in (3.56) where the TD-UTD dyadic slope diffraction coefficient based on Hwang's frequency domain UTD slope result is given in (3.57) and (3.58) while the slope diffraction coefficient based on Veruttipong's frequency domain UTD result is given in (3.64) and (3.65). Finally, the impulse response formulas, denoted by the subscript I , may be convolved with an excitation in closed form as in (3.80) and (3.81) when the excitation has the form in (3.77) or (3.78).

This chapter presents a time domain version of the UTD (TD-UTD) for the general case of a curved PEC wedge, where the wedge faces and the edge may be curved. This time domain solution can handle more general geometries than what has been done in the past and supplies a good stepping stone for the development of a complete

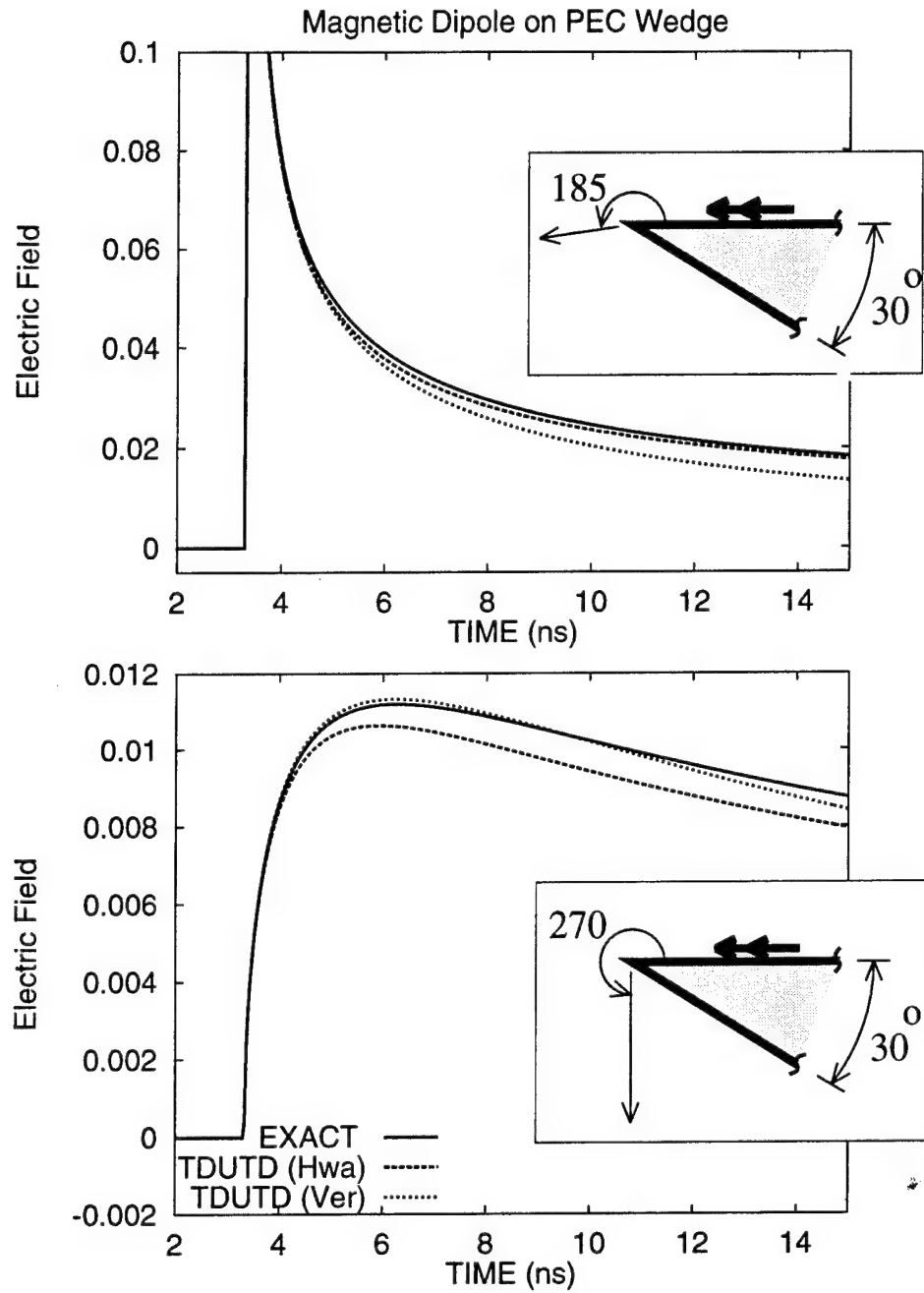


Figure 3.15: The two versions of the TD-UTD slope diffraction are compared with an exact result. The infinitesimal magnetic current has a unit step time behavior which approximately illuminates the wedge with an impulsive spherical wave.

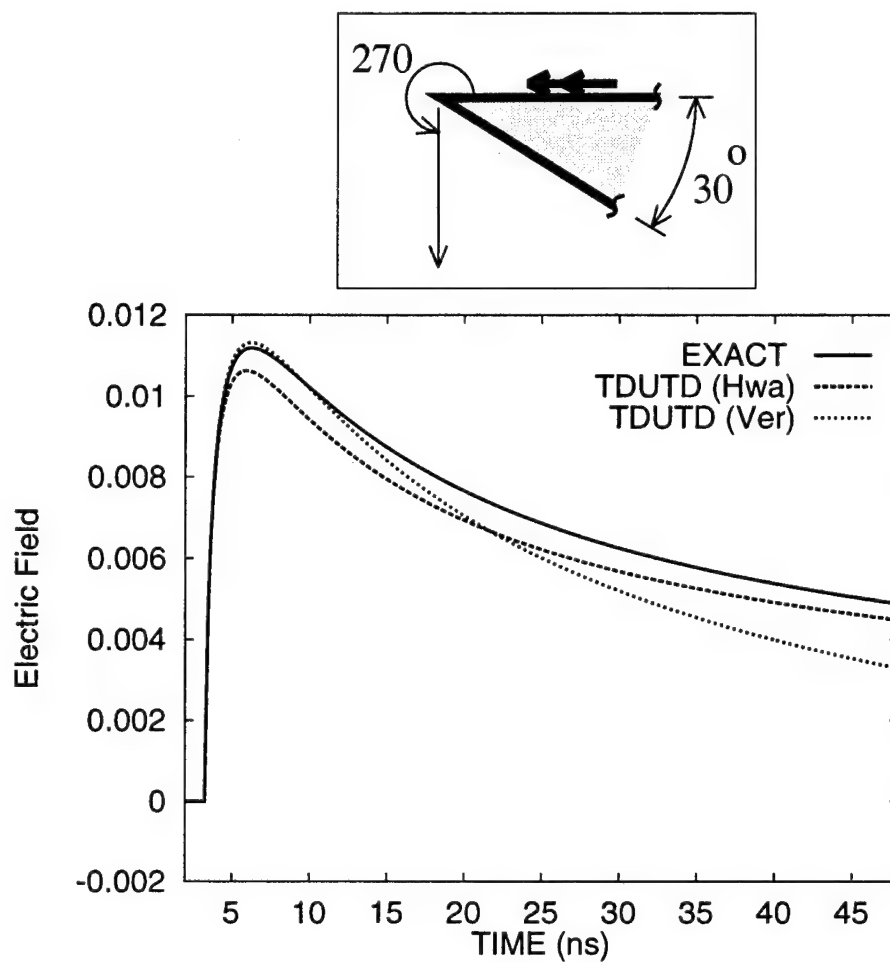


Figure 3.16: The two versions of the TD-UTD slope diffraction are compared with an exact result. The infinitesimal magnetic current has a unit step time behavior which approximately illuminates the wedge with an impulsive spherical wave.

TD-UTD which includes multiple diffractions, caustic corrections, surface diffraction, etc.

Chapter 4

TD-UTD for a Smooth Convex Surface

The study of electromagnetic surface diffraction has been an active area of research for many years both in the frequency domain (i.e. the time harmonic case) and also in the time domain. Smooth surface diffraction as described here assumes that the surface is a perfect electric conductor. Even with this assumption, smooth surface diffraction is a very important phenomena since many geometries encountered in engineering contain conducting smooth surfaces, such as airplanes, automobiles, etc. The work in this report is based on the frequency domain UTD solution and Pathak provides an excellent summary of this work in [4].

There is an abundance of past research on the topic of diffraction from smooth surfaces which are excited by short pulses, either acoustic pulses or electromagnetic pulses. One of the classic works on acoustic pulse scattering is a book by Friedlander [7]. In chapter 6 of [7], Friedlander formulates the time domain acoustic Green's function (i.e. impulse response) for a circular cylinder and also for a sphere. He obtains an approximate "early time" formula for the diffraction from a circular cylinder by implementing an asymptotic evaluation of an inverse Laplace transform of the frequency domain result. This early time result is a summation of time domain creeping wave modes and therefore is not valid when the observer is near the surface shadow boundary (SSB), but it is still very useful for "deep shadow" observer locations or backscatter calculations. Friedlander solves the acoustic scattering from a sphere similarly. Also, he finds an explicit early time formula for when the observer is located at

the caustic in the shadow region. But, Friedlander does not obtain the solution to the sphere problem for the case when the diffracted ray field has passed through a caustic. In [42], Weston obtains the back-scattered electromagnetic field from a perfectly conducting sphere when the incident field is a plane wave and the temporal excitation is a modulated square pulse. Weston finds a power series approximation for small (or early) time from the inverse Laplace transform of the Luneberg-Kline expansion. For large (or late) time, Weston uses an eigenfunction representation and when the sphere radius is large in terms of the wavelength of the modulation frequency he used a creeping wave representation. Wait and Conda discussed diffraction of electromagnetic pulses by curved surfaces in [43]. The first section of Wait and Conda's paper is devoted to finding the electric currents induced on a circular cylinder when it is excited by a plane wave. The temporal excitation is a step function. The currents in the frequency domain are expressed as an approximate integral expression containing an Airy integral. This approximate frequency domain result is valid when the radius of the cylinder is large in terms of wavelength. They then expand this frequency domain expression into a power series and use an inverse Laplace transform to obtain an asymptotic time series in terms of inverse powers of time. Although it appears that they use both high frequency and low frequency approximations here, one can interpret their solution to be valid for intermediate time values and observations near the shadow boundary. In the second half of the paper, Wait and Conda [43] discuss the diffraction from a smooth surface when the source and observer are removed from the surface. They solve the specific case of a circular cylinder, although they mention at the end of the paper that these results could be easily generalized. This solution is valid for observations near the shadow boundary. In [44], Chen computes the large-time transient behavior of the diffracted field from a circular cylinder excited by a plane wave with a step function temporal behavior. He solves the problem for various types of boundary conditions at the surface and also pays close attention to causality. Chen bases his solution on the exact frequency domain eigenfunction summation. He uses an inverse Laplace transform on the eigenfunction summation, applies the transform term by term, and then evaluates each term asymptotically for

large time. Überall, Doolittle and McNicholas solve the acoustic scattering problem of a cylinder excited by an impulsive plane wave (i.e. the impulse response) [45]. They first solve the frequency domain problem and then obtain the impulse response by using an inverse Laplace transform. Since their frequency domain solution is an asymptotic high frequency result, their impulse response is valid for early (or small) times. Also, in their solution the scattered field is decomposed into a reflected field and diffracted field which is written as a sum of creeping wave modes. Therefore, their solution is not valid near the shadow boundary. In [46] and Appendix II of [1], Moffatt explores that nature of the creeping wave. He does this by examining the early time backscattered electromagnetic field from a circular cylinder and a sphere which he obtains by using an inverse Laplace transform on the asymptotic high frequency results. He discovers that the early time backscattered diffracted field from the sphere is the Hilbert transform of a causal time function and then correctly predicts that the early time approximate backscattered diffracted field from a sphere is not causal. This is easily understood now, since we know that the arrival of the reflected field represents the "turn on" time of the total scattered field, and therefore the "small time" solution for the diffracted field contribution may contain information before and after the time of arrival of the diffracted ray. This is consistent with the asymptotic nature of the "small time" solution. Wait investigates the currents on a cylinder when the cylinder is excited by an impulsive plane wave in [47]. Wait first formulates the solution in the frequency domain and approximates the currents in the penumbral (near the shadow boundary) region as a contour integral containing Airy functions. He expands this representation into a creeping wave mode series and uses an inverse Laplace transform term by term to obtain a time domain creeping wave mode series. He is able to transform each creeping wave mode (for the currents in the shadow region) in closed form in terms of Airy functions. In [48, 49], Schafer calculates the currents on a circular cylinder when the cylinder is excited by an impulsive plane wave. He finds an early (small) time representation in the lit region by using an inverse Laplace transform on the frequency domain Luneberg-Kline series which gives a power series time representation. He obtains an early (small) time representation

in the shadow region by applying the inverse Laplace transform to the high frequency creeping wave summation. He obtains a large time representation by applying the inverse Laplace transform to the frequency domain eigenfunction summation term by term. Finally, for intermediate time values he uses an interpolation scheme to combine the small and large time representations. Lee, Jamnejad and Mittra examine the early time response for the scattered field and current on a circular cylinder by using an inverse Laplace transform on the high frequency creeping wave representation [33]. In [50], Heyman and Felsen develop a solution for the currents on a circular cylinder (or a smooth surface in general) when the excitation is located on the cylinder. Their solution combines a low frequency eigenfunction representation with a high frequency creeping wave representation, then they do a similar combination in the time domain. Ma and Ciric in [51], obtain an early time solution for the currents on a circular cylinder when it is excited by a line current. Their solution is similar to Schafer's for the plane wave case. In [52], Naishadham and Yao present the transient scattering by a circular cylinder when it is excited by magnetic line source when the source and observation point are on the cylinder. They obtain their solution using an efficient numerical evaluation of a contour integral which approximates the exact contour integral solution.

The time domain curved surface diffraction presented in this chapter is different from the solutions discussed above since the present work is based on the frequency domain UTD [4]. The frequency domain UTD formulation of surface diffraction can be applied to a very general class of smooth surfaces, whereas most of the previous time domain solutions discussed above involve canonical geometries such as cylinders or spheres. More importantly, the previous time domain solutions discussed above assume simple excitations such as a plane wave or line source, whereas in the TD-UTD solution presented here, the excitation is an astigmatic ray field where plane, cylindrical and spherical wavefronts are special cases. Also, with the analytic time representation used here, one could easily incorporate incident ray fields which have passed through a smooth caustic, incident ray fields that are circularly polarized and

diffracted ray fields which have passed through a smooth caustic. This greatly increases the usefulness of the present TD-UTD solution for smooth surface diffraction.

The content of this chapter is as follows. First there is a brief review of the frequency domain UTD formulation for smooth surface diffraction. Then the TD-UTD is obtained for observers in the deep lit and deep shadow regions by applying the analytic time transform to the frequency domain UTD formulas. Also, a TD-UTD solution is obtained for observers near the shadow boundary. Finally, all of these solutions are combined to obtain a uniform TD-UTD surface diffraction solution which remains valid in the deep shadow region, near the shadow boundary and deep in the lit region. This uniform TD-UTD solution is the time domain version of the UTD solution in Pathak [4]. This solution is restricted to the "scattering case" where the observer and source are located off the smooth surface, although the radiation and coupling problems could be dealt with in a similar fashion. Finally, some simple numerical results are presented to demonstrate the TD-UTD and compare it with a reference solution.

4.1 General Formulation in the Frequency Domain

This chapter discusses only the smooth surface scattering situation where the source and observer are off of the surface. Although the radiation and coupling situations where the source or/and the observer are located on the smooth surface are of considerable interest only the scattering situation is considered here. The radiation and coupling situations could be analyzed in a similar fashion as the scattering problem studied here.

The frequency domain UTD solution for the smooth surface diffraction geometry shown in Figure 4.1 is as follows. The UTD formulation for smooth surface diffraction briefly presented here is based on the summary by Pathak [4]. For the scattering case

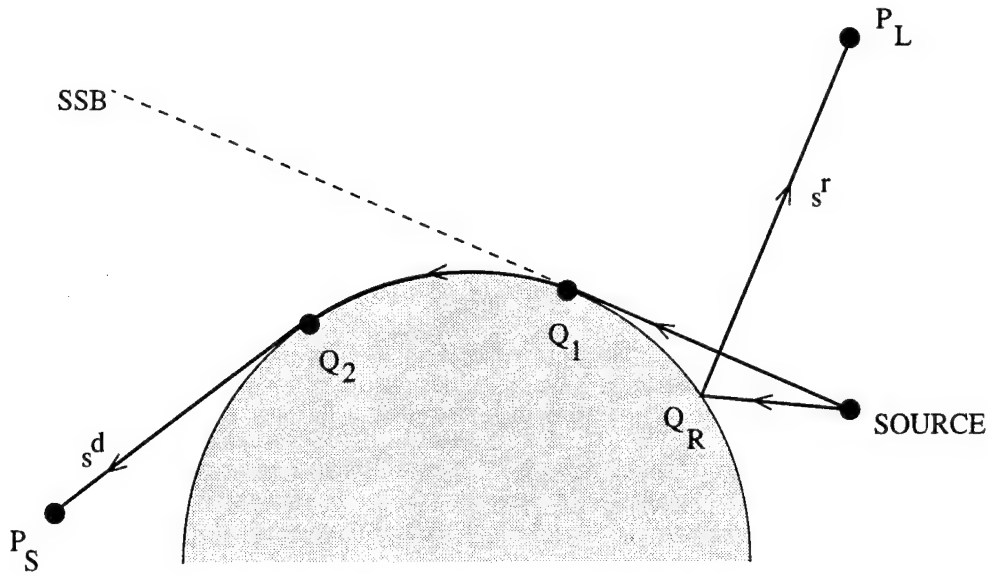


Figure 4.1: Geometry of the smooth surface scattering situation where the source and observer are off the surface.

shown in Figure 4.1, the total field as approximated by the UTD may be written as

$$\tilde{\mathbf{E}}^{\text{UTD}}(P) = \begin{cases} \tilde{\mathbf{E}}^i(P_L) + \tilde{\mathbf{E}}^{gr}(P_L) & P = P_L \text{ in lit region} \\ \tilde{\mathbf{E}}^d(P_S) & P = P_S \text{ in shadow} \end{cases} \quad (4.1)$$

The surface diffracted field $\tilde{\mathbf{E}}^d(P_S)$ may also appear in the lit region when the surface is closed and one includes multiple encirclements around the surface. The incident field $\tilde{\mathbf{E}}^i(P_L)$ is the usual GO incident field which exists in the lit region. The reflected field $\tilde{\mathbf{E}}^{gr}(P_L)$ is a generalized reflected field which behaves as the usual GO reflected field deep in the lit region, but behaves quite differently near the surface shadow boundary (SSB), it can be expressed in terms of generalized reflection coefficients

$$\tilde{\mathbf{E}}^{gr}(P_L) \sim \tilde{\mathbf{E}}^i(Q_R) \cdot [\tilde{\mathcal{R}}_s \hat{\mathbf{e}}_\perp \hat{\mathbf{e}}_\perp + \tilde{\mathcal{R}}_h \hat{\mathbf{e}}_\parallel \hat{\mathbf{e}}_\parallel] A_r(s^r) e^{-jks^r} \quad (4.2)$$

where $\tilde{\mathbf{E}}^i(Q_R)$ is the incident field at the point of reflection Q_R . The unit vectors in (4.2) are the same as in the usual GO reflection formula discussed in the previous chapter. The spreading factor for the reflected field is given by

$$A_r(s^r) = \sqrt{\frac{\rho_1^r \rho_2^r}{(\rho_1^r + s^r)(\rho_2^r + s^r)}} \quad (4.3)$$

where ρ_1^r and ρ_2^r are the reflected ray caustic distances and s^r is the distance from the reflection point Q_R to the observer at P . The surface diffracted field can be written

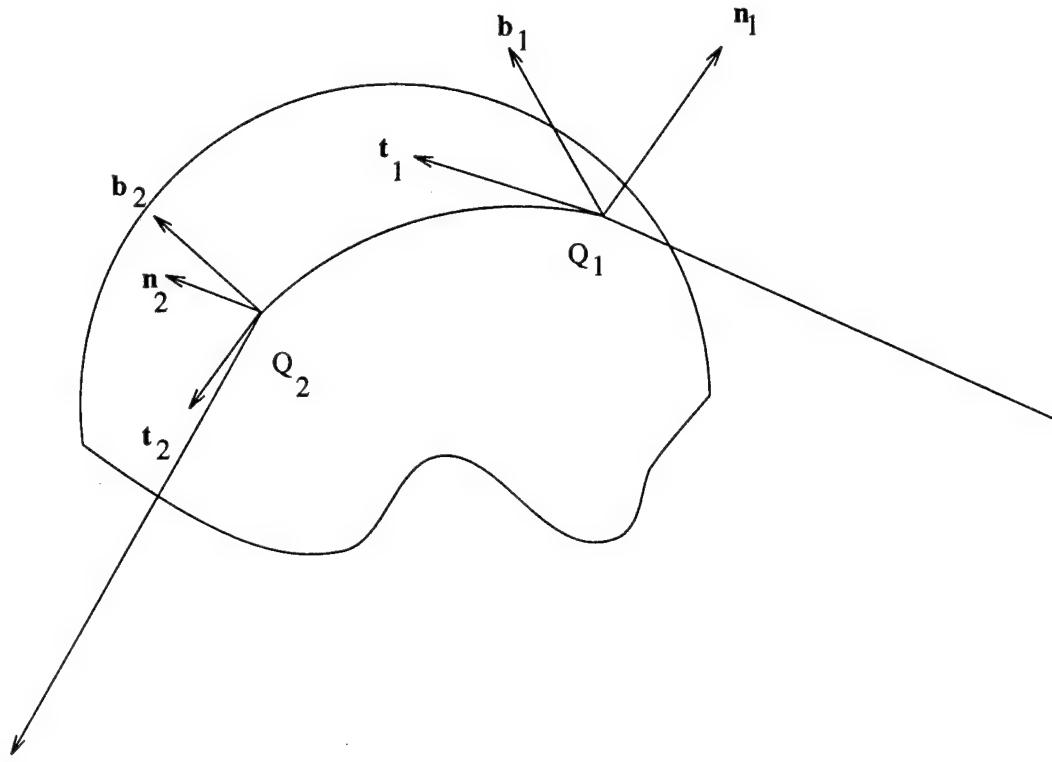


Figure 4.2: Ray vectors for surface diffraction.

as

$$\tilde{\mathbf{E}}^d(P_S) \sim \tilde{\mathbf{E}}^i(Q_1) \cdot [\tilde{\mathcal{D}}_s \hat{\mathbf{b}}_1 \hat{\mathbf{b}}_2 + \tilde{\mathcal{D}}_h \hat{\mathbf{n}}_1 \hat{\mathbf{n}}_2] A_d(s^d) e^{-jks^d} \quad (4.4)$$

where $\tilde{\mathbf{E}}^i(Q_1)$ is the incident field at the attachment point as shown in Figure 4.1. The unit ray vectors in (4.4) are shown in Figure 4.1. The unit vectors $\hat{\mathbf{n}}_1$ and $\hat{\mathbf{n}}_2$ are normal to the surface at points Q_1 and Q_2 respectively. The unit tangent vectors $\hat{\mathbf{t}}_1$ and $\hat{\mathbf{t}}_2$ point in the direction in which the "surface ray" is moving at points Q_1 and Q_2 respectively. The other tangent vectors $\hat{\mathbf{b}}_{1,2}$ are defined by $\hat{\mathbf{b}}_{1,2} = \hat{\mathbf{t}}_{1,2} \times \hat{\mathbf{n}}_{1,2}$. The spreading factor for the diffracted ray is

$$A_d(s^d) = \sqrt{\frac{\rho_s}{s^d(\rho_s + s^d)}} \quad (4.5)$$

where ρ_s is the caustic distance of the diffracted ray and s^d is the distance from the point of diffraction to the observer. The frequency domain generalized reflection coefficient can be written as

$$\tilde{\mathcal{R}}_{s,h} = -\sqrt{\frac{-4}{\Xi^L}} e^{-j\omega(\Xi^L)^3/12} \left\{ \frac{1}{2\Xi^L \sqrt{\pi} \sqrt{j\omega}} [1 - \tilde{F}_{tr}(\omega x^L)] + \frac{1}{\omega^{\frac{1}{6}}} \tilde{P}_{s,h}(\omega^{\frac{1}{3}} \Xi^L) \right\} \quad (4.6)$$

where

$$M(\cdot) = \left(\frac{\rho_g(\cdot)}{2c} \right)^{\frac{1}{3}} \quad (4.7)$$

$$\Xi^L = -2M(Q_R) \cos \theta^i \quad (4.8)$$

$$x^L = 2 \frac{L}{c} \cos^2 \theta^i \quad (4.9)$$

and θ^i is the angle between the surface normal vector and incident ray direction at the point of reflection. The function $\tilde{F}_{tr}(z)$ is the UTD transition function given in (3.33) and the Fock type function $\tilde{P}_{s,h}(z)$ is described shortly. The $\rho_g(Q_R)$ in the above equations is the radius of curvature of the surface at the point of reflection Q_R in the plane of incidence. The frequency domain UTD surface diffraction coefficient is given by

$$\begin{aligned} \tilde{\mathcal{D}}_{s,h} = & -\sqrt{2cM(Q_1)M(Q_2)} \left\{ \frac{1}{2\Xi\sqrt{\pi}\sqrt{j\omega}} [1 - \tilde{F}_{tr}(\omega x^d)] \right. \\ & \left. + \frac{1}{\omega^{\frac{1}{6}}} \tilde{P}_{s,h}(\omega^{\frac{1}{3}}\Xi) \right\} \sqrt{\frac{d\eta(Q_1)}{d\eta(Q_2)}} e^{-j\omega l/c} \end{aligned} \quad (4.10)$$

where

$$\Xi = \int_{Q_1}^{Q_2} \frac{M(l')}{\rho_g(l')} dl' \quad (4.11)$$

$$x^d = \frac{L\Xi^2}{2cM(Q_1)M(Q_2)} \quad (4.12)$$

$$l = \int_{Q_1}^{Q_2} dl' \quad (4.13)$$

The path from Q_1 to Q_2 on the surface is a geodesic where the path length is a minimum. The $\rho_g(l')$ in (4.11) is the radius of curvature of the surface at l' on the geodesic path in the \hat{l}' (or \hat{t}) direction. The distance parameter in (4.9) and (4.12) when evaluated at the shadow boundary is given by

$$L = \frac{\rho_1^i(Q_1)\rho_2^i(Q_1)}{(\rho_1^i(Q_1) + s)(\rho_2^i(Q_1) + s)} \frac{s(\rho_b^i(Q_1) + s)}{\rho_b^i(Q_1)} \quad (4.14)$$

where $\rho_{1,2}^i(Q_1)$ are the principle radii of curvature of the incident ray field at Q_1 and $\rho_b^i(Q_1)$ is the radius of curvature of the incident ray field in the \hat{b}_1 direction at Q_1 . Note that the distance parameter L in (4.9) and (4.12) would in general be different

for the lit and shadow regions but it is usually more convenient to approximate L by its value at the shadow boundary given by (4.14) [3].

For the special case of an incident spherical wave

$$L = \frac{s's}{s' + s} \quad (4.15)$$

and

$$s' = \rho_1^i(Q_1) = \rho_2^i(Q_1) = \rho_b^i(Q_1) \quad (4.16)$$

where s' is the distance from the source to the point Q_1 on the surface.

The Fock type functions $\tilde{P}_{s,h}(x)$ are related to the soft and hard Pekeris functions $p^*(x)$ and $q^*(x)$ by

$$\tilde{P}_{s,h}(x) = \begin{Bmatrix} \tilde{p}^*(x) \\ \tilde{q}^*(x) \end{Bmatrix} e^{-j\pi/4} - \frac{e^{-j\pi/4}}{2\sqrt{\pi x}} \quad (4.17)$$

where $\tilde{p}^*(x)$ and $\tilde{q}^*(x)$ are bounded and well behaved. The Fock type function $\tilde{P}_{s,h}(x)$ can also be written as

$$\tilde{P}_{s,h}(x) = \frac{e^{-j\pi/4}}{\sqrt{\pi}} \int_{-\infty}^{\infty} \frac{QV(z)}{QW_2(z)} e^{-jxz} dz \quad (4.18)$$

where the operator Q is

$$Q = \begin{cases} 1 & \text{soft case} \\ \partial/\partial z & \text{hard case} \end{cases} \quad (4.19)$$

The Fock type Airy functions are

$$2jV(z) = W_1(z) - W_2(z) \quad (4.20)$$

$$W_1(z) = \frac{1}{\sqrt{\pi}} \int_{\infty \exp(-j2\pi/3)}^{\infty} e^{zy - y^3/3} dy \quad (4.21)$$

$$W_2(z) = \frac{1}{\sqrt{\pi}} \int_{\infty \exp(+j2\pi/3)}^{\infty} e^{zy - y^3/3} dy \quad (4.22)$$

4.2 Deep Lit Region

The frequency domain UTD formulation for the fields in the lit region can be simplified when the observer is far from the shadow boundary. When the observer is in the deep

lit region (i.e. far from the shadow boundary), x^L is large and $-\Xi^L$ is large (or $\Xi^L \ll 0$) and the following approximations can be made

$$\tilde{F}_{tr}(\omega x^L) \sim 1 \quad \text{for } x^L \rightarrow \infty \quad (4.23)$$

$$\tilde{P}_{s,h}(\omega^{\frac{1}{3}} \Xi^L) \sim \pm \omega^{\frac{1}{6}} \sqrt{\frac{-\Xi^L}{4}} e^{j\omega(\Xi^L)^3/12} \quad \text{for } \Xi^L \rightarrow -\infty \quad (4.24)$$

Using the above approximations for the deep lit region, the generalized reflection coefficient becomes

$$\mathcal{R}_{s,h} \sim \mp 1 \quad \text{deep lit region} \quad (4.25)$$

where the \sim above the reflection coefficient $\tilde{\mathcal{R}}$ has been dropped since it is no longer a function of frequency with this approximation. It is now obvious that the generalized reflection coefficient $\tilde{\mathcal{R}}_{s,h}$ simply becomes the ordinary GO reflection coefficient $R_{s,h}$ discussed in Chapter 3 when the observer is in the deep lit region. Now the TD-UTD field in the deep lit region can be written as

$$\mathbf{E}^{gr}(P_L; t) \sim \mathbf{E}^i(Q_R; t - s^r/c) \cdot [\mathcal{R}_s \hat{\mathbf{e}}_{\perp} \hat{\mathbf{e}}_{\perp} + \mathcal{R}_h \hat{\mathbf{e}}_{\parallel} \hat{\mathbf{e}}_{\parallel}] A_r(s^r) \quad (4.26)$$

where $\mathcal{R}_{s,h}$ is given in (4.25). Notice that this is an early time deep lit region result which directly corresponds to the high frequency deep lit region approximations. The early time deep lit region result in (4.26) is not expected to be accurate for late times, since the deep lit region approximations made in the frequency domain are increasingly accurate as the frequency increases. Nonetheless, the result in (4.26) is a good approximation for early time and for an observer deep in the lit region.

4.3 Deep Shadow Region

The frequency domain UTD formulation can be simplified when the observer is deep in the shadow region. When the observer is in the deep shadow region, x^d in (4.12) and Ξ in (4.11) are large and positive and the following approximations can be made

$$\tilde{F}_{tr}(\omega x^d) \sim 1 \quad \text{for } x^d \rightarrow \infty \quad (4.27)$$

$$\tilde{P}_{s,h}(\omega^{\frac{1}{3}} \Xi) \sim \begin{cases} \frac{-e^{-j\pi/4}}{\sqrt{\pi}} \sum_{n=1}^N \frac{e^{j\frac{\pi}{6}} \exp(-(j\omega)^{\frac{1}{3}} \Xi q_n)}{2[\text{Ai}'(-q_n)]^2} \\ \frac{-e^{-j\pi/4}}{\sqrt{\pi}} \sum_{n=1}^N \frac{e^{j\frac{\pi}{6}} \exp(-(j\omega)^{\frac{1}{3}} \Xi \bar{q}_n)}{2\bar{q}_n[\text{Ai}(-\bar{q}_n)]^2} \end{cases} \quad (4.28)$$

for $\Xi \rightarrow \infty$. In (4.28), $\text{Ai}(x) = V(x)/\sqrt{\pi}$ is a Miller type Airy function and $\text{Ai}'(x) = \partial \text{Ai}(x)/\partial x$ is its derivative [29]. The n^{th} roots of $\text{Ai}(-q_n) = 0$ and $\text{Ai}'(-\bar{q}_n) = 0$, denoted by q_n and \bar{q}_n respectively, are also used in (4.28). Typically two terms ($N = 2$) are used for the summation in (4.28) [4]. The surface diffraction coefficient in (4.10) can now be simplified for an observer in the deep shadow region by

$$\tilde{D}_{s,h} \sim \sqrt{\frac{2c}{\pi}} M(Q_1) M(Q_2) \sqrt{\frac{d\eta(Q_1)}{d\eta(Q_2)}} e^{-j\omega l/c} \left\{ \begin{aligned} & \frac{1}{(j\omega)^{\frac{1}{6}}} \sum_{n=1}^N \frac{\exp(-(j\omega)^{\frac{1}{3}} \Xi q_n)}{2[\text{Ai}'(-q_n)]^2} \\ & \frac{1}{(j\omega)^{\frac{1}{6}}} \sum_{n=1}^N \frac{\exp(-(j\omega)^{\frac{1}{3}} \Xi \bar{q}_n)}{2\bar{q}_n[\text{Ai}(-\bar{q}_n)]^2} \end{aligned} \right\} \quad (4.29)$$

Finally, the analytic time transform can be applied to (4.29) to obtain the analytic time representations of the surface diffraction coefficient

$$\tilde{D}_{s,h}^+(t) \sim \sqrt{\frac{2c}{\pi}} M(Q_1) M(Q_2) \sqrt{\frac{d\eta(Q_1)}{d\eta(Q_2)}} \left\{ \begin{aligned} & \sum_{n=1}^N \frac{\tilde{F}_{cw}^+(\Xi q_n, \tau_D)}{2[\text{Ai}'(-q_n)]^2} \\ & \sum_{n=1}^N \frac{\tilde{F}_{cw}^+(\Xi \bar{q}_n, \tau_D)}{2\bar{q}_n[\text{Ai}(-\bar{q}_n)]^2} \end{aligned} \right\} \quad (4.30)$$

where $\tau_D = t - l/c$ and

$$\tilde{F}_{cw}^+(\alpha, t) = \frac{1}{\pi} \int_0^\infty (j\omega)^{-\frac{1}{6}} e^{-\alpha(j\omega)^{\frac{1}{3}}} e^{j\omega t} d\omega \quad (4.31)$$

for $\text{Im } t \geq 0$. The analytic time function in (4.31) is a new special function which must be calculated. Appendix D explains in detail how to calculate $\tilde{F}_{cw}^+(\alpha, t)$ in (4.31).

4.4 Observer Near the Shadow Boundary

This section presents the TD-UTD smooth surface reflection and diffraction coefficients for when the observer is near the shadow boundary. First rewrite the frequency domain generalized reflection coefficient in (4.6) as the following

$$\tilde{\mathcal{R}}_{s,h} = \sqrt{\frac{-4}{\Xi^L}} e^{-j\omega(\Xi^L)^3/12} \left\{ \frac{\tilde{F}_{tr}(\omega x^L)}{2\Xi^L \sqrt{\pi} \sqrt{j\omega}} - \frac{e^{-j\pi/6}}{(j\omega)^{1/6}} \left[\begin{aligned} & \tilde{p}^*(\omega^{1/3} \Xi^L) \\ & \tilde{q}^*(\omega^{1/3} \Xi^L) \end{aligned} \right] \right\} \quad (4.32)$$

and the surface diffraction coefficient of (4.10) as

$$\tilde{D}_{s,h} = -\sqrt{2cM(Q_1)M(Q_2)} \left[\frac{\tilde{F}_{tr}(\omega x^d)}{2\Xi \sqrt{\pi} \sqrt{j\omega}} \right]$$

$$-\frac{e^{-j\pi/6}}{(j\omega)^{1/6}} \left\{ \begin{array}{l} \tilde{p}^*(\omega^{1/3}\Xi) \\ \tilde{q}^*(\omega^{1/3}\Xi) \end{array} \right\} \left[\sqrt{\frac{d\eta(Q_1)}{d\eta(Q_2)}} e^{-j\omega l/c} \right] \quad (4.33)$$

Now apply the ATT to (4.32) and (4.33) to obtain

$$\mathcal{R}_{s,h}^+ = \sqrt{\frac{-4}{\Xi^L}} \left\{ \frac{\tilde{F}^+(cx^L, \tau_{\mathcal{R}})}{2\sqrt{\pi c \Xi^L}} - \tilde{F}_{p,q}^+(\Xi^L, \tau_{\mathcal{R}}) \right\} \quad (4.34)$$

where

$$\tau_{\mathcal{R}} = t - (\Xi^L)^3/12 \quad (4.35)$$

and

$$\mathcal{D}_{s,h}^+ = \sqrt{2cM(Q_1)M(Q_2)} \left[\frac{\tilde{F}^+(cx^d, \tau_{\mathcal{D}})}{2\sqrt{\pi c \Xi}} - \tilde{F}_{p,q}^+(\Xi, \tau_{\mathcal{D}}) \right] \sqrt{\frac{d\eta(Q_1)}{d\eta(Q_2)}} \quad (4.36)$$

where

$$\tau_{\mathcal{D}} = t - l/c \quad (4.37)$$

See Appendix E for a series expansion for $\tilde{F}_{p,q}^+(\Xi, t)$ which is appropriate when $|\Xi|$ is small (i.e. when the observer is close to the shadow boundary). The other time function used in (4.34) and (4.36) is related to the TD-UTD wedge transition function in (3.37) by

$$\mathcal{A} \left[\frac{\tilde{F}_{tr}(\omega x)}{\sqrt{j\omega}} \right] = \frac{1}{\sqrt{c}} \tilde{F}^+(cx, t) \quad (4.38)$$

$$= \frac{\sqrt{x/\pi}}{\sqrt{-jt}(\sqrt{-jt} + \sqrt{jx})} \quad (4.39)$$

At the shadow boundary, $x^d \rightarrow 0$ and $x^L \rightarrow 0$, therefore

$$\tilde{F}^+(cx, t) \sim \sqrt{\pi cx} \delta^+(t) \quad (4.40)$$

Also, $\Xi^L \rightarrow 0^-$ and $\Xi \rightarrow 0^+$ so that the following could be used

$$\tilde{F}_{p,q}^+(0, t) = \frac{\Gamma(5/6)}{j\pi} \frac{e^{-j\pi/12}}{(-jt)^{5/6}} \left\{ \begin{array}{l} p_0 \\ q_0 \end{array} \right\} \quad (4.41)$$

where $p_0 = 0.354064$ and $q_0 = -0.307177$. Equations (4.40) and (4.41) could be used to demonstrate that the TD-UTD is continuous across the surface shadow boundary,

just as is done in [3] for the frequency domain case. The term containing $\delta^+(t)$ function will produce minus one half of the incident field when used in the reflection coefficient and plus one half of the incident field when used in the diffraction coefficient. But, the term containing $(-jt)^{-5/6}$ produces a diffracted field effect even on the shadow boundary. This is in contrast to the first order diffraction from the wedge which becomes one half of the incident field at the shadow boundary.

4.5 Uniform TD-UTD Surface Diffraction

This section presents the uniform TD-UTD formulation for the scattering from a smooth convex surface. This requires the analytic time transform (ATT) of the corresponding frequency domain UTD generalized reflection coefficient in (4.6) and surface diffraction coefficient in (4.10). The following transform pairs are used

$$\mathcal{A} \left[\frac{1}{\sqrt{j\omega}} \right] = \frac{e^{-j\pi/4}}{\sqrt{\pi}\sqrt{-jt}} \quad (4.42)$$

and

$$\mathcal{A} \left[\frac{1}{\omega^{1/6}} \tilde{P}_{s,h}(\omega^{1/3}\Xi) \right] = \tilde{F}_{s,h}^{+P}(\Xi, t) \quad (4.43)$$

along with (4.38). The transform in (4.43) can be used when $\Xi < 0$ and when $\Xi > 0$, so it can be used for the generalized reflection coefficient and the surface diffraction coefficient. The special time function $\tilde{F}_{s,h}^{+P}(\Xi, t)$ is not known in closed form, but instead it can be calculated using various expansions for early time, late time and so forth. Appendix E fully explains the properties of the $\tilde{F}_{s,h}^{+P}(\Xi, t)$ function and explains the algorithm used for its calculation. Nonetheless, some basic results concerning the $\tilde{F}_{s,h}^{+P}(\Xi, t)$ are now summarized.

In the shadow region, $\Xi > 0$ and the following expansions can be used. When the observer is in the deep shadow region (or for very early time) a creeping wave expansion can be used

$$\tilde{F}_{s,h}^{+P}(\Xi, t) \sim \begin{cases} \frac{-1}{\sqrt{\pi}} \sum_{n=1}^N \frac{\tilde{F}_{cw}^{+}(\Xi q_n, t)}{2 [\text{Ai}'(-q_n)]^2} \\ \frac{-1}{\sqrt{\pi}} \sum_{n=1}^N \frac{\tilde{F}_{cw}^{+}(\Xi \bar{q}_n, t)}{2 \bar{q}_n [\text{Ai}(-\bar{q}_n)]^2} \end{cases} \quad (4.44)$$

for $|t/\Xi^3| \rightarrow 0$, where $\overset{+}{F}_{cw}(\alpha, t)$ are the time domain creeping wave mode functions described in Appendix D. When the observer is near the shadow boundary (or for late time) an inverse time power series can be used

$$\overset{+}{F}_{s,h}^P(\Xi, t) = \overset{+}{F}_{p,q}(\Xi, t) - \frac{1}{2\pi\Xi} \frac{e^{-j\pi/4}}{\sqrt{-jt}} \quad (4.45)$$

where

$$\overset{+}{F}_{p,q}(\Xi, t) = \frac{e^{-j\pi/12}}{\pi(-jt)^{5/6}} \sum_{n=0}^{\infty} \left\{ \begin{matrix} \rho_n \\ \sigma_n \end{matrix} \right\} \frac{\Gamma(n/3 + 5/6) e^{jn\pi/6}}{n!} \frac{\Xi^n}{(-jt)^{n/3}} \quad (4.46)$$

for $|t/\Xi^3| \neq 0$.

For the lit region, $\Xi^L < 0$, and (4.46) can be used when $|t/(\Xi^L)^3| \rightarrow \infty$ by simply replacing Ξ in (4.46) with Ξ^L . But, for $|t/(\Xi^L)^3| \rightarrow 0$ the creeping wave mode series in (4.44) is not valid in the lit region, instead one can use

$$\overset{+}{F}_{s,h}^P(\Xi, t) \sim \pm \sqrt{\frac{-\Xi^L}{4}} \overset{+}{\delta}(t + (\Xi^L)^3/12) \quad (4.47)$$

for $|[t + (\Xi^L)^3/12]/(\Xi^L)^3| \rightarrow 0$. See Appendix E for more details about the computation of these expansions and $\overset{+}{F}_{s,h}^P(\Xi, t)$ in general.

Now, using the transform relationships in (4.38), (4.42) and (4.43), transform (4.6) into

$$\overset{+}{\mathcal{R}}_{s,h} = -\sqrt{\frac{-4}{\Xi^L}} \left\{ \frac{e^{-j\pi/4}}{2\Xi^L\pi(\sqrt{-jt} + \sqrt{jx^L})} + \overset{+}{F}_{s,h}^P(\Xi^L, \tau_{\mathcal{R}}) \right\} \quad (4.48)$$

and transform (4.10) into

$$\overset{+}{\mathcal{D}}_{s,h} = -\sqrt{2cM(Q_1)M(Q_2)} \left\{ \frac{e^{-j\pi/4}}{2\Xi\pi(\sqrt{-jt} + \sqrt{jx^d})} + \overset{+}{F}_{s,h}^P(\Xi, \tau_{\mathcal{D}}) \right\} \quad (4.49)$$

It is interesting to notice how

$$\frac{e^{-j\pi/4}}{\sqrt{-jt} + \sqrt{jx}}$$

behaves for $x > 0$ and real time $\text{Im}(t) = 0$. The above can be rewritten as

$$\frac{\sqrt{t} - j\sqrt{x}}{t + x}$$

and notice that this gives

$$\operatorname{Re} \left(\frac{e^{j\pi/4}}{\sqrt{-jt} + \sqrt{jx}} \right) = \frac{\sqrt{t}u(t)}{t+x}$$

for $x > 0$ and $\operatorname{Im}(t) = 0$. This is the same type of transient behavior observed for the slope diffraction transition function (C.17).

4.6 Numerical Example

Figures 4.4 through 4.8 show a comparison between a TD-UTD solution and an eigenfunction reference solution for the TE_z (soft) far zone scattering from a two dimensional (2-D) cylinder at various bistatic angles. The reference eigenfunction solution is a frequency domain solution [53] which is multiplied by the frequency domain window in Figure 4.3 and transformed into the time domain using the IFFT. The time pulse excitation, in the top plot of Figure 4.3, corresponding to the frequency window in the bottom plot of Figure 4.3, is convolved with the TD-UTD analytic impulse response in closed form where only two frequency domain exponentials are used (see (2.67) in Chapter 2). In the far zone, $x^d \rightarrow \infty$ and $x^L \rightarrow \infty$ so that the coefficients $\mathcal{R}_{s,h}^+$ and $\mathcal{D}_{s,h}^+$ are proportional to the $F_{s,h}^{+P}(\Xi, t)$ function. The source and observer locations are chosen to be in the far zone for this comparison because the $F_{s,h}^{+P}(\Xi, t)$ function is more difficult to calculate than the other terms in reflection coefficient $\mathcal{R}_{s,h}^+$ and diffraction coefficient $\mathcal{D}_{s,h}^+$ and it is therefore desirable to check the accuracy of this $F_{s,h}^{+P}(\Xi, t)$ function. The radius of the cylinder is $r = 1$ meter which makes the radius one wavelength at the peak frequency of the window function in Figure 4.3. In Figures 4.4 through 4.13, the top plot shows the magnitude of the analytic time function while the bottom plot shows the real part of the analytic time function. Although the bottom plots (i.e. the real part) are the actual time signals arising from the excitation in Figure 4.3, the top plots (i.e. the magnitude) may be thought of qualitatively as the signal from an envelope detector. Notice that there is excellent agreement between the TD-UTD solution and the eigenfunction reference solution, which confirms that the numerical algorithm for computing $F_{s,h}^{+P}(\Xi, t)$ in

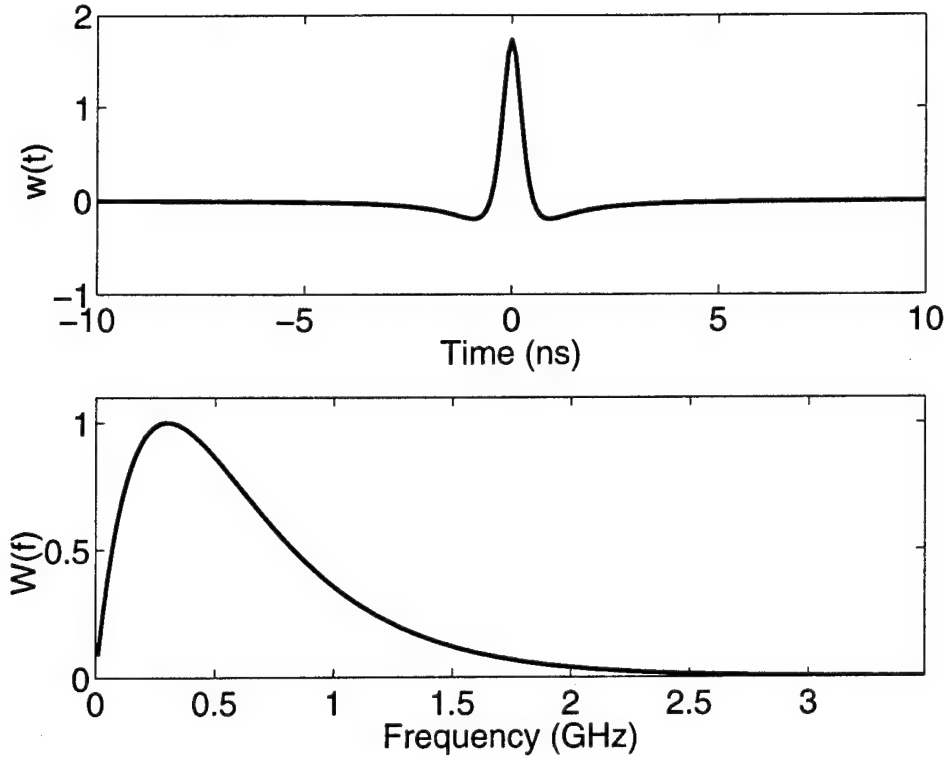


Figure 4.3: Excitation pulse $w(t)$ and corresponding frequency response (or frequency window) $W(f)$ used for the scattering from a 2-D cylinder example.

Appendix E is working well for this case and that the TD-UTD is very accurate for this case.

Figures 4.9 through 4.13 are essentially the same as the Figures 4.4 through 4.8 just discussed except that Figures 4.9 through 4.13 are for the TM_z (hard) polarization case.

4.7 Conclusions

This chapter presents a TD-UTD formulation for the scattering from a smooth perfectly conducting convex surface. The TD-UTD impulse response for the field in the presence of a convex smooth surface may be written as

$$\mathbf{E}_I^{\text{UTD}}(t) = \begin{cases} \mathbf{E}_I^i(t) + \mathbf{E}_I^{gr}(t) & \text{lit region} \\ \mathbf{E}_I^d(t) & \text{shadow region} \end{cases} \quad (4.50)$$

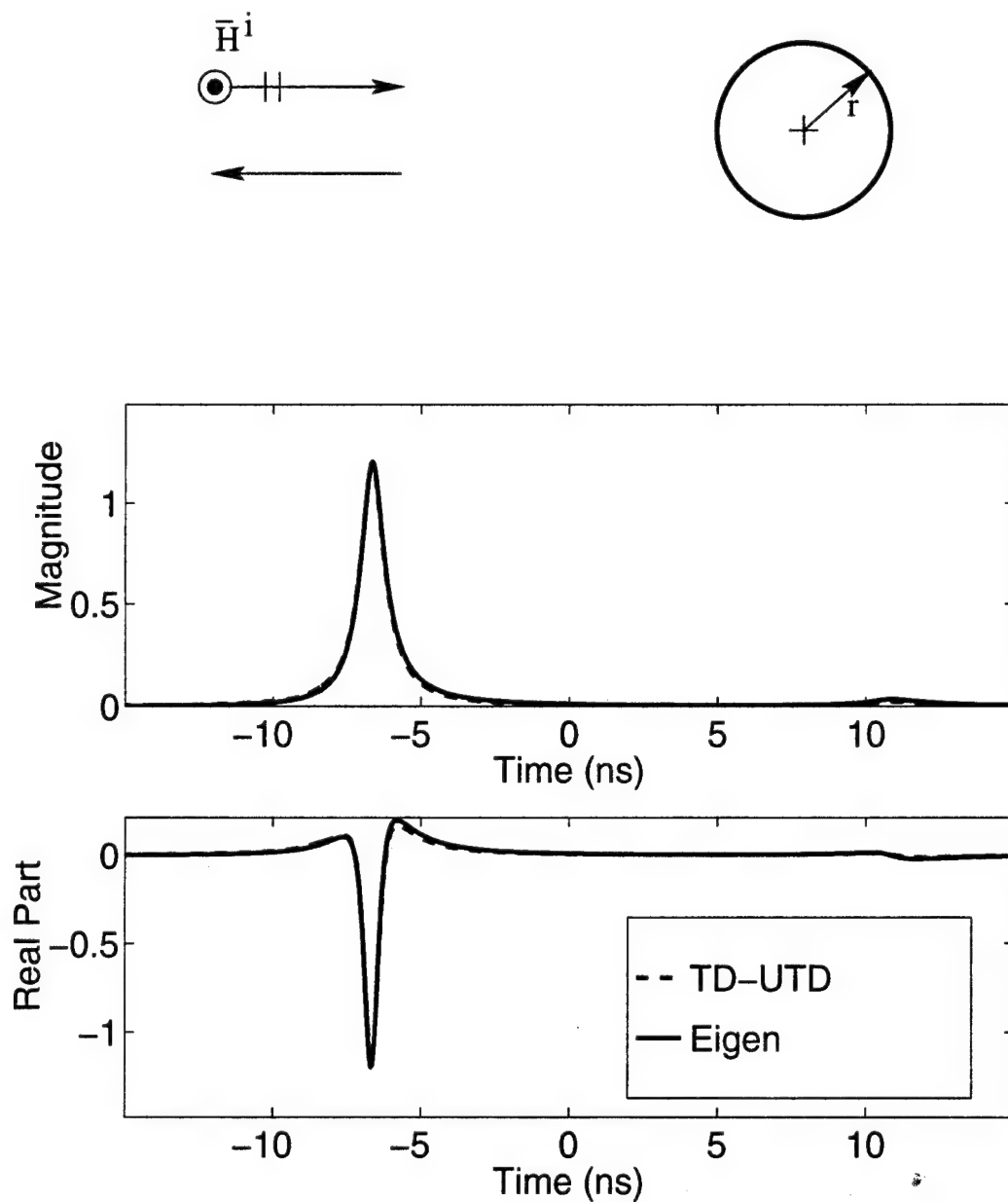


Figure 4.4: Comparison of the TD-UTD solution and an eigenfunction reference solution (eigen) which is transformed into time domain with the IFFT after the window in Figure 4.3 is applied. The far zone backscatter from a 2-D circular cylinder, for TE_z (hard) polarization and the radius is $r = 1$ meter.

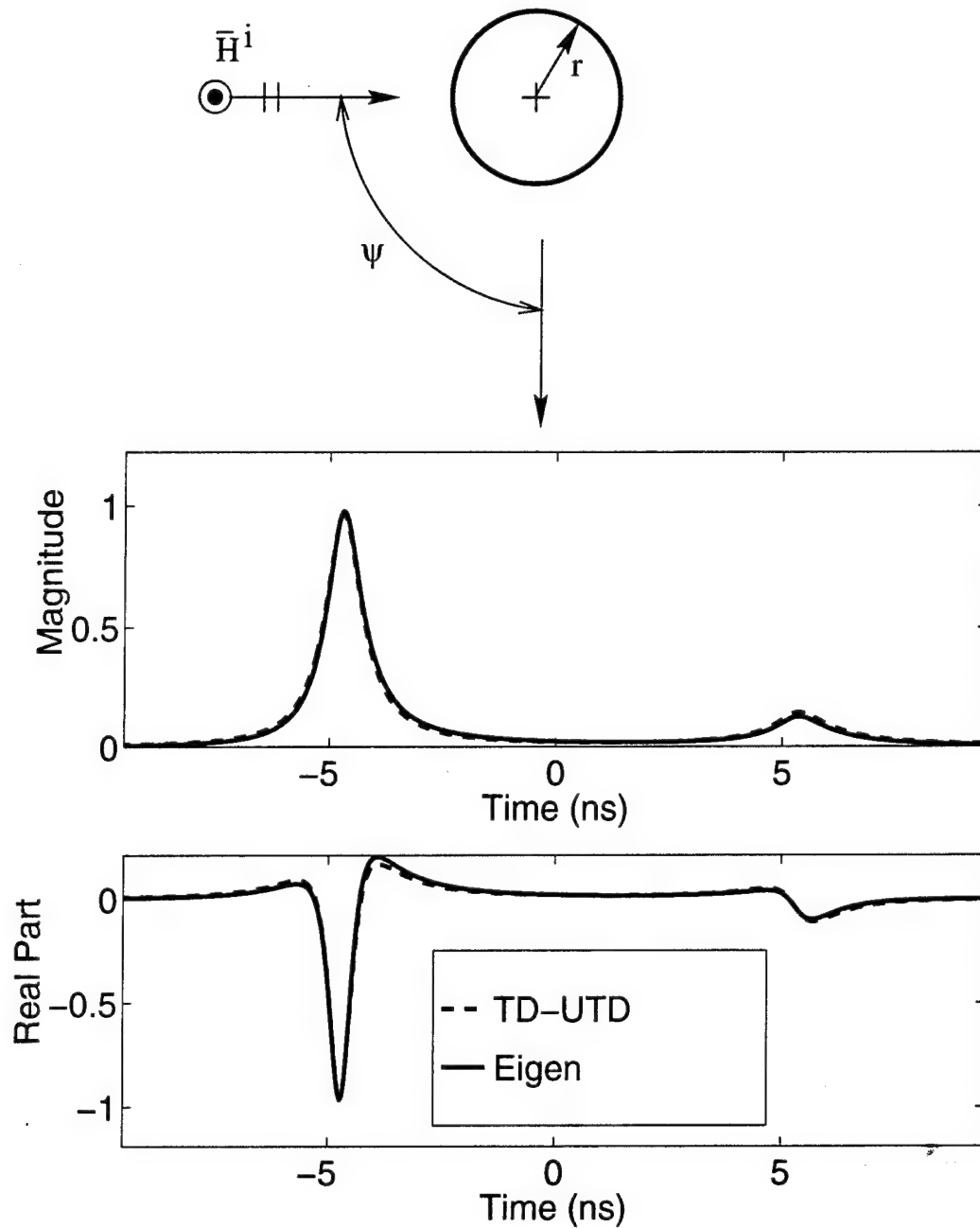


Figure 4.5: Comparison of the TD-UTD versus a reference eigenfunction solution ("eigen") which is transformed into the time domain with the IFFT after the window in Figure 4.3 is applied. The far zone bistatic scattering (at bistatic angle $\psi = 90^\circ$) from 2-D cylinder, for TE_z (hard) polarization and radius $r = 1$ meter.

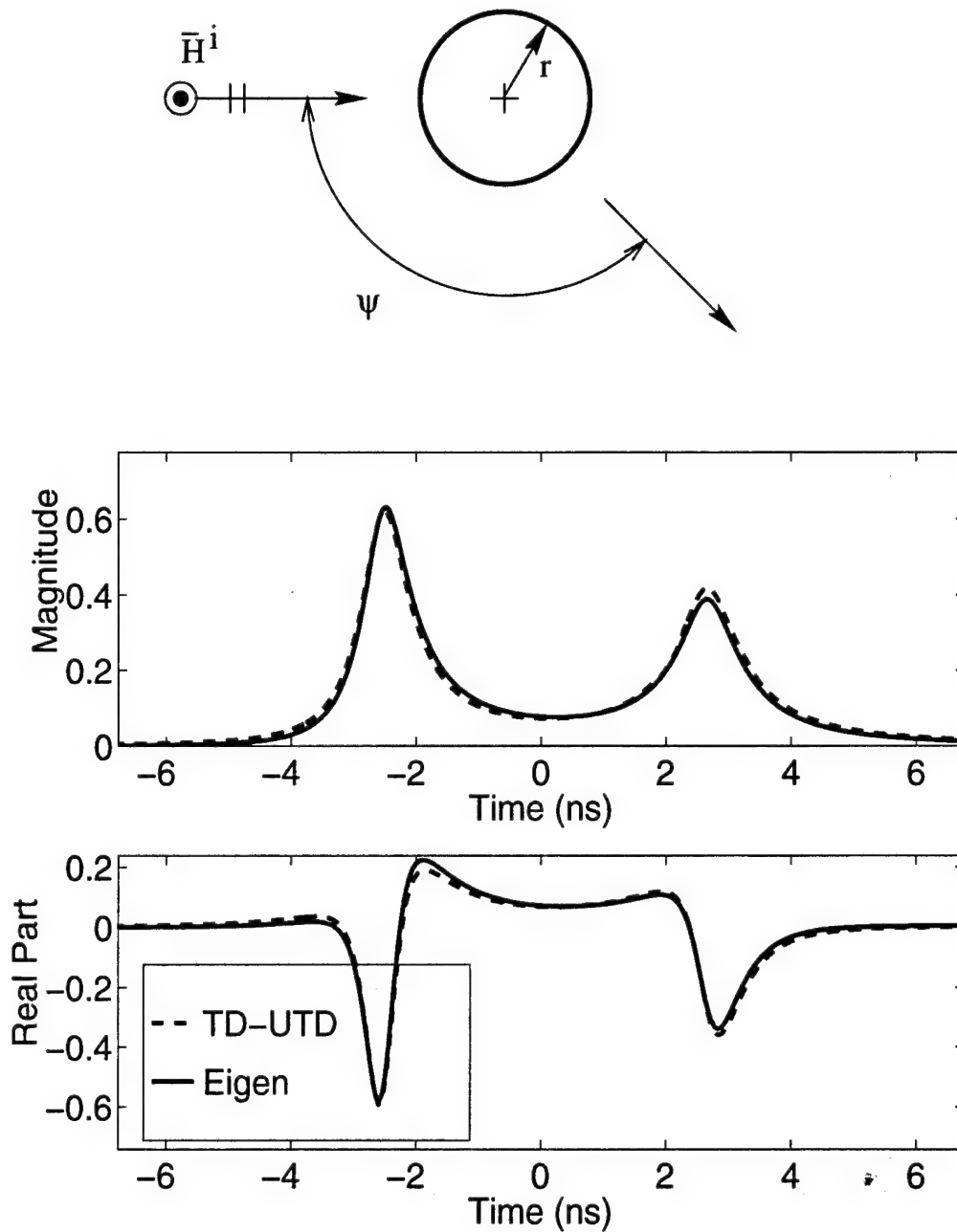


Figure 4.6: Comparison of the TD-UTD versus a reference eigenfunction solution ("eigen") which is transformed into the time domain with the IFFT after the window in Figure 4.3 is applied. The far zone bistatic scattering (at bistatic angle $\psi = 135^\circ$) from 2-D cylinder, for TE_z (hard) polarization and radius $r = 1$ meter.

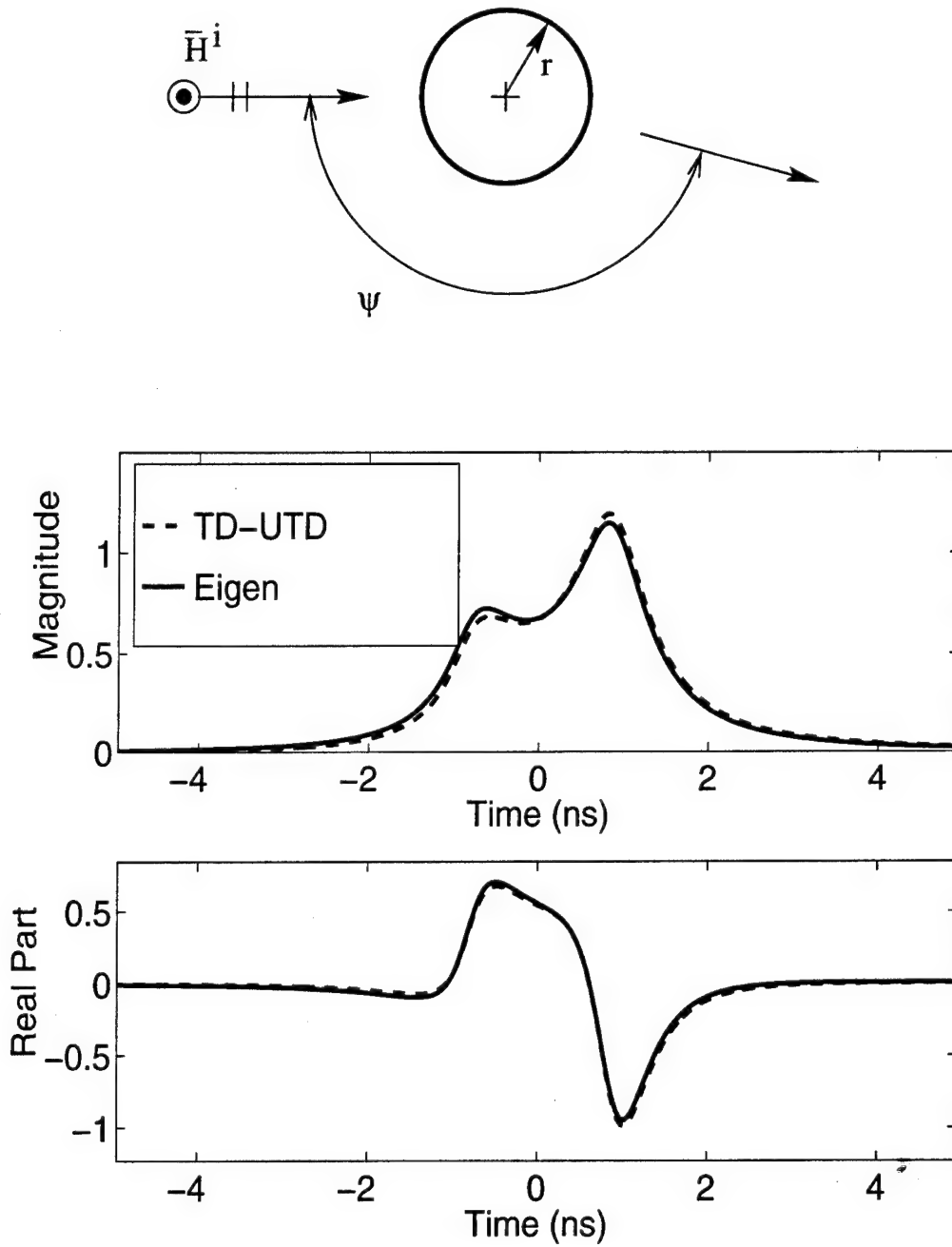


Figure 4.7: Comparison of the TD-UTD versus a reference eigenfunction solution (“eigen”) which is transformed into the time domain with the IFFT after the window in Figure 4.3 is applied. The far zone bistatic scattering (at bistatic angle $\psi = 165^\circ$) from 2-D cylinder, for TE_z (hard) polarization and radius $r = 1$ meter.

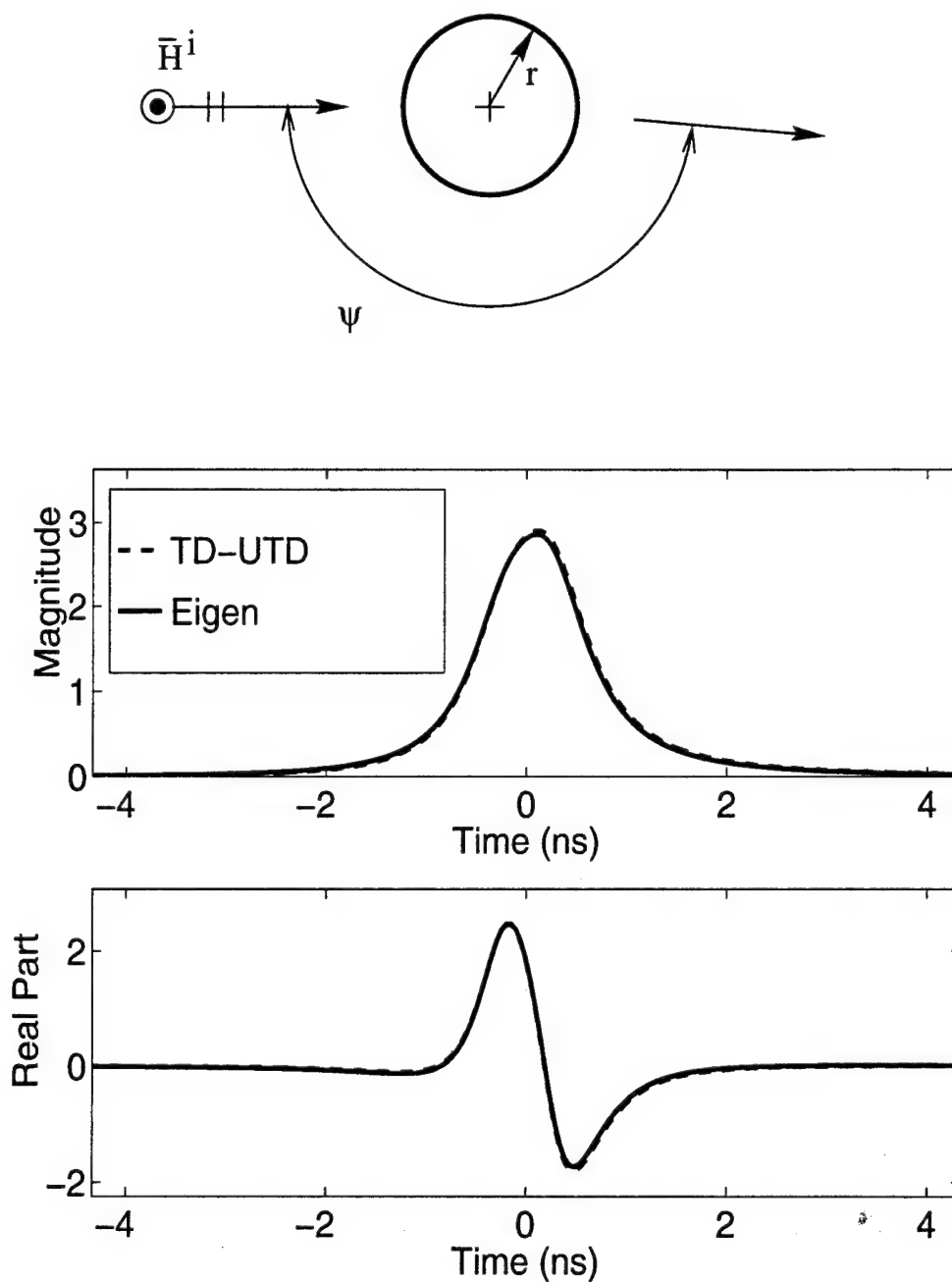


Figure 4.8: Comparison of the TD-UTD versus a reference eigenfunction solution ("eigen") which is transformed into the time domain with the IFFT after the window in Figure 4.3 is applied. The far zone bistatic scattering (at bistatic angle $\psi = 175^\circ$) from 2-D cylinder, for TE_z (hard) polarization and radius $r = 1$ meter.

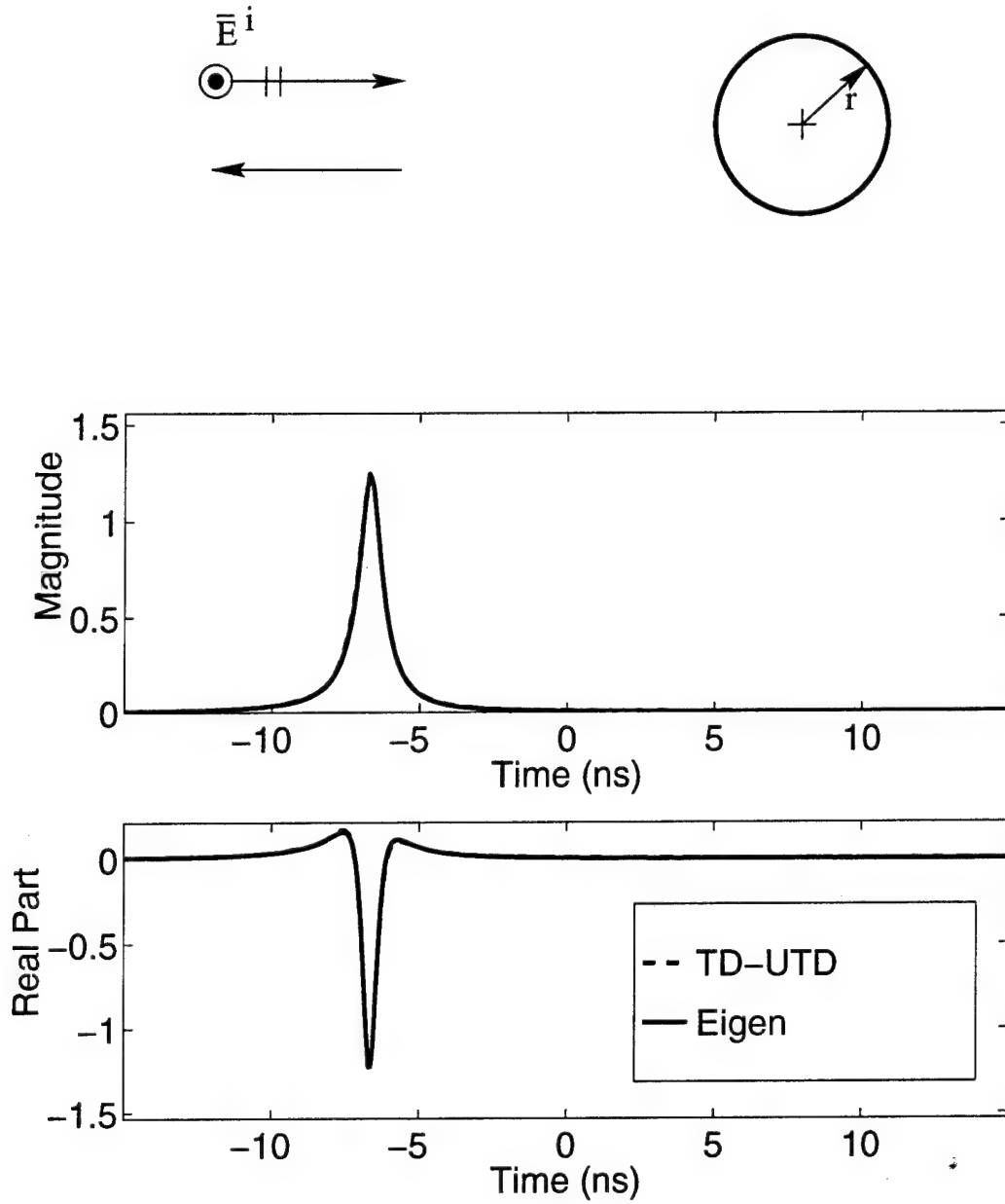


Figure 4.9: Comparison of the TD-UTD versus a reference eigenfunction solution (“eigen”) which is transformed into the time domain with the IFFT after the window in Figure 4.3 is applied. The far zone backscatter from 2-D cylinder, for TM_z (soft) polarization and radius $r = 1$ meter.

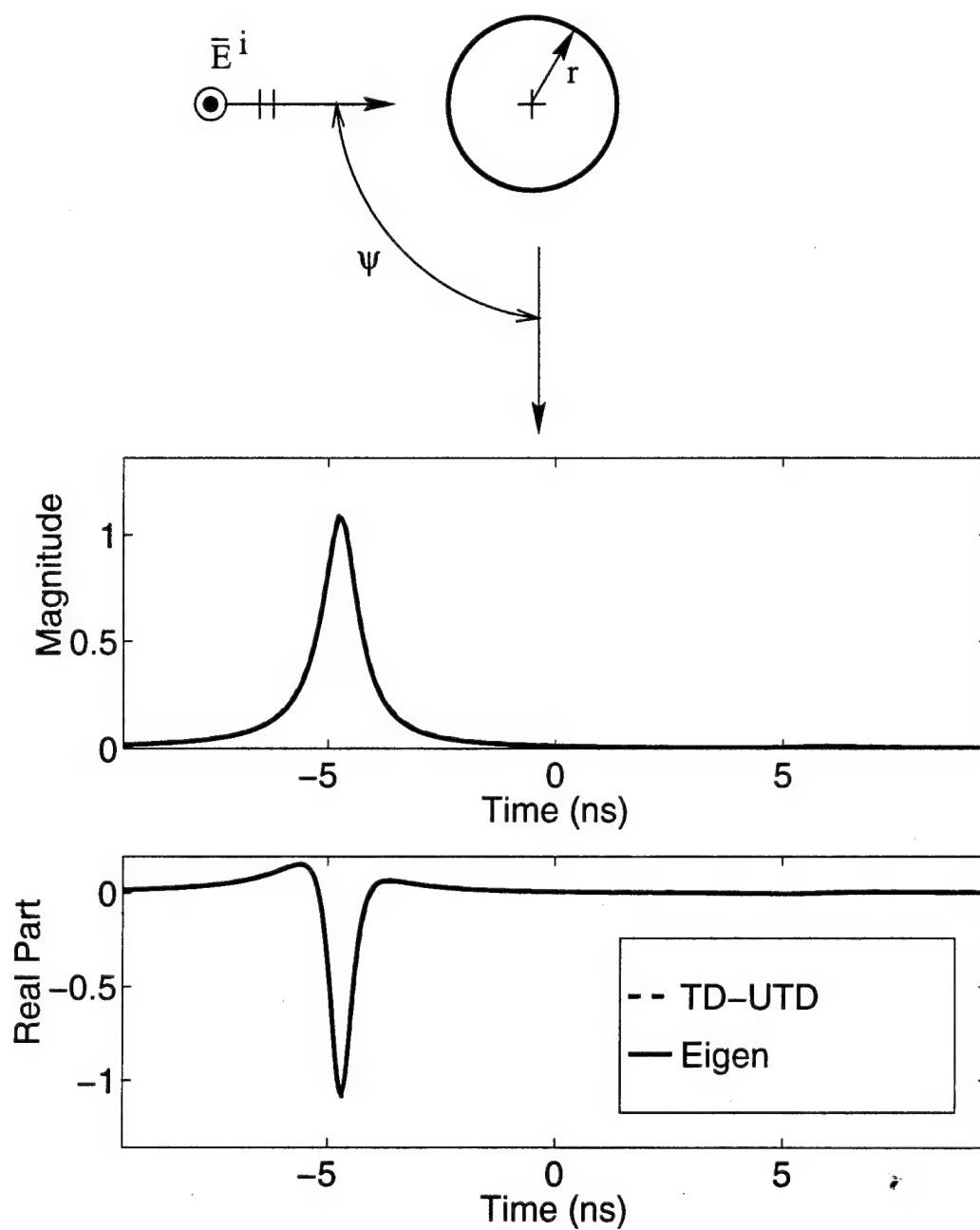


Figure 4.10: Comparison of the TD-UTD versus a reference eigenfunction solution ("eigen") which is transformed into the time domain with the IFFT after the window in Figure 4.3 is applied. The far zone bistatic scattering (bistatic angle $\psi = 90^\circ$) from 2-D cylinder, for TM_z (soft) polarization and radius $r = 1$ meter.

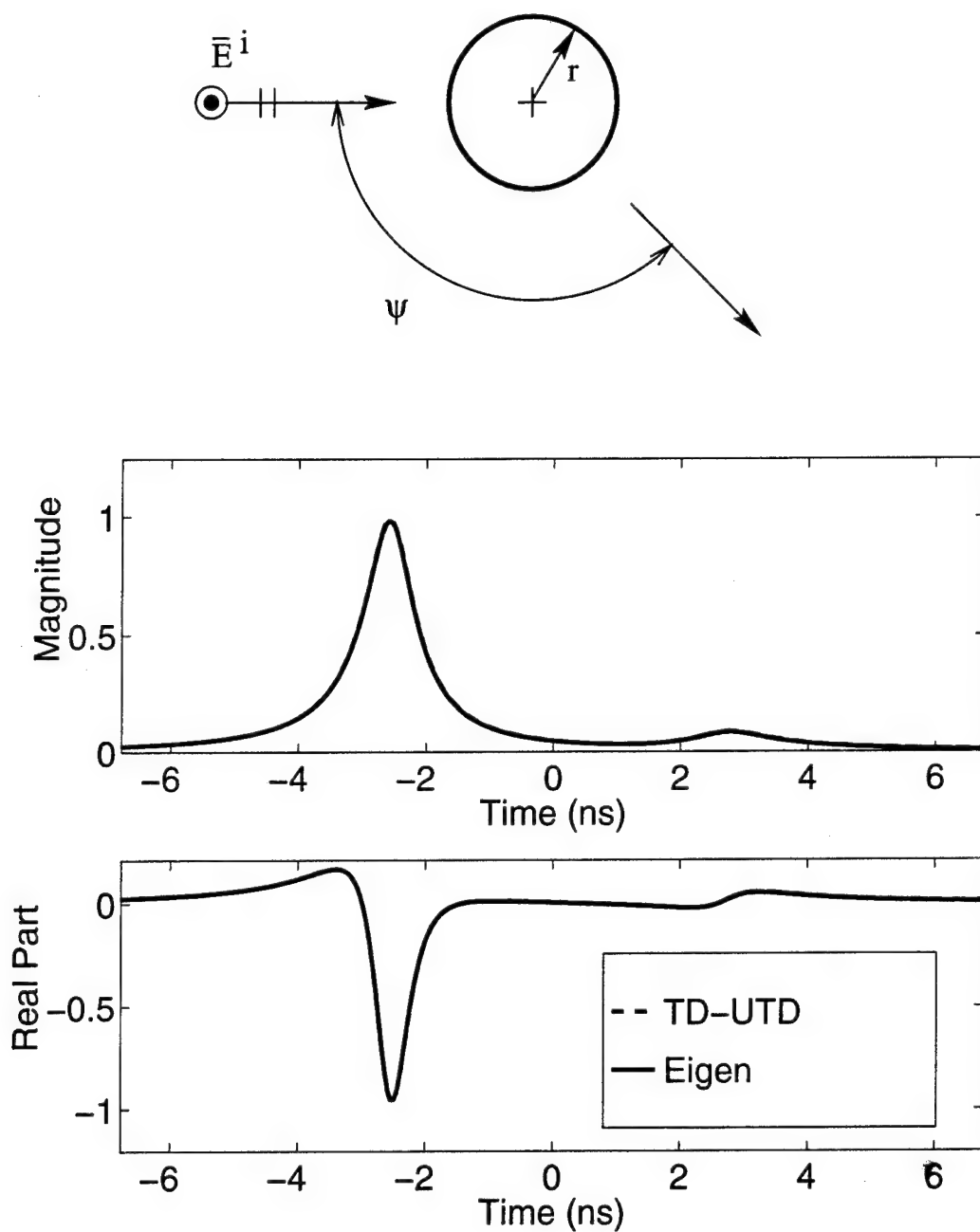


Figure 4.11: Comparison of the TD-UTD versus a reference eigenfunction solution (“eigen”) which is transformed into the time domain with the IFFT after the window in Figure 4.3 is applied. The far zone bistatic scattering (bistatic angle $\psi = 135^\circ$) from 2-D cylinder, for TM_z (soft) polarization and radius $r = 1$ meter.

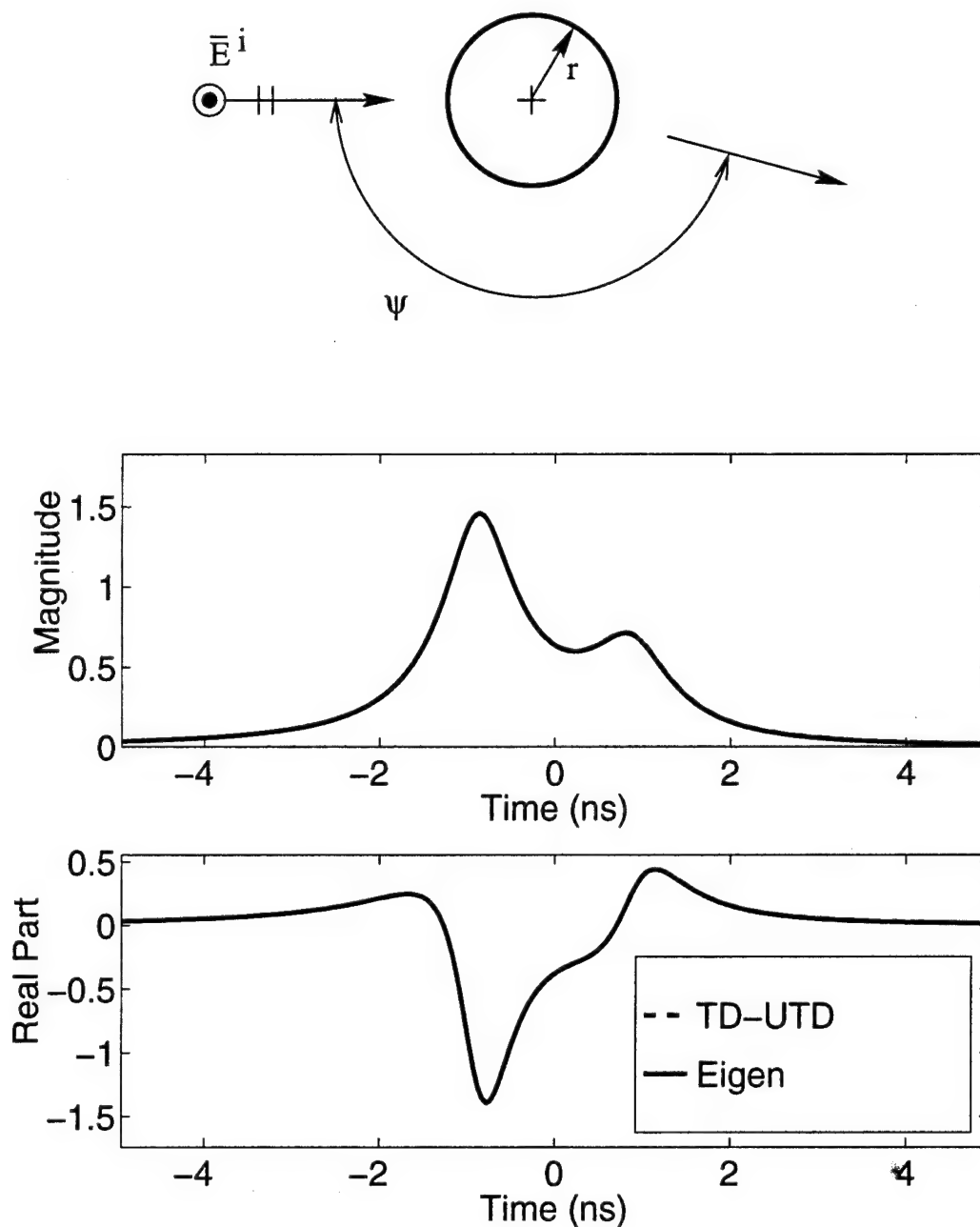


Figure 4.12: Comparison of the TD-UTD versus a reference eigenfunction solution ("eigen") which is transformed into the time domain with the IFFT after the window in Figure 4.3 is applied. The far zone bistatic scattering (bistatic angle $\psi = 165^\circ$) from 2-D cylinder, for TM_z (soft) polarization and radius $r = 1$ meter.

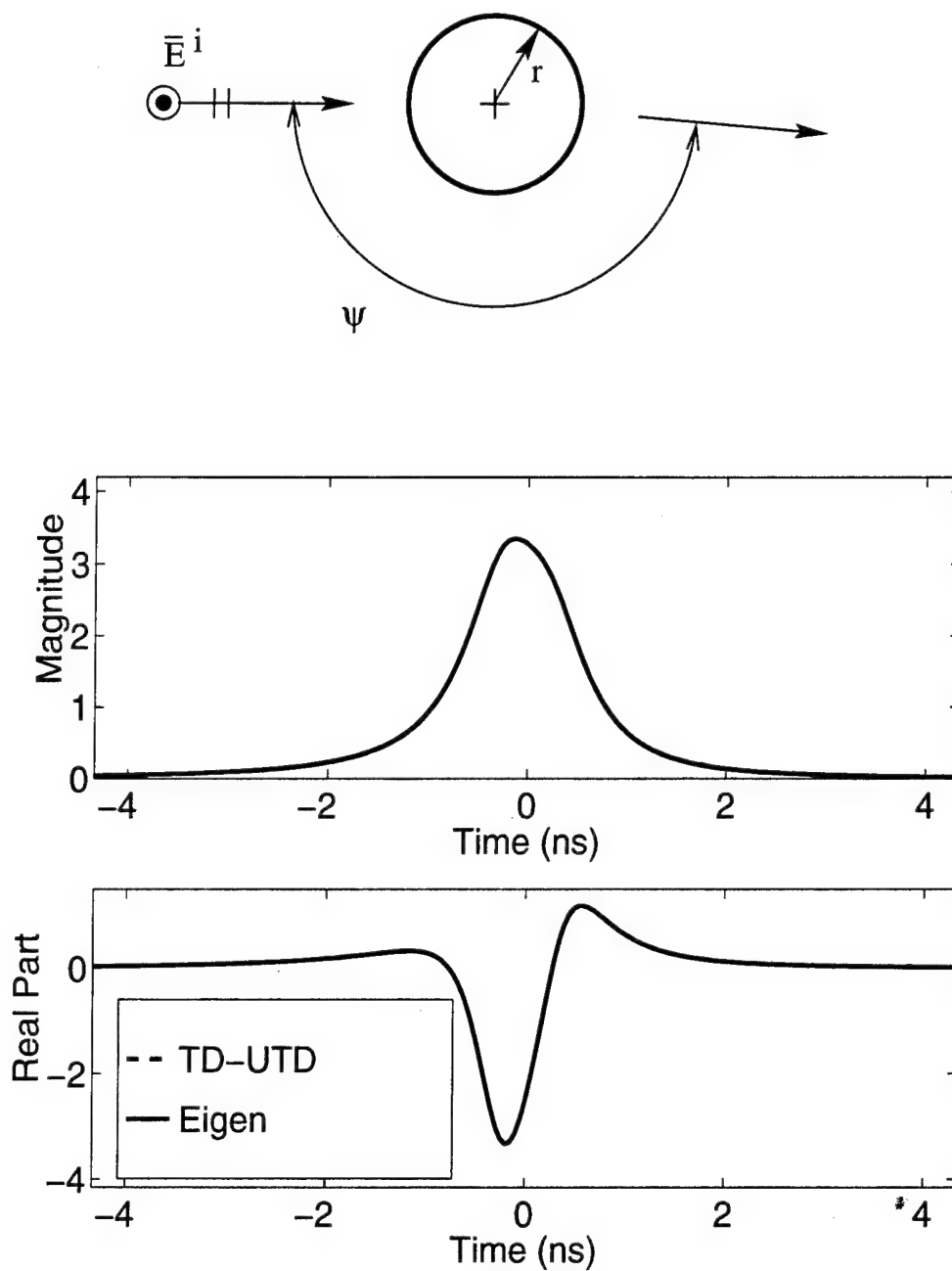


Figure 4.13: Comparison of the TD-UTD versus a reference eigenfunction solution (“eigen”) which is transformed into the time domain with the IFFT after the window in Figure 4.3 is applied. The far zone bistatic scattering (bistatic angle $\psi = 175^\circ$) from 2-D cylinder, for TM_z (soft) polarization and radius $r = 1$ meter.

where the impulse response of the incident GO field is

$$\mathbf{E}_I^+(t) = \mathbf{E}_0^i A_i(s^i) \delta(t - s^i/c) \quad (4.51)$$

with \mathbf{E}_0^i being an initial value vector which is a constant with respect to time (or frequency) and contains the polarization information of the incident field. Note that the field in (4.51) is from the source and travels to the observer along a straight line of length s^i . The fields incident at the point of reflection Q_R and the attachment point Q_1 have the same form as in (4.51). The TD-UTD generalized reflected field is

$$\mathbf{E}_I^{gr}(t) = \mathbf{E}_0^i \cdot [\mathcal{R}_s^+(\tau_r) \hat{\mathbf{e}}_\perp \hat{\mathbf{e}}_\perp + \mathcal{R}_h^+(\tau_r) \hat{\mathbf{e}}_\parallel \hat{\mathbf{e}}_\parallel] A_r(s^r) A_i(s^i) \quad (4.52)$$

where $\tau_r = t - s^i/c - s^r/c$, and the TD-UTD surface diffracted field is

$$\mathbf{E}_I^d(t) = \mathbf{E}_0^i \cdot [\mathcal{D}_s^+(\tau_d) \hat{\mathbf{b}}_1 \hat{\mathbf{b}}_2 + \mathcal{D}_h^+(\tau_d) \hat{\mathbf{n}}_1 \hat{\mathbf{n}}_2] A_d(s^d) A_i(s^i) \quad (4.53)$$

where $\tau_d = t - s^i/c - s^d/c$. Note that the variable s^i in (4.52) is the distance from the source to the reflection point Q_R but the variable s^i in (4.53) is the distance from the source to the point of attachment Q_1 . The TD-UTD coefficients $\mathcal{R}_{s,h}$ and $\mathcal{D}_{s,h}$ can be found in (4.48) and (4.49), respectively. The special function $\bar{F}_{s,h}^{+P}(\Xi, t)$, used in the uniform coefficients $\mathcal{R}_{s,h}$ and $\mathcal{D}_{s,h}$, can be calculated using the numerical algorithm in Appendix E for all values of Ξ and $\text{Im}(t) > 0.002|\Xi^3|$ (or $\text{Im}(t) > 0.002|(\Xi^L)^3|$). Finally, the impulse response formulas, denoted by the subscript I , may be convolved with an excitation in closed form as in (3.80) and (3.81) when the excitation has the form in (3.77) and (3.78).

Chapter 5

Conclusions

This report presents a development of a time domain version of the uniform geometrical theory of diffraction (TD-UTD). The analytic time transform (ATT) is formulated and is shown to be very useful in deriving the TD-UTD solution to the scattering from an arbitrary curved wedge and also from an arbitrary smooth convex surface, both of which configurations are perfectly conducting. These two types of configurations constitute a very important set because many complex geometries can be built up from these configurations as has already been demonstrated in the frequency domain UTD based ray approach. This same ray picture is valid in the TD-UTD developed here, and therefore the TD-UTD retains all the advantages of the frequency domain UTD.

The ATT is defined and its properties are discussed in Chapter 2. An important observation is that the ATT may be expressed as a one-sided forward Laplace transform when the roles of time and frequency are interchanged as expressed in (2.13). This is an important observation since it implies that the abundant math texts and tables on the one-sided Laplace transform may be applied in deriving results for the ATT. Another important result presented in Chapter 2 is the ATT applied to an asymptotic high frequency power series expansion, which is useful when deriving expressions for the numerical computation of special functions. It is noted that the ATT can not simply be applied to an asymptotic frequency domain power series term-by-term, nonetheless more rigorous results are presented in Chapter 2. When an impulse response is represented by an analytic time function (obtained by the

ATT), the convolution with an excitation pulse function can be performed in closed form as in (2.70) when the frequency response of the excitation is modeled as a series of exponential functions as in (2.67).

The TD-UTD formulation for the scattered field from a general curved wedge when the wedge is illuminated by an astigmatic wavefront is presented in Chapter 3. The TD-UTD impulse response for the curved wedge is obtained by an application of the ATT to the frequency domain UTD formulation. This TD-UTD impulse response may then be convolved with a more general time pulse excitation where the convolution may be performed efficiently as described in Chapter 2. In general, the TD-UTD impulse response for the curved wedge may be expressed as

$$\mathbf{E}_I^{+ \text{UTD}}(t) = \mathbf{E}_I^{+i}(t)U_i + \mathbf{E}_I^{+r}(t)U_r + \mathbf{E}_I^{+d}(t) + \mathbf{E}_I^{+sd}(t) \quad (5.1)$$

where the spatial unit step functions U_i and U_r are 1 on the lit side of the incident shadow boundary and the reflection shadow boundary, respectively, and 0 otherwise. The TD-UTD incident GO field $\mathbf{E}_I^{+i}(t)$ is in (3.10) and the TD-UTD reflected field $\mathbf{E}_I^{+r}(t)$ is in (3.14). The first order TD-UTD edge diffracted field $\mathbf{E}_I^{+d}(t)$ is in (3.16) where the TD-UTD dyadic diffraction coefficient is defined in (3.40) and (3.41). The higher order edge diffracted field called the slope diffracted field $\mathbf{E}_I^{+sd}(t)$ is in (3.56) where the TD-UTD dyadic slope diffraction coefficient based on Hwang's frequency domain UTD slope result is given in (3.57) and (3.58) while the slope diffraction coefficient based on Veruttipong's frequency domain UTD result is given in (3.64) and (3.65). The two versions of the slope diffraction coefficient are derived in detail in Appendix C.

Chapter 4 presents a TD-UTD formulation for the scattering from smooth conducting convex surfaces. Only the scattering case where the source and observer are removed from the surface is analyzed in Chapter 4, but the radiation and coupling cases could be handled in a similar fashion. The TD-UTD impulse response for the

field in the presence of a convex smooth surface may be written as

$$\mathbf{E}_I^{\text{UTD}}(t) = \begin{cases} \mathbf{E}_I^i(t) + \mathbf{E}_I^{gr}(t) & \text{lit region} \\ \mathbf{E}_I^d(t) & \text{shadow region} \end{cases} \quad (5.2)$$

where the impulse response of the incident GO field is

$$\mathbf{E}_I^i(t) = \mathbf{E}_0^i A_i(s^i) \delta(t - s^i/c) \quad (5.3)$$

with \mathbf{E}_0^i being an initial value vector which is a constant with respect to time (or frequency) and contains the polarization information of the incident field. Note that the field in (5.3) is from the source and travels to the observer along a straight line of length s^i . The TD-UTD generalized reflected field $\mathbf{E}_I^{gr}(t)$ is given in (4.52) and the TD-UTD surface diffracted field $\mathbf{E}_I^d(t)$ is in (4.53). The surface diffracted field $\mathbf{E}_I^d(t)$ may also exist in the lit region for closed surfaces when multiple encirclements are included. In the same manner as the TD-UTD wedge scattering formulation, the impulse response formulas for the smooth surface scattering, denoted by the subscript I , may be convolved with an excitation in closed form as in (3.80) and (3.81) when the excitation has the form in (3.77) and (3.78).

The development of the TD-UTD is important for many reasons. There are many problems of engineering interest for which the more robust time domain numerical methods (such as the finite difference time domain (FDTD), or the time domain integral equations (TD-IE) method) are not well suited, because the geometries are too large in terms of pulse width. Also, the TD-UTD can provide an approximate impulse response which may provide more interesting information about a scatterer or an antenna, since the impulse response is essentially independent of excitation waveform shape. In addition, the development of the TD-UTD has requires the use of some novel techniques such as the analytic time transform (ATT) and so forth, there are many other research topics which the development of the TD-UTD and the ATT may have a positive benefit.

An important observation from the development of the TD-UTD is that the early time asymptotic results obtained from the high frequency asymptotic frequency do-

main solutions are not necessarily causal. This is understood now, because the early time results correspond to scattering from localized portions of an object, and the shifted times about which they are asymptotically valid is NOT the so called "turn on time" for the general geometry. This is an important observation, because it rules out using an inverse Laplace transform for solving general problems since the inverse Laplace transform only provides one-sided time functions. Although, in principle a two-sided Laplace transform or a Fourier transform could be used, the ATT developed in Chapter 2 is much more convenient. The analytic time signals obtained from the ATT provide a very compact general solution which can be convolved with a broad class of excitation functions in closed form.

The TD-UTD formulations developed in this report for a general curved wedge including slope diffraction and for the diffraction from smooth convex curved surfaces (scattering case) represent a substantial progress towards achieving a full TD-UTD framework which is just as useful as the frequency domain UTD. Nonetheless, there is a lot of research which still must be done to extend the usefulness of the TD-UTD even farther. First of all, work should be done on improving the efficiency of computing the TD-UTD transition functions (related to the Fock type function) in the smooth surface diffraction coefficient. Although the numerical algorithm described in Appendix E is adequate for most purposes, it is likely that there is a more efficient method for the calculation since accuracy not efficiency was the primary concern in the development of the numerical algorithm in Appendix E. Next, there are still some canonical (localized) geometries to be analyzed such as the coupling and radiation problems for antennas located on smooth convex surfaces, diffraction from a vertex, a general equivalent current type of formulation for observations near caustics, an impedance wedge, and so on. In particular, the development of the TD-UTD solution to the coupling and radiation on/from smooth convex surfaces should essentially follow the approach used for the scattering case considered in this report.

In addition to the obvious potential research topics concerning the TD-UTD mentioned above, there are some other potential research problems related to the TD-UTD. One of these topics is using the TD-UTD as the guiding principle in the de-

velopment of new parametric models used in the analysis of radar scattering data [5, 6]. There are some inherent benefits of formulating parametric scattering models in the time domain (or more generally the image domain) instead of the frequency domain since for scatterers large in terms of wavelength (or pulse width) the terms in the parametric model naturally become isolated in time. Another potential use of the TD-UTD is in the development of a hybrid numerical method combining a robust numerical approach such as the finite difference time domain (FDTD) or time domain integral equations (TD-IE) with an asymptotic ray based methodology. Although, it is not currently known how a hybrid time domain numerical method such as this would perform, it is felt that the TD-UTD formulation as presented in this report would be helpful in its development.

Recently, there has been a great interest in a new type of transform called the wavelet transform [54, 55]. There are fundamentally two types of wavelet transforms; the discrete wavelet transform (DWT) and continuous wavelet transform (CWT). It appears that the DWT is more popular because there have been recent developments in fast algorithms for the computation of the DWT. Nonetheless, it turns out that the second time derivative of the ATT defined in (2.11) is a continuous wavelet expansion. See Kaiser [56] to understand this relationship. In particular, Chapter 9 of [56] "Introduction to Wavelet Electromagnetics" is very helpful. To utilize this CWT, there may be further modifications necessary to compensate for the poor behavior of the asymptotic high frequency results at the low frequencies, but these modifications should be trivial. Because of the observation that the ATT is actually a CWT, the TD-UTD which uses the ATT may be applied to compute time-scale or time-frequency distributions of various diffraction phenomena directly or essentially in closed form. It is not known if looking at the TD-UTD formulation from a wavelet transform perspective would be helpful, but there may be future research opportunities here.

In summary, the current development of the TD-UTD will likely impact many areas of research beyond just the analysis of electromagnetic radiation and scattering phenomena, because of the novel use of the ATT and also the increased insight into transient electromagnetics.

Appendix A

Synthesis of an Arbitrary Finite Energy Time Pulse for Efficient Convolution

This appendix describes one practical method of obtaining the parameters in the model of the excitation waveform in (2.68) or (3.78). As discussed earlier, the advantage of using the model in (2.68) or (3.78) is that the convolution of this model with the TD-UTD impulse response can be performed in closed form as shown in (2.70) or (3.80).

Assume that the constants $\{A_n\}$ are real and $\alpha_n = \alpha'_n + j\alpha''_n$ where α'_n and α''_n are real for $n = 1, \dots, N$. Now, the real time waveform constructed by the model (using the series in (2.68) or (3.78)) is

$$F(t) = \text{Re } \overset{+}{F}(t) = \frac{1}{\pi} \sum_{n=1}^N \frac{A_n \alpha'_n}{(t - \alpha''_n)^2 + \alpha'^2_n} \quad \text{for } \text{Im } t = 0 \quad (\text{A.1})$$

Assume that the entire excitation pulse $F_0^i(t)$ is contained in the time interval $0 \leq t \leq a$ (or at least approximately contained within this interval). Notice that the parameter α''_n controls the position of the n^{th} expansion term on the t axis while α'_n controls the "width" of the n^{th} term. It would be convenient to select explicit values (which may depend on the index n) for the parameters α'_n and α''_n so that the solution for the A_n parameters will be a "system of linear equations" type of problem. Let the expansion functions be equally spaced along the t axis and choose

$$\alpha''_n = (n-1) \frac{a}{N-1} \quad (\text{A.2})$$

for $n = 1, \dots, N$. Let the “width” of the expansion functions be constant ($\alpha'_n = \alpha'$ for all n) and enforce

$$\alpha' \geq \frac{1}{2} \frac{a}{N-1}$$

to make sure the expansion functions are wide enough. Typically, one can choose $\alpha' = 0.75(a/(N-1))$ or $\alpha' = 1.0(a/(N-1))$ for satisfactory results. Note that choosing an α' value that is too large may make the expansion approximation have a large “tail” for times where the excitation waveform is actually zero, on the other hand choosing α' too small may cause too much “ripple” in the expansion approximation. Now sample the excitation waveform $F_0^i(t)$ at M points defined by

$$t_m = (m-1) \frac{a}{M-1}$$

for $m = 1, 2, \dots, M$ and $M \geq N$. The expansion in (A.1) is set equal to the excitation waveform $F_0^i(t)$ at these sample points to form an overdetermined system of linear equations

$$[C][A] = [B] \tag{A.3}$$

where

$$[C]_{mn} = \frac{1}{\pi} \frac{\alpha'_n}{(t_m - \alpha'_n)^2 + \alpha_n'^2} \tag{A.4}$$

$$[B]_m = F_0^i(t_m) \tag{A.5}$$

$$[A]_n = A_n \tag{A.6}$$

One can solve the overdetermined system of equations in (A.3) in a least squares sense by using the singular value decomposition (SVD) [57]. Or, a simpler but less robust approach to solve (A.3) in a least squares sense is to form the moment equations

$$[C]^T[C][A] = [C]^T[B] \tag{A.7}$$

and then use Cholesky decomposition on (A.7) to solve for the unknown vector $[A]$ [57]. The solution of these equations provides the $\{A_n\}$ parameters and all the parameters in the expansion are now specified.

Appendix B

Exact Time Domain Field of an Arbitrarily Oriented Electric or Magnetic Dipole in the Presence of a Perfectly Conducting Wedge

This appendix summarizes an exact time domain solution for the electromagnetic field from an arbitrarily oriented electric or magnetic dipole in the presence of a perfectly conducting wedge. The solution in this appendix is based on Felsen's work [22]. In this appendix, a " \sim " on top of a variable indicates that it is a frequency domain quantity. An $e^{j\omega t}$ time convention is used for the frequency domain quantities in this appendix.

The coordinate system used here is shown in Figure B.1. Without loss of generality the source is assumed to lie in the $z = 0$ plane and the observer may be out of this plane. The wedge angle α is assumed to be less than 180 degrees, but the solution for the general case is given by Felsen [22]. The more general case simply includes more image contributions, whereas for the $\alpha < 180$ case there is at most one image contribution to the geometrical optics field corresponding to the reflected ray.

B.1 Electric Dipole Case

Electromagnetic fields can be expressed in terms of vector potentials. Felsen chooses to use Hertz vector potentials in [22] so they are also used here. The electric field \mathbf{E} and magnetic field \mathbf{H} can be expressed in terms of the electric Hertz vector potential

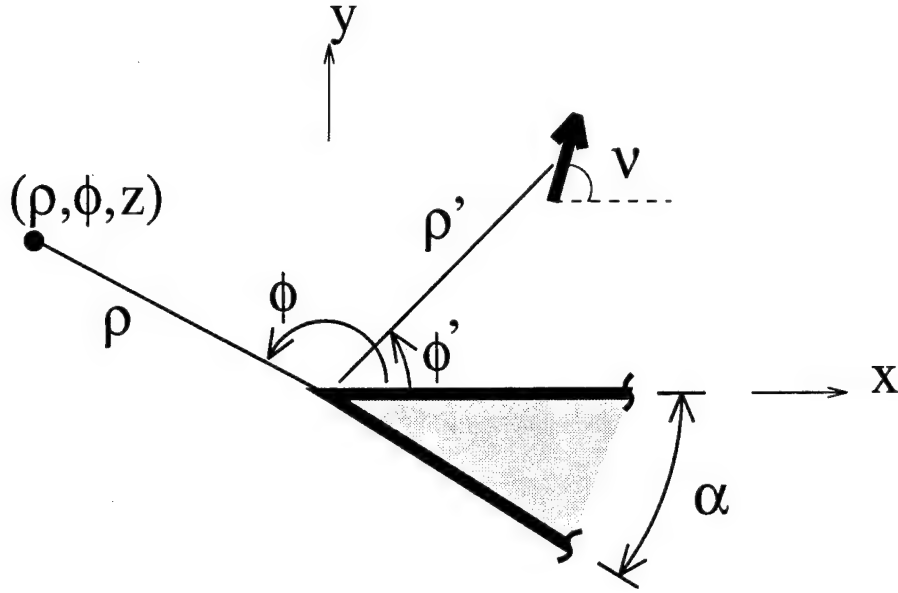


Figure B.1: An electric (or magnetic) dipole radiating in the presence of a PEC wedge. The dipole is in the $z = 0$ plane but the observer may be out of this plane.

Π by [58]

$$\mathbf{E} = \nabla \nabla \cdot \Pi - \mu \epsilon \frac{\partial^2}{\partial t^2} \Pi \quad (\text{B.1})$$

$$\mathbf{H} = \epsilon \nabla \times \frac{\partial}{\partial t} \Pi \quad (\text{B.2})$$

in the time domain, or

$$\tilde{\mathbf{E}} = \nabla \nabla \cdot \tilde{\Pi} + \omega^2 \mu \epsilon \tilde{\Pi} \quad (\text{B.3})$$

$$\tilde{\mathbf{H}} = j\omega \epsilon \nabla \times \tilde{\Pi} \quad (\text{B.4})$$

in the frequency domain. The space surrounding the wedge is assumed to be a linear homogeneous isotropic nonconducting medium, and the permittivity ϵ and permeability μ are constants with respect to space and time (or frequency). The electromagnetic fields satisfy Maxwell's Equations

$$\nabla \times \mathbf{H} = \epsilon \frac{\partial \mathbf{E}}{\partial t} + \frac{\partial \mathbf{P}}{\partial t} \quad (\text{B.5})$$

$$\nabla \times \mathbf{E} = -\mu \frac{\partial \mathbf{H}}{\partial t} \quad (\text{B.6})$$

$$\nabla \cdot \mathbf{E} = -\frac{1}{\epsilon} \nabla \cdot \mathbf{P} \quad (\text{B.7})$$

$$\nabla \cdot \mathbf{H} = 0 \quad (\text{B.8})$$

where \mathbf{P} is an electric dipole moment density which is related to the electric current density \mathbf{J} by

$$\mathbf{J} = \frac{\partial}{\partial t} \mathbf{P}. \quad (\text{B.9})$$

The Hertz electric vector $\mathbf{\Pi}$ satisfies the wave equation

$$\nabla^2 \mathbf{\Pi} - \mu\epsilon \frac{\partial^2}{\partial t^2} \mathbf{\Pi} = -\frac{1}{\epsilon} \mathbf{P}. \quad (\text{B.10})$$

Notice that the Hertz electric vector $\mathbf{\Pi}$ is related to the conventional vector potential \mathbf{A} by [59]

$$\mathbf{A} = \mu\epsilon \frac{\partial \mathbf{\Pi}}{\partial t} \quad (\text{B.11})$$

or in the frequency domain

$$\tilde{\mathbf{A}} = j\omega\mu\epsilon\tilde{\mathbf{\Pi}}. \quad (\text{B.12})$$

In the far zone, defined here as the limit $r \rightarrow \infty$, the Hertz vector can be written as

$$\tilde{\mathbf{\Pi}} \sim \frac{e^{-jkr}}{r} \tilde{\mathbf{f}}_p(\theta, \phi) \quad \text{for } r \rightarrow \infty \quad (\text{B.13})$$

and the electric field becomes

$$\tilde{\mathbf{E}} \sim -\frac{\omega^2}{c^2} \frac{e^{-jkr}}{r} \hat{\mathbf{r}} \times \hat{\mathbf{r}} \times \tilde{\mathbf{f}}_p(\theta, \phi) \quad \text{for } r \rightarrow \infty \quad (\text{B.14})$$

where $c^2 = 1/(\mu\epsilon)$. In the time domain, these far zone relationships become

$$\mathbf{\Pi} \sim \frac{1}{r} \mathbf{f}_p(\theta, \phi, t - r/c) \quad \text{for } r \rightarrow \infty \quad (\text{B.15})$$

$$\mathbf{E} \sim \frac{1}{c^2 r} \frac{\partial^2}{\partial t^2} \hat{\mathbf{r}} \times \hat{\mathbf{r}} \times \mathbf{f}_p(\theta, \phi, t - r/c) \quad \text{for } r \rightarrow \infty. \quad (\text{B.16})$$

Usually, the $1/r$ factor and r/c time delay in (B.15) or (B.16) are not included in far zone calculations.

The "impulse response" in this appendix is defined in terms of the dominant term of the electric field incident on the wedge, therefore to obtain the impulse response let the electric dipole moment density have a ramp time dependence as in

$$\mathbf{P}(t) = \hat{\mathbf{p}} \delta(\mathbf{r} - \mathbf{r}') t u(t) \quad (\text{B.17})$$

or equivalently let the electric current element be

$$\mathbf{J}(t) = \hat{\mathbf{p}} \delta(\mathbf{r} - \mathbf{r}') u(t) \quad (\text{B.18})$$

where $u(t)$ is the unit step function.

The Geometrical Optics Field

It is assumed here that the orientation of the dipole $\hat{\mathbf{p}}$ is contained in the $z = 0$ plane (i.e. a transverse source). The solution for a longitudinal source can be found in Felsen's book [34].

The Hertz vector can be written as

$$\mathbf{\Pi} = \mathbf{\Pi}^{\text{go}} + \mathbf{\Pi}^{\text{d}} \quad (\text{B.19})$$

where $\mathbf{\Pi}^{\text{go}}$ corresponds to the geometrical optics (GO) field, while $\mathbf{\Pi}^{\text{d}}$ corresponds to the diffracted field. When the wedge angle α is less than 180 degrees, the GO Hertz vector can be written as two terms

$$\begin{aligned} \mathbf{\Pi}^{\text{go}} = & \hat{\mathbf{p}} \frac{1}{4\pi\epsilon} \frac{(t - |\mathbf{r} - \mathbf{r}'|)u(t - |\mathbf{r} - \mathbf{r}'|)}{|\mathbf{r} - \mathbf{r}'|} u(\pi - |\phi - \phi'|) \\ & + \hat{\mathbf{p}}_i \frac{1}{4\pi\epsilon} \frac{(t - |\mathbf{r} - \mathbf{r}'_i|)u(t - |\mathbf{r} - \mathbf{r}'_i|)}{|\mathbf{r} - \mathbf{r}'_i|} u(\pi - |\phi - \phi'_i|) \end{aligned} \quad (\text{B.20})$$

where the orientation of the dipole is

$$\hat{\mathbf{p}} = \hat{\mathbf{x}} \cos \nu + \hat{\mathbf{y}} \sin \nu \quad (\text{B.21})$$

and the orientation of the image is

$$\hat{\mathbf{p}}_i = -\hat{\mathbf{x}} \cos \nu + \hat{\mathbf{y}} \sin \nu. \quad (\text{B.22})$$

The position of the dipole in cylindrical coordinates is $\mathbf{r}' = (\rho', \phi', 0)$, while the position of the image source is $\mathbf{r}'_i = (\rho', \phi'_i, 0)$ where $\phi'_i = 2\pi - \phi'$.

To obtain the far zone ($r \rightarrow \infty$) expressions use

$$|\mathbf{r} - \mathbf{r}_0| \sim \begin{cases} r & \text{in magnitude} \\ r - \hat{\mathbf{r}} \cdot \mathbf{r}_0 & \text{in phase (or time delay)} \end{cases} \quad (\text{B.23})$$

where \mathbf{r}_0 may be \mathbf{r}' or \mathbf{r}'_i . Using the above far zone approximation, the Hertz vector becomes

$$\begin{aligned} \mathbf{\Pi}^{\text{go}} \sim & \hat{\mathbf{p}} \frac{1}{4\pi\epsilon} \frac{(\tau + \hat{\mathbf{r}} \cdot \mathbf{r}'/c)u(\tau + \hat{\mathbf{r}} \cdot \mathbf{r}'/c)}{r} u(\pi - |\phi - \phi'|) \\ & + \hat{\mathbf{p}}_i \frac{1}{4\pi\epsilon} \frac{(\tau + \hat{\mathbf{r}} \cdot \mathbf{r}'_i/c)u(\tau + \hat{\mathbf{r}} \cdot \mathbf{r}'_i/c)}{r} u(\pi - |\phi - \phi'_i|) \end{aligned} \quad (\text{B.24})$$

where $\tau = t - r/c$. Using the above result together with (B.15) and (B.16), the far zone geometrical optics electric field can be written down from inspection as

$$\begin{aligned} \mathbf{E}^{\text{go}} \sim & \hat{\mathbf{r}} \times \hat{\mathbf{r}} \times \hat{\mathbf{p}} \frac{Z_0}{4\pi r c} \delta(\tau + \hat{\mathbf{r}} \cdot \mathbf{r}'/c) u(\pi - |\phi - \phi'|) \\ & + \hat{\mathbf{r}} \times \hat{\mathbf{r}} \times \hat{\mathbf{p}}_i \frac{Z_0}{4\pi r c} \delta(\tau + \hat{\mathbf{r}} \cdot \mathbf{r}'_i/c) u(\pi - |\phi - \phi'_i|) \end{aligned} \quad (\text{B.25})$$

where $Z_0 = \sqrt{\mu/\epsilon}$.

The Diffracted Field

The Hertz vector corresponding to the diffracted field Π^d as presented by Felsen is repeated here for convenience [22]. Also, the simplification of Π^d for an observer in the far zone and the electric field in the far zone is derived.

When the orientation of the dipole $\hat{\mathbf{p}}$ is transverse to z the solution is obtained from only the transverse components of the Hertz vector $\Pi = \hat{\mathbf{x}}\Pi_x + \hat{\mathbf{y}}\Pi_y$. Felsen gives [22]

$$\frac{\partial^2}{\partial t^2} \Pi_{x,y}^d = -\frac{c}{4\pi^2 \epsilon} \frac{\text{Re} [A_{x,y}(\phi, \phi', -i\beta)]}{\rho \rho' \sinh \beta} u(t - r/c) \quad (\text{B.26})$$

where the double time derivative on $\Pi_{x,y}^d$ occurs because Felsen uses the source $\mathbf{P} = \hat{\mathbf{p}}\delta(\mathbf{r} - \mathbf{r}')\delta(t)$ which is the double time derivative of the source used here. The other parameters in (B.26) are

$$\beta = \cosh^{-1} \left[\frac{c^2 t^2 - \rho^2 - \rho'^2 - z^2}{2\rho\rho'} \right] \quad (\text{B.27})$$

$$r = \sqrt{(\rho + \rho')^2 + z^2} \quad (\text{B.28})$$

and

$$\begin{aligned} A_x(\phi, \phi', w) = & -\frac{\pi}{2\alpha} \{ [Q_1(\phi - \phi', w) - Q_1(\phi + \phi', w)] \cos \nu \\ & - [Q_2(\phi - \phi', w) + Q_2(\phi + \phi', w)] \sin \nu \} \end{aligned} \quad (\text{B.29})$$

$$\begin{aligned} A_y(\phi, \phi', w) = & -\frac{\pi}{2\alpha} \{ [Q_2(\phi - \phi', w) - Q_2(\phi + \phi', w)] \cos \nu \\ & + [Q_1(\phi - \phi', w) + Q_1(\phi + \phi', w)] \sin \nu \} \end{aligned} \quad (\text{B.30})$$

with

$$\begin{aligned} Q_1(\psi, w) &= \cos(\psi - w - \pi) \cot \left(\frac{\psi - w - \pi}{2\alpha/\pi} \right) \\ &\quad - \cos(\psi + w + \pi) \cot \left(\frac{\psi + w + \pi}{2\alpha/\pi} \right) \end{aligned} \quad (\text{B.31})$$

$$\begin{aligned} Q_2(\psi, w) &= \sin(\psi - w - \pi) \cot \left(\frac{\psi - w - \pi}{2\alpha/\pi} \right) \\ &\quad - \sin(\psi + w + \pi) \cot \left(\frac{\psi + w + \pi}{2\alpha/\pi} \right) \end{aligned} \quad (\text{B.32})$$

To obtain the far zone expressions, the following far zone approximation is used

$$\frac{c^2 t^2 - \rho^2 - \rho'^2 - z^2}{2\rho\rho'} \sim \frac{c\tau}{\rho' \sin \theta} \quad \text{for } r \rightarrow \infty \quad (\text{B.33})$$

where

$$\tau = t - r/c \quad (\text{B.34})$$

and notice that

$$\sinh \left[\cosh^{-1} \left(\frac{c\tau}{\rho' \sin \theta} \right) \right] = \frac{1}{\rho' \sin \theta} \sqrt{c^2 \tau^2 - \rho'^2 \sin^2 \theta}. \quad (\text{B.35})$$

So, in the far zone, the Hertz vector $\Pi_{x,y}^d$ becomes

$$\frac{\partial^2}{\partial t^2} \Pi_{x,y}^d \sim \frac{-c}{4\pi^2 \epsilon r} \frac{\text{Re} [A_{x,y}(\phi, \phi', -j\beta)]}{\sqrt{c^2 \tau^2 - \rho'^2 \sin^2 \theta}} u \left(\tau - \frac{\rho'}{c} \sin \theta \right) \quad (\text{B.36})$$

where

$$\beta \sim \cosh^{-1} \left[\frac{c\tau}{\rho' \sin \theta} \right]. \quad (\text{B.37})$$

Now the far zone diffracted electric field can be written down

$$\begin{aligned} \mathbf{E}^d &\sim -\frac{Z_0}{4\pi^2 r} \hat{\mathbf{r}} \times \hat{\mathbf{r}} \times \{ \hat{\mathbf{x}} \text{Re} [A_x(\phi, \phi', -j\beta)] \\ &\quad + \hat{\mathbf{y}} \text{Re} [A_y(\phi, \phi', -j\beta)] \} \frac{u \left(\tau - \frac{\rho'}{c} \sin \theta \right)}{\sqrt{c^2 \tau^2 - \rho'^2 \sin^2 \theta}}. \end{aligned} \quad (\text{B.38})$$

B.2 Magnetic Dipole Case

Once again, the electromagnetic fields can be expressed in terms of vector potentials. Felsen chooses to use Hertz vector potentials in [22] so they are also used here. The electric field \mathbf{E} can be expressed in terms of the magnetic Hertz vector potential $\mathbf{\Pi}^m$ by [58]

$$\mathbf{E} = -\mu \frac{\partial}{\partial t} \nabla \times \mathbf{\Pi}^m \quad (\text{B.39})$$

in the time domain, or

$$\mathbf{E} = -j\omega\mu \nabla \times \mathbf{\Pi}^m \quad (\text{B.40})$$

in the frequency domain. The electromagnetic fields satisfy Maxwell's Equations

$$\nabla \times \mathbf{H} = \epsilon \frac{\partial \mathbf{E}}{\partial t} \quad (\text{B.41})$$

$$\nabla \times \mathbf{E} = -\mu \frac{\partial \mathbf{H}}{\partial t} - \mu \frac{\partial \mathbf{M}}{\partial t} \quad (\text{B.42})$$

$$\nabla \cdot \mathbf{E} = 0 \quad (\text{B.43})$$

$$\nabla \cdot \mathbf{H} = -\nabla \cdot \mathbf{M} \quad (\text{B.44})$$

where \mathbf{M} is a magnetic dipole moment density which is related to the magnetic current \mathbf{K} by

$$\mathbf{K} = \mu \frac{\partial}{\partial t} \mathbf{M}. \quad (\text{B.45})$$

The magnetic Hertz vector $\mathbf{\Pi}^m$ satisfies the wave equation

$$\nabla^2 \mathbf{\Pi}^m - \mu\epsilon \frac{\partial^2}{\partial t^2} \mathbf{\Pi}^m = -\mathbf{M}. \quad (\text{B.46})$$

Notice that the Hertz magnetic vector $\mathbf{\Pi}^m$ is related to the conventional vector potential \mathbf{F} by [59]

$$\mathbf{F} = \mu\epsilon \frac{\partial \mathbf{\Pi}^m}{\partial t} \quad (\text{B.47})$$

or in the frequency domain

$$\tilde{\mathbf{F}} = j\omega\mu\epsilon \tilde{\mathbf{\Pi}}^m. \quad (\text{B.48})$$

In the far zone, defined here as the limit $r \rightarrow \infty$, the Hertz vector can be written as

$$\tilde{\Pi}^m \sim \frac{e^{-jkr}}{r} \tilde{\mathbf{g}}^m(\theta, \phi) \quad \text{for } r \rightarrow \infty \quad (\text{B.49})$$

and the electric field becomes

$$\tilde{\mathbf{E}} \sim -\frac{\omega^2 \mu}{c} \frac{e^{-jkr}}{r} \hat{\mathbf{r}} \times \tilde{\mathbf{g}}^m(\theta, \phi) \quad \text{for } r \rightarrow \infty. \quad (\text{B.50})$$

In the time domain, these far zone relationships become

$$\Pi^m \sim \frac{1}{r} \mathbf{g}^m(\theta, \phi, t - r/c) \quad \text{for } r \rightarrow \infty \quad (\text{B.51})$$

$$\mathbf{E} \sim \frac{\mu}{cr} \frac{\partial^2}{\partial t^2} \hat{\mathbf{r}} \times \mathbf{g}^m(\theta, \phi, t - r/c) \quad \text{for } r \rightarrow \infty \quad (\text{B.52})$$

Usually, the $1/r$ factor and r/c time delay are not included in the far zone calculations.

The “impulse response” in this appendix is defined in terms of the dominant term of the electric field incident on the wedge, therefore to obtain the impulse response let the magnetic dipole moment density have a ramp time dependence as in

$$\mathbf{M}(t) = \frac{1}{\mu} \hat{\mathbf{m}} \delta(\mathbf{r} - \mathbf{r}') t u(t) \quad (\text{B.53})$$

or equivalently let the magnetic current element have a step time dependence as in

$$\mathbf{K}(t) = \hat{\mathbf{m}} \delta(\mathbf{r} - \mathbf{r}') u(t) \quad (\text{B.54})$$

where $u(t)$ is the unit step function.

The Geometrical Optics Field

It is assumed here that the orientation of the magnetic dipole $\hat{\mathbf{m}}$ is contained in the $z = 0$ plane (i.e. a transverse source). The longitudinal source case can be found in Felsen's book [34].

The Hertz vector can be written as

$$\Pi^m = \Pi^{m,go} + \Pi^{m,d} \quad (\text{B.55})$$

where $\Pi^{m,go}$ corresponds to the geometrical optics (GO) field, while $\Pi^{m,d}$ corresponds to the diffracted field. When the wedge angle α is less than 180 degrees, the GO Hertz vector can be written as two terms

$$\begin{aligned}\Pi^{m,go} = & \hat{\mathbf{m}} \frac{1}{4\pi\mu} \frac{(t - |\mathbf{r} - \mathbf{r}'|)u(t - |\mathbf{r} - \mathbf{r}'|)}{|\mathbf{r} - \mathbf{r}'|} u(\pi - |\phi - \phi'|) \\ & + \hat{\mathbf{m}}_i \frac{1}{4\pi\mu} \frac{(t - |\mathbf{r} - \mathbf{r}'_i|)u(t - |\mathbf{r} - \mathbf{r}'_i|)}{|\mathbf{r} - \mathbf{r}'_i|} u(\pi - |\phi - \phi'_i|)\end{aligned}\quad (\text{B.56})$$

where the orientation of the magnetic dipole is

$$\hat{\mathbf{m}} = \hat{\mathbf{x}} \cos \nu + \hat{\mathbf{y}} \sin \nu \quad (\text{B.57})$$

and the orientation of the image is

$$\hat{\mathbf{m}}_i = \hat{\mathbf{x}} \cos \nu - \hat{\mathbf{y}} \sin \nu. \quad (\text{B.58})$$

The position of the magnetic dipole in cylindrical coordinates is $\mathbf{r}' = (\rho', \phi', 0)$, while the position of the image source is $\mathbf{r}'_i = (\rho', \phi'_i, 0)$ where $\phi'_i = 2\pi - \phi'$.

To obtain the far zone ($r \rightarrow \infty$) expressions use

$$|\mathbf{r} - \mathbf{r}_0| \sim \begin{cases} r & \text{in magnitude} \\ r - \hat{\mathbf{r}} \cdot \mathbf{r}_0 & \text{in phase (or time delay)} \end{cases} \quad (\text{B.59})$$

where \mathbf{r}_0 may be \mathbf{r}' or \mathbf{r}'_i . Using the above far zone approximation, the magnetic Hertz vector becomes

$$\begin{aligned}\Pi^{m,go} \sim & \hat{\mathbf{m}} \frac{1}{4\pi\mu} \frac{(\tau + \hat{\mathbf{r}} \cdot \mathbf{r}'/c)u(\tau + \hat{\mathbf{r}} \cdot \mathbf{r}'/c)}{r} u(\pi - |\phi - \phi'|) \\ & + \hat{\mathbf{m}}_i \frac{1}{4\pi\mu} \frac{(\tau + \hat{\mathbf{r}} \cdot \mathbf{r}'_i/c)u(\tau + \hat{\mathbf{r}} \cdot \mathbf{r}'_i/c)}{r} u(\pi - |\phi - \phi'_i|)\end{aligned}\quad (\text{B.60})$$

where $\tau = t - r/c$. Using the above result together with (B.51) and (B.52), the far zone geometrical optics electric field can be written down from inspection as

$$\begin{aligned}\mathbf{E}^{go} \sim & \hat{\mathbf{r}} \times \hat{\mathbf{m}} \frac{1}{4\pi r c} \delta(\tau + \hat{\mathbf{r}} \cdot \mathbf{r}'/c) u(\pi - |\phi - \phi'|) \\ & + \hat{\mathbf{r}} \times \hat{\mathbf{m}}_i \frac{1}{4\pi r c} \delta(\tau + \hat{\mathbf{r}} \cdot \mathbf{r}'_i/c) u(\pi - |\phi - \phi'_i|).\end{aligned}\quad (\text{B.61})$$

The Diffracted Field

The magnetic Hertz vector corresponding to the diffracted field $\Pi^{m,d}$ as presented by Felsen is repeated here for convenience [22]. Also, the simplification of $\Pi^{m,d}$ for an observer in the far zone and the electric field in the far zone are presented.

When the orientation of the magnetic dipole $\hat{\mathbf{m}}$ is transverse to z the solution is obtained from only the transverse components of the Hertz vector $\Pi^m = \hat{\mathbf{x}}\Pi_x^m + \hat{\mathbf{y}}\Pi_y^m$. Felsen gives [22]

$$\frac{\partial^2}{\partial t^2} \Pi_{x,y}^{m,d} = -\frac{c}{4\pi^2} \frac{\text{Re} [A_{x,y}^m(\phi, \phi', -i\beta)]}{\rho\rho' \sinh\beta} u(t - r/c) \quad (\text{B.62})$$

where the double time derivative on $\Pi_{x,y}^{m,d}$ occurs because Felsen uses the source $\mathbf{M} = \frac{1}{\mu} \hat{\mathbf{m}} \delta(\mathbf{r} - \mathbf{r}') \delta(t)$ which is the double time derivative of the source used here. The parameters in (B.62) are the same as in the electric dipole case, except

$$\begin{aligned} A_x^m(\phi, \phi', w) &= -\frac{\pi}{2\alpha} \{ [Q_1(\phi - \phi', w) + Q_1(\phi + \phi', w)] \cos \nu \\ &\quad - [Q_2(\phi - \phi', w) - Q_2(\phi + \phi', w)] \sin \nu \} \end{aligned} \quad (\text{B.63})$$

$$\begin{aligned} A_y^m(\phi, \phi', w) &= -\frac{\pi}{2\alpha} \{ [Q_2(\phi - \phi', w) + Q_2(\phi + \phi', w)] \cos \nu \\ &\quad + [Q_1(\phi - \phi', w) - Q_1(\phi + \phi', w)] \sin \nu \} \end{aligned} \quad (\text{B.64})$$

The far zone expressions are obtained in the same manner as in the electric dipole case. In the far zone, the Hertz vector $\Pi_{x,y}^{m,d}$ becomes

$$\frac{\partial^2}{\partial t^2} \Pi_{x,y}^{m,d} \sim \frac{-c}{4\pi^2 r} \frac{\text{Re} [A_{x,y}^m(\phi, \phi', -j\beta)]}{\sqrt{c^2 \tau^2 - \rho'^2 \sin^2 \theta}} u\left(\tau - \frac{\rho'}{c} \sin \theta\right) \quad (\text{B.65})$$

where

$$\beta \sim \cosh^{-1} \left[\frac{c\tau}{\rho' \sin \theta} \right] \quad (\text{B.66})$$

as $r \rightarrow \infty$, and

$$\tau = t - r/c. \quad (\text{B.67})$$

Now the far zone diffracted electric field can be written down

$$\begin{aligned} \mathbf{E}^d &\sim -\frac{1}{4\pi^2 r} \hat{\mathbf{r}} \times \{ \hat{\mathbf{x}} \text{Re} [A_x^m(\phi, \phi', -j\beta)] \\ &\quad + \hat{\mathbf{y}} \text{Re} [A_y^m(\phi, \phi', -j\beta)] \} \frac{u\left(\tau - \frac{\rho'}{c} \sin \theta\right)}{\sqrt{c^2 \tau^2 - \rho'^2 \sin^2 \theta}} \end{aligned} \quad (\text{B.68})$$

as $r \rightarrow \infty$.

Appendix C

Derivation of Two TD-UTD Slope Diffraction Coefficients, One Based on Veruttipong's Work and the Other on Hwang's Work

This appendix derives two versions of the TD-UTD slope diffraction coefficient; one version is based on a frequency domain slope diffraction coefficient derived by Hwang and Kouyoumjian [21, 4] and the other is based on a frequency domain slope diffraction coefficient derived by Veruttipong and Kouyoumjian [20]. For simplicity, these two results will be referred to as Hwang's version and Veruttipong's version of slope diffraction, respectively. The TD-UTD slope diffraction coefficient for either case is obtained by an application of the analytic time transform (ATT) described in Chapter 2.

Hwang obtains the slope diffraction coefficient by taking the derivative with respect to ϕ' of the exact straight wedge diffraction coefficient, where this exact coefficient is written as a spectral integral. The operations of integration and differentiation are interchanged and the new spectral integral is evaluated asymptotically. On the other hand, Veruttipong finds the slope diffraction coefficient by taking the derivative with respect to ϕ' of the UTD wedge diffraction coefficient, where the UTD coefficient is obtained by an asymptotic evaluation of the exact diffraction coefficient. So, Veruttipong takes the derivative of an asymptotic expression whereas Hwang inter-

changes the derivative and integration operations first and then does the asymptotic evaluation.

This appendix derives the time domain slope diffraction coefficients for the straight wedge, but these slope diffraction coefficients can be generalized to the curved wedge case as is done in Chapter 3.

C.1 Hwang's Slope Diffraction Coefficient

Hwang's frequency domain slope diffraction coefficient for a straight wedge can be written as

$$D_{s,h}^s = \frac{-1}{4n^2\sqrt{2\pi}\sin^2\beta_0} \sum_{m=1}^4 C_m^{s,h} \tilde{F}_s(x_m, \omega) \quad (\text{C.1})$$

where

$$C_1^{s,h} = +\csc^2[(\pi + \beta^-)/(2n)] \quad (\text{C.2})$$

$$C_2^{s,h} = -\csc^2[(\pi - \beta^-)/(2n)] \quad (\text{C.3})$$

$$C_3^{s,h} = \pm \csc^2[(\pi + \beta^+)/(2n)] \quad (\text{C.4})$$

$$C_4^{s,h} = \mp \csc^2[(\pi - \beta^+)/(2n)] \quad (\text{C.5})$$

and

$$\tilde{F}_s(x_m, \omega) = 2x_m \left[\frac{\sqrt{c}}{\sqrt{j\omega}} - \tilde{F}(x_m, \omega) \right] \quad (\text{C.6})$$

with

$$\tilde{F}(x_m, \omega) = \sqrt{\frac{c}{j\omega}} \tilde{F}_{tr} \left(\frac{\omega x_m}{c} \right) \quad (\text{C.7})$$

where $F_{tr}(z)$ is the UTD transition function defined by

$$\tilde{F}_{tr}(z) = 2j\sqrt{z}e^{jz} \int_{\sqrt{z}}^{\infty} e^{-j\tau^2} d\tau \quad (\text{C.8})$$

The $\tilde{F}(x_m, \omega)$ function can also be written as

$$\tilde{F}(x_m, \omega) = \sqrt{\pi x_m} e^{j\omega x_m/c} \text{erfc} \left(\sqrt{\frac{j\omega x_m}{c}} \right) \quad (\text{C.9})$$

as is done in Chapter 3. The x_m for a straight wedge are defined by

$$x_1 = La^+(\beta^-) \quad (\text{C.10})$$

$$x_2 = La^-(\beta^-) \quad (C.11)$$

$$x_3 = La^+(\beta^+) \quad (C.12)$$

$$x_4 = La^-(\beta^+) \quad (C.13)$$

where $a^\pm(\beta) = 2 \cos^2[(2n\pi N^\pm - \beta)/2]$ and N^\pm is the nearest integer solution of $2\pi n N^\pm - \beta = \pm\pi$. The L parameter for a straight wedge can be found in [4, 2].

Now the TD-UTD slope diffraction coefficient based on Hwang's coefficient is

$$\overset{+}{D}_{s,h}^s(t) = \frac{-1}{4n^2\sqrt{2\pi} \sin^2 \beta_0} \sum_{m=1}^4 C_m^{s,h} \overset{+}{F}_s(x_m, t) \quad (C.14)$$

where $\overset{+}{F}_s(x_m, t)$ is the analytic time transform of $\tilde{F}_s(x_m, \omega)$ given by

$$\overset{+}{F}_s(x_m, t) = 2x_m \left[\frac{e^{-j\pi/4}\sqrt{c}}{\sqrt{\pi}\sqrt{-jt}} + \frac{j\sqrt{-x_m/\pi}}{\sqrt{-jt}(\sqrt{-jt} + e^{-j\pi/4}\sqrt{-x_m/c})} \right] \quad (C.15)$$

which can be easily simplified into

$$\overset{+}{F}_s(x_m, t) = \sqrt{\frac{c}{\pi}} \frac{2x_m e^{-j\pi/4}}{\sqrt{-jt} + e^{-j\pi/4}\sqrt{-x_m/c}} \quad (C.16)$$

It is interesting to examine some special cases. Consider the straight wedge when it is illuminated by a transient pulse which is a real time impulse $\delta(t)$. For this case, $x_m > 0$ and we are only interested in the real part of the slope transition function in (C.16). First $\overset{+}{F}_s(x_m, t)$ can be written as

$$\overset{+}{F}_s(x_m, t) = \left(\frac{2x_m\sqrt{c}}{\sqrt{\pi}} \right) \frac{\sqrt{t} - e^{j\pi/2}\sqrt{x_m/c}}{t + x_m/c} \quad (C.17)$$

Now the real time function is the real part of (C.17) evaluated at real time ($\text{Im } t = 0$)

$$F_s(x_m, t) = \left(\frac{2x_m\sqrt{c}}{\sqrt{\pi}} \right) \frac{\sqrt{t}}{t + x_m/c} u(t) \quad (C.18)$$

Notice that this function is zero at $t = 0$ and has a peak at $t = x_m/c$. This signifies that the impulse response of the slope diffracted field for the straight wedge is a continuous time function and has a maximum after the time of arrival of the wavefront (i.e. the time corresponding to the diffracted ray path length). If the observation point is far from the m^{th} shadow boundary, then x_m can be considered much greater than ct and we find

$$F_s(x_m, t) \sim \frac{2c^{3/2}}{\sqrt{\pi}} \sqrt{t} u(t) \quad \text{for } \frac{x_m}{ct} \rightarrow \infty \quad (C.19)$$

C.2 Veruttipong's Slope Diffraction Coefficient

Veruttipong's frequency domain slope diffraction coefficient for a straight wedge can be written as

$$D_{s,h}^s = \frac{-1}{4n^2\sqrt{2\pi}\sin^2\beta_0} \left[\begin{aligned} &+A_1\tilde{F}_{vs}(x_1,\omega) + B_1\tilde{F}_s(x_1,\omega) \\ &-A_2\tilde{F}_{vs}(x_2,\omega) - B_2\tilde{F}_s(x_2,\omega) \\ &\pm A_3\tilde{F}_{vs}(x_3,\omega) \pm B_3\tilde{F}_s(x_3,\omega) \\ &\mp A_4\tilde{F}_{vs}(x_4,\omega) \mp B_4\tilde{F}_s(x_4,\omega) \end{aligned} \right] \quad (\text{C.20})$$

where

$$A_1 = \csc^2((\pi + \beta^-)/2n) - B_1 \quad (\text{C.21})$$

$$A_2 = \csc^2((\pi - \beta^-)/2n) - B_2 \quad (\text{C.22})$$

$$A_3 = \csc^2((\pi + \beta^+)/2n) - B_3 \quad (\text{C.23})$$

$$A_4 = \csc^2((\pi - \beta^+)/2n) - B_4 \quad (\text{C.24})$$

and

$$B_1 = +\frac{n\dot{a}^+(\beta^-)}{a^+(\beta^-)} \cot((\pi + \beta^-)/(2n)) \quad (\text{C.25})$$

$$B_2 = -\frac{n\dot{a}^-(\beta^-)}{a^-(\beta^-)} \cot((\pi - \beta^-)/(2n)) \quad (\text{C.26})$$

$$B_3 = +\frac{n\dot{a}^+(\beta^+)}{a^+(\beta^+)} \cot((\pi + \beta^+)/(2n)) \quad (\text{C.27})$$

$$B_4 = -\frac{n\dot{a}^-(\beta^+)}{a^-(\beta^+)} \cot((\pi - \beta^+)/(2n)) \quad (\text{C.28})$$

$$a^\pm(\beta) = 2\cos^2\left(\frac{2\pi nN^\pm - \beta}{2}\right) \quad (\text{C.29})$$

$$\dot{a}^\pm(\beta) = \sin(2\pi nN^\pm - \beta) \quad (\text{C.30})$$

All the other parameters in (C.20) are defined in the previous section of this appendix. The transition function $\tilde{F}_s(x_m, \omega)$ is defined in (C.6) and its analytic time transform is

(C.16). The other transition function, which only arises in Veruttipong's formulation, is

$$\tilde{F}_{vs}(x_m, \omega) = \frac{c^{3/2}}{j\omega\sqrt{j\omega}} \tilde{F}_{tr}\left(\frac{x_m\omega}{c}\right) \quad (\text{C.31})$$

where $\tilde{F}_{tr}(z)$ is the UTD transition function defined in (C.8). The $\tilde{F}_{vs}(x_m, \omega)$ function can also be written as

$$\tilde{F}(x_m, \omega) = \frac{c}{j\omega} \sqrt{\pi x_m} e^{j\omega x_m/c} \text{erfc}\left(\sqrt{\frac{j\omega x_m}{c}}\right) \quad (\text{C.32})$$

where the complement of the error function is defined as

$$\text{erfc}(z) = \frac{2}{\sqrt{\pi}} \int_z^\infty e^{-t^2} dt \quad (\text{C.33})$$

The analytic time transform of $\tilde{F}_{vs}(x_m, \omega)$ is derived as follows. First notice that

$$\tilde{F}_{vs}(x_m, \omega) = \frac{c}{j\omega} \tilde{F}(x_m, \omega) \quad (\text{C.34})$$

where $\tilde{F}(x_m, \omega)$ is defined in Chapter 3 for use in the first order diffraction and is given in (3.32) or (3.34). The analytic time transform of $\tilde{F}(x_m, \omega)$ denoted by $\tilde{F}^+(x_m, t)$ in (3.38) is derived in Chapter 3. It is repeated here for convenience

$$\begin{aligned} \tilde{F}^+(x_m, t) &= \frac{-j\sqrt{-x_m/\pi}}{\sqrt{-jt}(\sqrt{-jt} + e^{-j\pi/4}\sqrt{-x_m/c})} \\ &= \frac{x_m}{\sqrt{\pi c}} \frac{1}{\sqrt{t}(t + x_m/c)} + j \frac{\sqrt{x_m/\pi}}{t + x_m/c} \end{aligned} \quad (\text{C.35})$$

for $\text{Im } t \geq 0$ where

$$\sqrt{-x_m} = \begin{cases} j\sqrt{x_m}, & x_m > 0 \\ \sqrt{-x_m}, & x_m < 0 \end{cases} \quad (\text{C.36})$$

and $\text{Re}(\sqrt{-jt}) > 0$. The following property of the analytic time transform is used

$$\frac{1}{j\omega} \tilde{H}(\omega) \xleftrightarrow{A} \tilde{H}^{(-1)}(t) + C_0 \quad (\text{C.37})$$

where $\tilde{H}^{(-1)}(t)$ is the anti-derivative (or primitive) of $\tilde{H}(t)$ and C_0 is a constant which must be determined. Using (C.37), the analytic time transform of $\tilde{F}_{vs}(x_m, \omega)$

is

$$\begin{aligned}
\bar{F}_{vs}^+(x_m, t) &= jc\sqrt{\frac{x_m}{\pi}} \left[\ln \left(\frac{\sqrt{t} + j\sqrt{x_m/c}}{\sqrt{t} - j\sqrt{x_m/c}} \right) + \ln(t + x_m/c) \right] + C_0 \\
&= j2c\sqrt{\frac{x_m}{\pi}} \ln \left(\sqrt{t} + j\sqrt{x_m/c} \right) + C_0 \\
&= j2c\sqrt{\frac{x_m}{\pi}} \left[\ln \left| \sqrt{t} + j\sqrt{x_m/c} \right| \right. \\
&\quad \left. + j \arg \left(\sqrt{t} + j\sqrt{x_m/c} \right) \right] + C_0
\end{aligned} \tag{C.38}$$

where $\arg(z)$ is the argument of the complex number z . The constant C_0 are chosen such that $\bar{F}_{vs}^+(x_m, t) = 0$ when $t = 0$ (for $x_m > 0$). This is a reasonable requirement since in general

$$\lim_{\omega \rightarrow \infty} j\omega \tilde{H}(\omega) = \lim_{(-jt) \rightarrow 0} \left[-j \bar{H}^+(t) - jt \frac{\partial}{\partial t} \bar{H}^+(t) \right] \tag{C.39}$$

and

$$\lim_{\omega \rightarrow \infty} j\omega \bar{F}_{vs}(x_m, \omega) = 0 \tag{C.40}$$

So, the analytic time transform of $\bar{F}_{vs}(x_m, \omega)$ can be written as

$$\bar{F}_{vs}^+(x_m, t) = jc\sqrt{\frac{x_m}{\pi}} \left[\ln \left| \frac{\sqrt{t} + j\sqrt{x_m/c}}{\sqrt{x_m/c}} \right| + \arg \left(\sqrt{t} + j\sqrt{x_m/c} \right) - j\frac{\pi}{2} \right] \tag{C.41}$$

To obtain a more convenient form for calculations, use $\sqrt{x_m} = -j\sqrt{-x_m}$ (since $-\pi/2 < \arg(-x_m) < 3\pi/2$) and $\sqrt{t} = e^{j\pi/4}\sqrt{-jt}$ (since $-\pi < \arg(-jt) < \pi$) to arrive at

$$\begin{aligned}
\bar{F}_{vs}^+(x_m, t) &= \frac{2c\sqrt{-x_m}}{\sqrt{\pi}} \left[\ln \left| \frac{e^{j\pi/4}\sqrt{-jct} + \sqrt{-x_m}}{\sqrt{-x_m}} \right| \right. \\
&\quad \left. + j \arg \left(e^{j\pi/4}\sqrt{-jct} + \sqrt{-x_m} \right) - j\frac{\pi}{2} \right]
\end{aligned} \tag{C.42}$$

Appendix D

Computation of the Time Domain Creeping Wave Function

This appendix discusses the analytic time function which is used in the TD-UTD creeping wave analysis in Chapter 4. The layout of this appendix is as follows. First the creeping wave time function is defined and some of its properties are examined. Then some simple approximate formulas for small time values or large time values are derived. Finally, an efficient numerical algorithm is presented to compute the creeping wave time function for all intermediate time values.

D.1 Definitions and Properties

The creeping wave time function is defined as

$$\overset{+}{F}_{cw}(\alpha, t) = \frac{1}{\pi} \int_0^\infty (j\omega)^{-\frac{1}{6}} e^{-\alpha(j\omega)^{\frac{1}{3}}} e^{j\omega t} d\omega \quad (\text{D.1})$$

where $\text{Im } t \geq 0$, α is a real constant and $\alpha \geq 0$.

By taking the appropriate derivatives and interchanging the differentiation operation with the integration, it is easy to show that $\overset{+}{F}_{cw}(\alpha, t)$ satisfies the following differential equation

$$\frac{\partial^3}{\partial \alpha^3} \overset{+}{F}_{cw}(\alpha, t) + \frac{\partial}{\partial t} \overset{+}{F}_{cw}(\alpha, t) = 0 \quad (\text{D.2})$$

This differential equation with appropriate boundary conditions could be used to derive a series expansion in t or a series in α of $\overset{+}{F}_{cw}(\alpha, t)$, although this approach is not used here.

Some special values of the creeping wave time function are

$$\overset{+}{F}_{cw}(\alpha = 0, t) = \frac{\Gamma(5/6)e^{-j\pi/12}}{\pi(-jt)^{5/6}} \quad (D.3)$$

$$\left. \frac{\partial}{\partial \alpha} \overset{+}{F}_{cw}(\alpha, t) \right|_{\alpha=0} = \frac{\Gamma(7/6)e^{j\pi/12}}{\pi(-jt)^{7/6}} \quad (D.4)$$

$$\left. \frac{\partial^n}{\partial \alpha^n} \overset{+}{F}_{cw}(\alpha, t) \right|_{\alpha=0} = \frac{\Gamma\left(\frac{5+2n}{6}\right)e^{j\frac{\pi}{12}(2n-1)}}{\pi(-jt)^{\left(\frac{5+2n}{6}\right)}} \quad (D.5)$$

and

$$\overset{+}{F}_{cw}(\alpha, t = -\infty) = \overset{+}{F}_{cw}(t = \infty, \alpha) = 0 \quad (D.6)$$

Friedlander derived the following early time approximation by evaluating the inverse Laplace transform integral asymptotically [7]

$$\mathcal{L}^{-1} \left[s^{-\frac{1}{6}} e^{-\alpha s^{\frac{1}{3}}} \right] \sim \frac{\alpha^{\frac{1}{2}}}{2\sqrt{\pi}} \frac{\exp \left[-2t^{-\frac{1}{2}}(\alpha/3)^{\frac{3}{2}} \right]}{t} u(t) \quad (D.7)$$

for $t \rightarrow 0^+$, and $u(t)$ is the Heaviside unit step function. Notice that (D.7) is only valid for real time (i.e. $\text{Im } t = 0$). Because of the relationships between the Laplace transform and the Fourier transform, (D.7) is an approximation of the real part of $\overset{+}{F}_{cw}(\alpha, t)$ in (D.1). Using (D.7) it can be deduced that

$$\text{Re} \left[\overset{+}{F}_{cw}(\alpha, t) \right] \sim \frac{\alpha^{\frac{1}{2}}}{2\sqrt{\pi}} \frac{\exp \left[-2t^{-\frac{1}{2}}(\alpha/3)^{\frac{3}{2}} \right]}{t} u(t) \quad (D.8)$$

for $\text{Im } t = 0$ and $t \rightarrow 0^+$. Notice that (D.8) goes to zero as $t \rightarrow 0^+$, and in fact any order of time derivative of (D.8) goes to zero as $t \rightarrow 0^+$. Figure D.1 shows a comparison between a numerical calculation of the creeping wave time function in (D.1) and the early time asymptotic result in (D.8). Notice that only the real part of (D.1) is plotted in Figure D.1. Also notice that the peak location of the asymptotic result, which in general occurs at $t = \frac{\alpha^3}{27}$, is very close to the peak location of the exact result. The comparison in Figure D.1 is for the case of $\alpha = 1$ but the comparison is essentially the same for other values of α (except for a change in height and scale change in t) because of the scaling properties of $\overset{+}{F}_{cw}(\alpha, t)$ and the asymptotic result in (D.8).

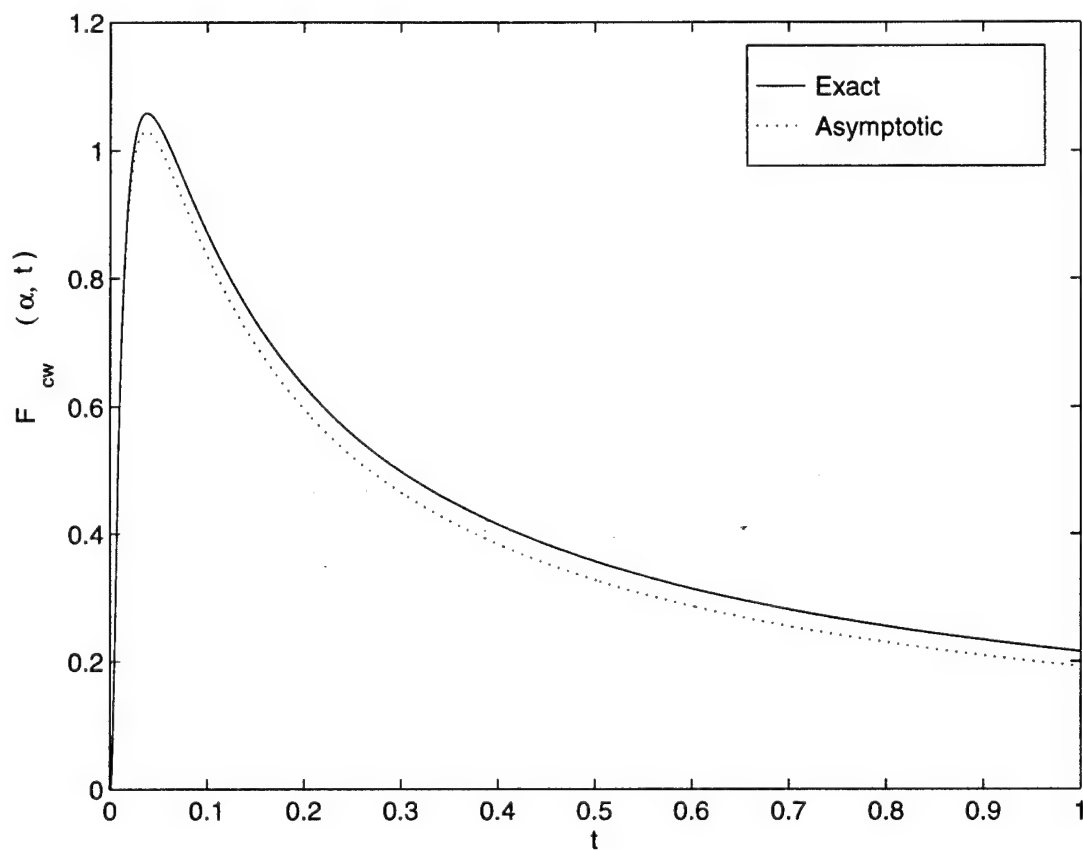


Figure D.1: Comparison between a numerical calculation of the real part of the creeping wave time function in (D.1) (“Exact”) and the asymptotic early time approximation in (D.7) (“Asymptotic”), where $\alpha = 1$.

The creeping wave time function has the following scale change properties.

$$\overset{+}{F}_{cw}(\alpha, bt) = \frac{1}{b^{5/6}} \overset{+}{F}_{cw}(\alpha/b^{1/3}, t) \quad (\text{D.9})$$

or

$$\overset{+}{F}_{cw}(b\alpha, t) = \frac{1}{b^{5/2}} \overset{+}{F}_{cw}(\alpha, t/b^3) \quad (\text{D.10})$$

where $b > 0$.

An early time power series representation for $\overset{+}{F}_{cw}(\alpha, t)$ can be derived by substituting

$$e^{j\omega t} = \sum_{n=0}^{\infty} \frac{t^n}{n!} (j\omega)^n \quad (\text{D.11})$$

into (D.1) and integrating term by term to obtain

$$\overset{+}{F}_{cw}(\alpha, t) \sim \frac{-3j}{\pi\alpha^{5/2}} \sum_{n=0}^{\infty} \frac{\Gamma(5/2 + 3n)}{n!} \left(\frac{t}{\alpha^3}\right)^n \quad (\text{D.12})$$

for $|t/\alpha^3| \rightarrow 0$. This type of early time series is sometimes called an “expansion by moments”. Notice that this series gives $\text{Re} [\overset{+}{F}_{cw}(\alpha, t)] = 0$ for $|t/\alpha^3| \rightarrow 0$. So, the series in (D.12) is only useful if $|t/\alpha^3|$ is “very small”. Also notice that this series is divergent, but it is asymptotic for $|t/\alpha^3| \rightarrow 0$. This type of asymptotic series is sometimes called “semi-convergent” [60]. The method used to obtain the asymptotic series in (D.12) is valid when all of the integrals are convergent (see page 134 in Bleistein and Handelsman’s book [31]).

A late time (or large $|t/\alpha^3|$) series representation can be derived by expanding the frequency domain function in the integrand of the transform integral of (D.1) into a low frequency series expansion and integrating term by term. This is done with the help of

$$e^{-\alpha(j\omega)^{1/3}} = \sum_{n=0}^{\infty} \frac{(-\alpha)^n}{n!} (j\omega)^{n/3} \quad (\text{D.13})$$

which is used in (D.1) to obtain

$$\overset{+}{F}_{cw}(\alpha, t) = \frac{e^{-j\frac{\pi}{12}}}{\pi(-jt)^{5/6}} \sum_{n=0}^{\infty} \frac{\Gamma(5/6 + n/3)e^{jn\frac{\pi}{6}}}{n!} \frac{(-\alpha)^n}{(-jt)^{n/3}} \quad (\text{D.14})$$

The series in (D.14) is convergent for $t \neq 0$ which can be shown with some effort by using the ratio test. From a practical stand point the series in (D.14) has good

convergence when $|t| > \alpha^3$. Note that the peak of $\text{Re} [\overset{+}{F}_{cw}(\alpha, t)]$ occurs close to $t = \alpha^3/27$, as seen in Figure D.1, which is significantly smaller than $t = \alpha^3$. So, the series in (D.14) is only useful when t is "very large".

D.2 Numerical Algorithm

This section describes an efficient algorithm which can be used to evaluate the integral in (D.1) numerically. This algorithm can theoretically be used for large or small values of $|t|$ (provided that $\text{Im } t \geq 0$). But, a more practical approach is to use the early time series in (D.12) when $|t| \ll \alpha^3/27$, use the late time series in (D.14) when $|t| \gg \alpha^3$ and use the numerical algorithm for all other $|t|$ values.

The numerical algorithm is derived by first applying a "change of variables" on the integral of (D.1). Then it is noticed that the resulting integrand contains a slowly varying factor and a rapidly varying exponential factor. So, the slowly varying factor can be approximated by a simple polynomial or series of exponentials and then the integration is performed in closed form.

The following change of variables

$$z = (j\omega)^{\frac{1}{3}} = e^{j\frac{\pi}{6}} \omega^{\frac{1}{3}} \quad (\text{D.15})$$

is used to change (D.1) into

$$\overset{+}{F}_{cw}(\alpha, t) = \frac{-3j}{\pi} \int_0^{\infty \exp(j\pi/6)} z^{\frac{3}{2}} e^{-\alpha z} e^{tz^3} dz \quad (\text{D.16})$$

Now, let

$$y = z \left(\frac{3t}{\alpha} \right)^{\frac{1}{2}} = z \left| \frac{3t}{\alpha} \right|^{\frac{1}{2}} e^{j\phi_t/2} \quad (\text{D.17})$$

where $t = |t|e^{j\phi_t}$ and $0 \leq \phi_t \leq \pi$, to change (D.16) into

$$\overset{+}{F}_{cw}(\alpha, t) = \frac{-3j\Omega^{5/2}}{\pi\alpha^{5/2}} \int_0^{\infty \exp(j\pi/6 + j\phi_t/2)} y^{3/2} \exp \left[\Omega \left(-y + \frac{1}{3}y^3 \right) \right] dy \quad (\text{D.18})$$

where

$$\Omega = \left(\frac{\alpha^3}{3t} \right)^{\frac{1}{2}} = |\Omega| e^{-j\phi_t/2} \quad (\text{D.19})$$

The integration contour of (D.18), shown in Figure D.2, lies in the valley because of

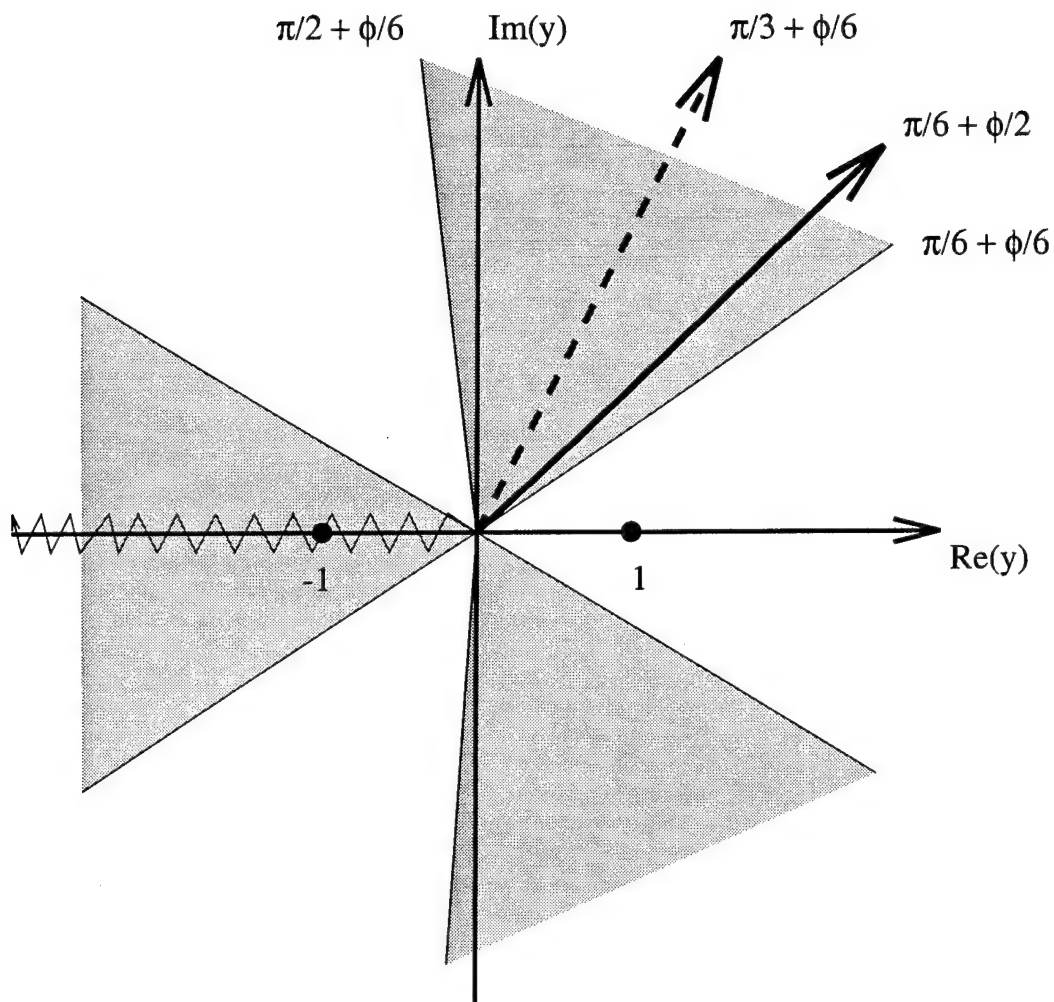


Figure D.2: The integration contour in the complex y plane. The shaded regions are valleys where the integral in (D.18) is convergent and the saddle points at $y = \pm 1$ are shown. The ϕ in this figure is the phase angle of the complex time variable $t = |t|e^{j\phi}$.

the following observation

$$\frac{\pi}{6} + \frac{\phi_t}{6} \leq \frac{\pi}{6} + \frac{\phi_t}{2} \leq \frac{\pi}{2} + \frac{\phi_t}{6} \quad (\text{D.20})$$

for $0 \leq \phi_t \leq \pi$. The integration contour in (D.18) (shown in Figure D.2 as a solid line) is shifted to a new contour (shown in Figure D.2 as a dashed line) which goes straight down the valley. This contour shift is valid, since no singularities of the integrand exist in this particular shaded valley region and the integrand decays exponentially in the valley as $|t| \rightarrow \infty$. So, the new integral expression for $\bar{F}_{cw}^+(\alpha, t)$ is

$$\bar{F}_{cw}^+(\alpha, t) = \frac{-3j\Omega^{5/2}}{\pi\alpha^{5/2}} \int_0^{\infty \exp(j\pi/3 + j\phi_t/6)} y^{3/2} \exp \left[\Omega \left(-y + \frac{1}{3}y^3 \right) \right] dy \quad (\text{D.21})$$

It is now convenient to map this contour integral such that the contour is along a real axis. This can be done by letting

$$x = y \exp(-j\pi/3 - j\phi_t/6) \quad (\text{D.22})$$

and noticing that

$$\begin{aligned} \Omega(-y + \frac{1}{3}y^3) &= |\Omega| e^{-j\phi_t/2} \left(-x e^{j\pi/3 + j\phi_t/6} - \frac{1}{3} e^{j\phi_t/2} x^3 \right) \\ &= |\Omega| \left(-x e^{j(\pi - \phi_t)/3} - \frac{1}{3} x^3 \right) \end{aligned}$$

the integral can now be written as

$$\bar{F}_{cw}^+(\alpha, t) = \frac{-3j|\Omega|^{5/2} e^{j\frac{5}{6}(\pi - \phi_t)}}{\pi\alpha^{5/2}} \bar{\mathbb{I}}^+(t) \quad (\text{D.23})$$

where

$$\bar{\mathbb{I}}^+(t) = \int_0^{\infty} x^{3/2} e^{-\frac{1}{3}|\Omega|x^3} e^{-|\Omega|Ax} dx \quad (\text{D.24})$$

and

$$A = e^{j(\pi - \phi_t)/3} \quad (\text{D.25})$$

Notice that $\text{Re}[A] \geq 0$ for $\text{Im } t \geq 0$ (or $0 \leq \phi_t \leq \pi$). Now the integral $\bar{\mathbb{I}}^+(t)$ is what must be evaluated numerically. First $\bar{\mathbb{I}}^+(t)$ is broken into two integrals

$$\bar{\mathbb{I}}^+(t) = \bar{\mathbb{I}}_1^+(t) + \bar{\mathbb{I}}_2^+(t) \quad (\text{D.26})$$

where

$$\overset{+}{I}_1(t) = \int_0^{Bx_m} x^{3/2} e^{-\frac{1}{3}|\Omega|x^3} e^{-|\Omega|Ax} dx \quad (D.27)$$

$$\overset{+}{I}_2(t) = \int_{Bx_m}^{\infty} x^{3/2} e^{-\frac{1}{3}|\Omega|x^3} e^{-|\Omega|Ax} dx \quad (D.28)$$

where

$$x_m = \left(\frac{3}{2|\Omega|} \right)^{\frac{1}{3}} \quad (D.29)$$

Notice that $x = x_m$ is the location of the maximum of $x^{3/2} e^{-\frac{1}{3}|\Omega|x^3}$ where this is considered the “slowly varying” factor in the integrand, whereas $e^{-|\Omega|Ax}$ is considered the “rapidly varying” factor in the integrand. The constant B is chosen such that the integrand of (D.24) is very small at $x = Bx_m$. This guarantees that $\overset{+}{I}_1(t)$ is the significant term in (D.26) and $\overset{+}{I}_2(t)$ is only a small correction term. The constant B is chosen to be

$$B = 2.7 \quad (D.30)$$

A different value for B could also be chosen as long as $B \gg 1$.

The $\overset{+}{I}_2(t)$ integral can be approximated by using the first term from the integration by parts procedure

$$\overset{+}{I}_2(t) \approx \frac{(Bx_m)^{\frac{3}{2}} \exp \left[-\frac{1}{3}|\Omega|(Bx_m)^3 - |\Omega|ABx_m \right]}{|\Omega|[(Bx_m)^2 + A]} \quad (D.31)$$

but $x_m = (3/2)^{1/3}|\Omega|^{-1/3}$ so

$$\overset{+}{I}_2(t) \approx \frac{(3/2)^{\frac{1}{2}} B^{\frac{2}{3}} \exp \left[-\frac{1}{2}B^3 - (3/2)^{\frac{1}{3}}|\Omega|^{\frac{2}{3}}AB \right]}{(3/2)^{\frac{2}{3}} B^2 |\Omega|^{\frac{5}{6}} + A|\Omega|^{\frac{3}{2}}} \quad (D.32)$$

The accuracy of the above equation is not critical, since $\overset{+}{I}_2(t)$ is much smaller than $\overset{+}{I}_1(t)$. Also, notice that the approximation in (D.32) improves when $|\Omega|$ increases (i.e. when t decreases).

Now all that remains is the calculation of $\overset{+}{I}_1(t)$ in (D.27). It is convenient to make another change of variables on $\overset{+}{I}_1(t)$ so that the slowly varying factor in the integrand is independent of t and α . It is very useful for the slowly varying factor to be independent of t and α because it can then be approximated by a series of simple functions just once and the integration can be performed in closed form for any values

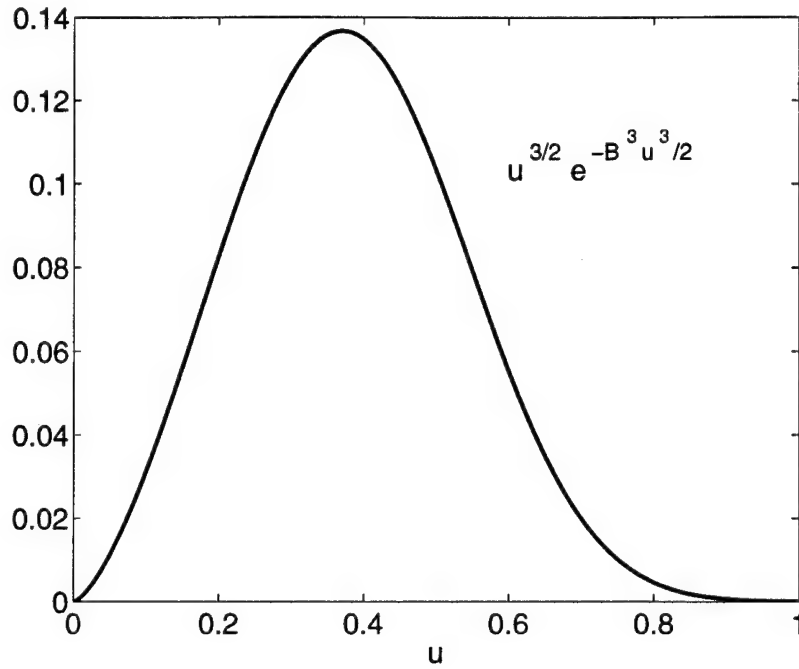


Figure D.3: The slowly varying factor in the integrand of $\dot{I}_1^+(t)$ in (D.34), where $B = 2.7$.

of t and α without finding a new approximation for the slowly varying factor. This turns out to be a very efficient method for calculating the integral $\dot{I}_1^+(t)$. So, make the following change of variables

$$u = \frac{x}{Bx_m} \quad (\text{D.33})$$

to arrive at

$$\dot{I}_1^+(t) = (Bx_m)^{\frac{5}{2}} \int_0^1 u^{\frac{3}{2}} e^{-\frac{1}{2}B^3 u^3} e^{-|\Omega|ABx_m u} du \quad (\text{D.34})$$

Notice that the slowly varying factor in the integrand $u^{\frac{3}{2}} e^{-\frac{1}{2}B^3 u^3}$ is now independent of t and α . Also, recall that the constant $B = 2.7$ is simply a fixed constant. Let the slowly varying factor in the integrand be called $g(u)$ so that

$$g(u) = u^{\frac{3}{2}} e^{-\frac{1}{2}B^3 u^3} \quad (\text{D.35})$$

Notice from Figure D.3 that $g(u)$ is a smooth and continuous function. The next step is to approximate $g(u)$ with a series of simple functions which, when substituted into (D.34), allows the integration to be done in closed form. One could achieve this by using global expansion functions defined on $u \in [0, 1]$ or by using subsectional expansion functions. The algorithm in this appendix uses global expansion functions.

Two types of approximations of $g(u)$ are now explored, one uses a polynomial and the other uses a series of exponential functions. The polynomial approximation can be easily implemented using a general least squares procedure [57]. The approximate polynomial can be written as

$$g(u) \approx \sum_{n=0}^N g_n u^n \quad (\text{D.36})$$

where the coefficients $\{g_n\}_{n=0}^N$ are found from the general least squares procedure. This is done by sampling the equation in (D.36) at many values of u , obtaining an overdetermined system of linear equations, and then solving this system of equations in a least squares sense. After (D.36) is substituted into the integral of (D.34), the integration may be done term by term to obtain the following approximation

$$\mathbb{I}_1^+(t) \approx (Bx_m)^{\frac{5}{2}} \sum_{n=0}^N g_n h_n \quad (\text{D.37})$$

where

$$h_0 = \frac{-1}{|\Omega|ABx_m} (e^{-|\Omega|ABx_m} - 1) \quad (\text{D.38})$$

$$h_n = \frac{-e^{-|\Omega|ABx_m}}{|\Omega|ABx_m} + \frac{n}{|\Omega|ABx_m} h_{n-1} \quad \text{for } n = 1 \dots N \quad (\text{D.39})$$

Although the polynomial approximation for $g(u)$ described above is straight forward, an exponential series gave better performance (i.e. the exponential series approximation for $g(u)$ is more accurate for a smaller number of terms). An exponential series approximation for $g(u)$ may be written as

$$g(u) \approx \sum_{m=1}^M g_m e^{-b_m u} \quad (\text{D.40})$$

where the parameters $\{g_m\}_{m=1}^M$ and $\{b_m\}_{m=1}^M$ can be obtained by using the extended Prony method (see page 623 in [61], or page 225 in [62]). Notice that the $\{g_m\}$ parameters here are different from the $\{g_n\}$ described earlier for the polynomial approximation. The extended Prony's method provides a very good approximation although it is not guaranteed to give a "least squares" approximation. For the problem of concern here the extended Prony's method gives an excellent approximation.

Tables D.1 and D.2 list the parameters in the exponential series approximation of

Table D.1: The exponential factors for the series of exponentials approximation to the $g(u)$ function in (D.40). These parameters are the result from using the extended Prony's method with 100 sample points.

m	Re (b_m)	Im (b_m)
1	2.492857990298293e+00	- 1.838078138920067e+01
2	2.492857990298293e+00	+ 1.838078138920067e+01
3	3.699029046816519e+00	- 1.178361372269887e+01
4	3.699029046816519e+00	+ 1.178361372269887e+01
5	4.522095825495970e+00	0
6	4.368725008737067e+00	- 5.860005489119182e+00
7	4.368725008737067e+00	+ 5.860005489119182e+00
8	6.547833511389427e+01	0
9	1.501055435645317e+02	0
10	3.732424459349517e+02	0

(D.40) when $M = 10$ and (D.40) is sampled 100 times. If one defines the relative error of the approximation as

$$\text{ERR} = \frac{\sum_{n=1}^N [g(u_n) - \sum_{m=1}^M g_m e^{-b_m u_n}]^2}{\sum_{n=1}^N [g(u_n)]^2} \quad (\text{D.41})$$

where $\{u_n\}_{n=1}^N$ are the sampled u values, then $\text{ERR} = 2.937e-9$ when the parameters in Tables D.1 and D.2 are used. Finally, substitute the approximation in (D.40) into the integral (D.34) to obtain

$$\overset{+}{I}_1(t) \approx (Bx_m)^{\frac{5}{2}} \sum_{m=1}^M g_m \left(\frac{1 - \exp(-b_m - |\Omega|ABx_m)}{b_m + |\Omega|ABx_m} \right) \quad (\text{D.42})$$

where $x_m = \left(\frac{3}{2|\Omega|}\right)^{1/3}$ and $A = \exp[j(\pi - \phi_t)/3]$.

The approximation (D.42) eventually breaks down if $|t|$ is very small or if $|t|$ is very large. So, when $|t| < 0.021(\alpha^3/40)$ use the first three terms of (D.12)

$$\overset{+}{F}_{cw}(\alpha, t) \approx \frac{-3j\Gamma(5/2)}{\pi\alpha^{5/2}} \left[1 + 39.375 \left(\frac{t}{\alpha^3}\right) + \frac{3 \cdot 5 \cdot 7 \cdots 15}{3 \cdot 2^7} \left(\frac{t}{\alpha^3}\right)^2 \right] \quad (\text{D.43})$$

Table D.2: Coefficients for the series of exponentials approximation to the $g(u)$ function in (D.40). These parameters are the result from using the extended Prony's method with 100 sample points.

m	Re (g_m)	Im (g_m)
1	-1.309449928924531e-03	- 4.143903979100756e-04
2	-1.309449928924775e-03	+ 4.143903979100027e-04
3	3.377694133016045e-02	+ 1.639435160611527e-02
4	3.377694133016031e-02	- 1.639435160611565e-02
5	3.798712810824805e-01	+ 5.480557524830053e-16
6	-2.228939771564507e-01	- 4.408366701346665e-02
7	-2.228939771564497e-01	+ 4.408366701346653e-02
8	6.785853728064312e-04	- 1.098566438683437e-15
9	2.525319404875919e-04	+ 1.430649359954744e-15
10	5.057254010578827e-05	- 5.842608514406963e-16

When $|t| > 15\alpha^3$ use the first three terms of (D.14)

$$\overset{+}{F}_{cw}(\alpha, t) \approx \frac{e^{j\pi/3}}{\pi t^{5/6}} \left[\Gamma(5/6) - \frac{\Gamma(7/6)e^{j\pi/3}\alpha}{t^{1/3}} + \frac{\Gamma(9/6)e^{j2\pi/3}\alpha^2}{2t^{2/3}} \right] \quad (D.44)$$

Figures D.4, D.5 and D.6 show the time domain creeping wave function $\overset{+}{F}_{cw}(\alpha, t)$ when $\alpha = 1$ for various time values. The function is computed using the numerical algorithm described above which uses a series of exponential functions to approximate the “slowly varying” factor in the integral. Notice that when $\overset{+}{F}_{cw}(\alpha, t)$ is plotted on a large time scale, as shown in Figure D.4, it appears to be very sharp and almost singular in nature. But when one “zooms in” on the plot of $\overset{+}{F}_{cw}(\alpha, t)$, as is done in Figure D.6, the function is seen to be smooth and continuous. In fact, the real part of $\overset{+}{F}_{cw}(\alpha, t)$ is infinitely smooth at $t \rightarrow 0$ since all of its time derivatives go to zero as explained earlier.

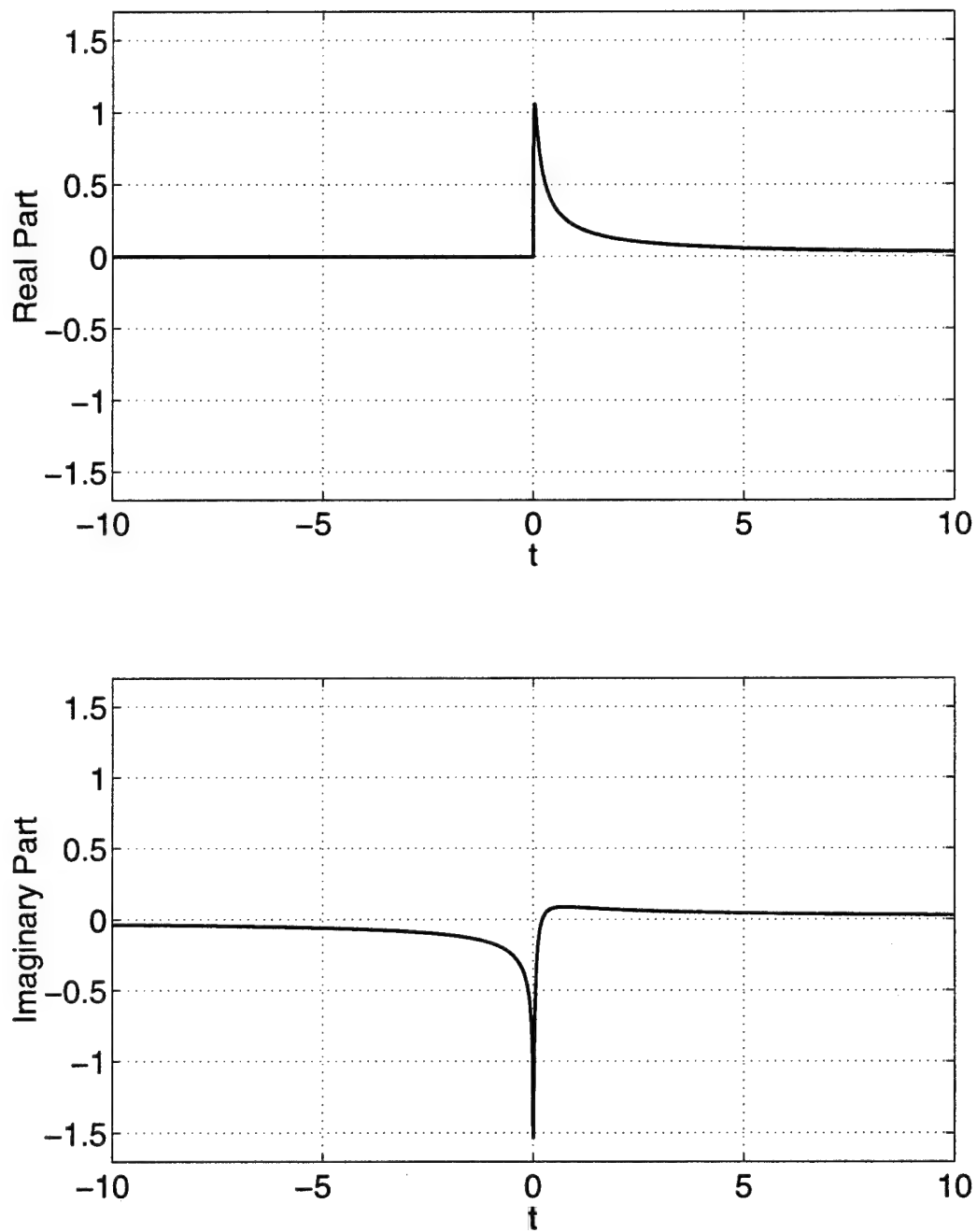


Figure D.4: The time domain creeping wave function $\bar{F}_{cw}^+(\alpha, t)$ when $\alpha = 1$, plotted for $t \in [-10, 10]$.

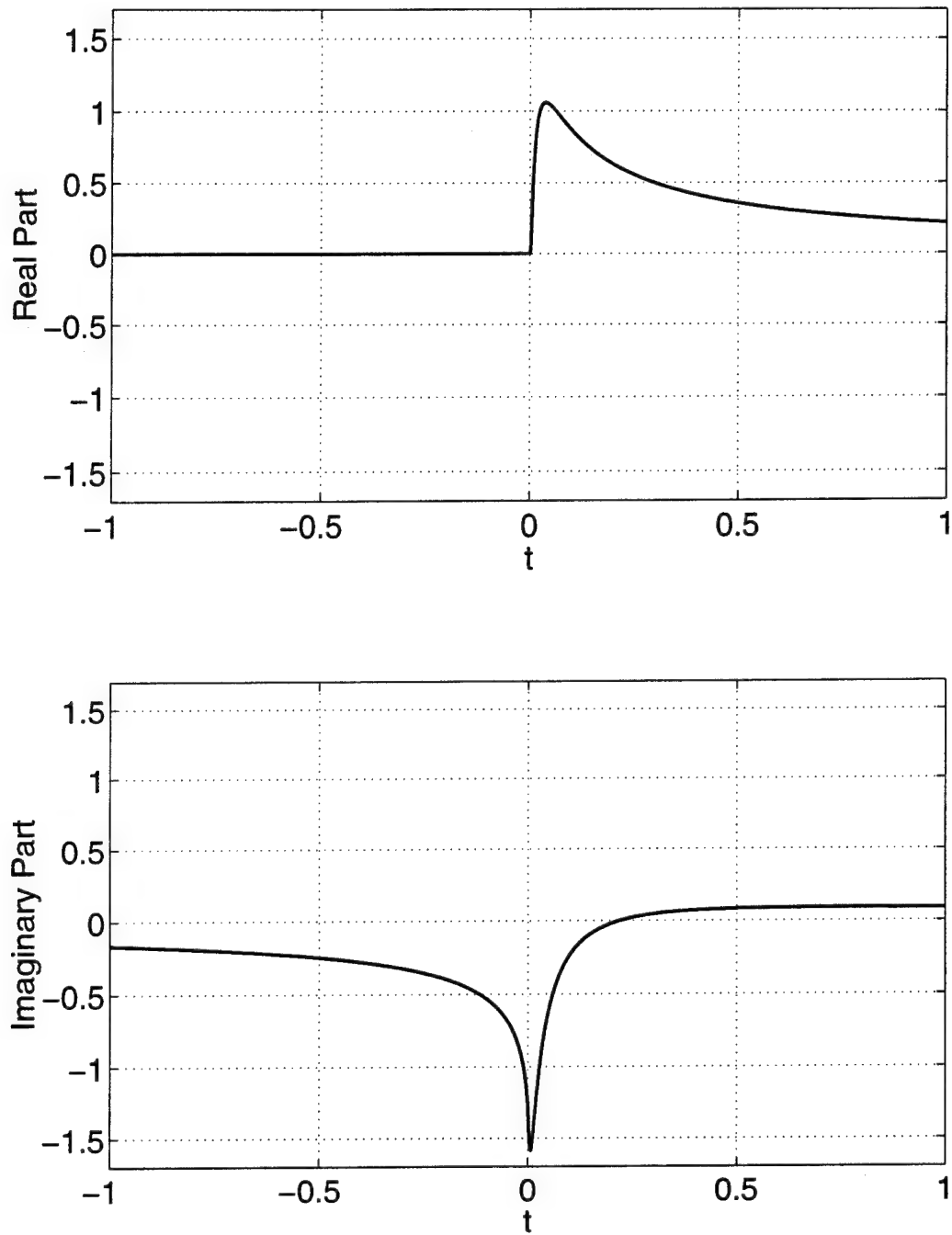


Figure D.5: The time domain creeping wave function $\hat{F}_{cw}^+(\alpha, t)$ when $\alpha = 1$, plotted for $t \in [-1, 1]$.

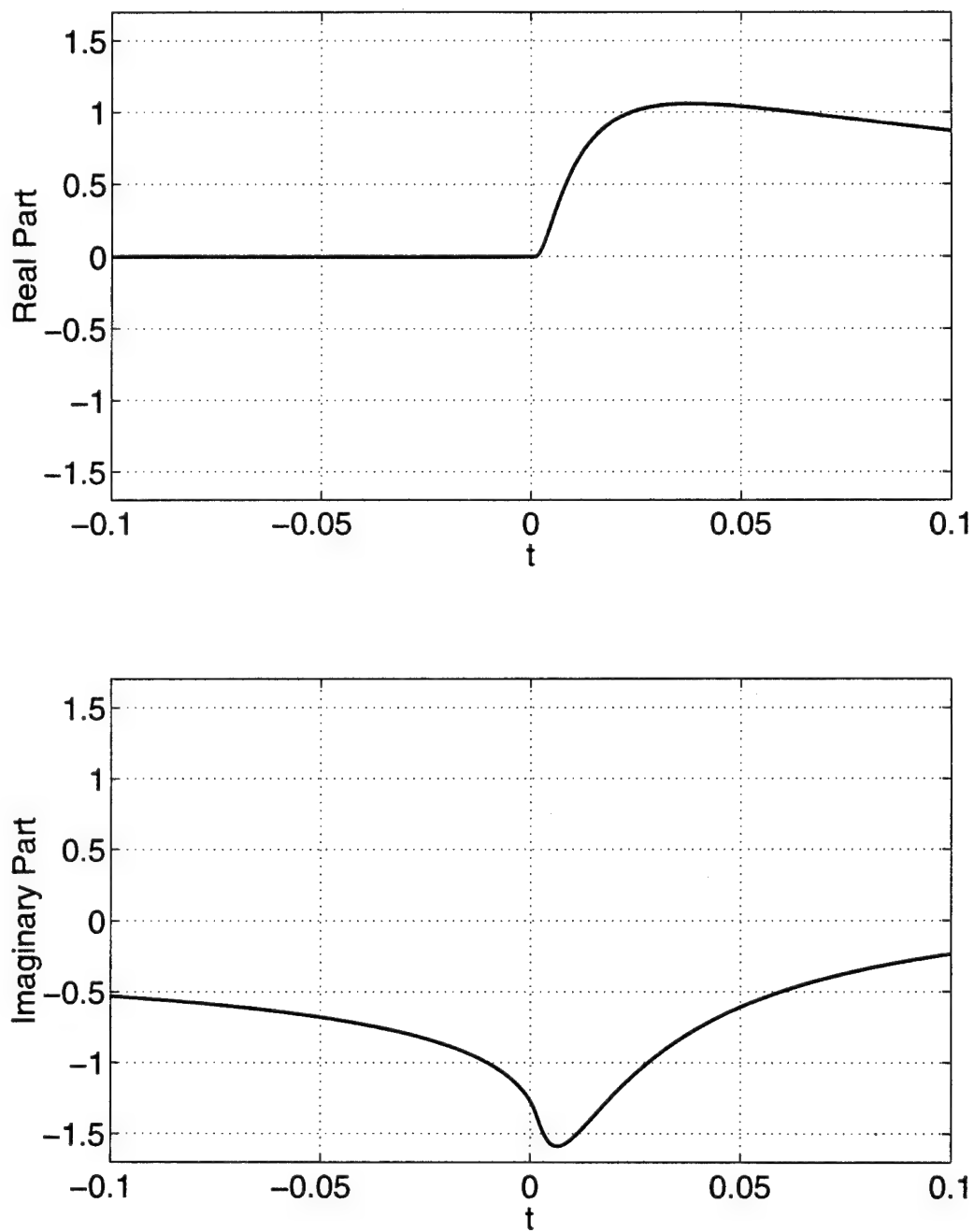


Figure D.6: The time domain creeping wave function $\dot{F}_{cw}^+(\alpha, t)$ when $\alpha = 1$, plotted for $t \in [-0.1, 0.1]$.

Appendix E

Computation of Special Function Used in TD-UTD Surface Diffraction

This appendix discusses the special function denoted by $\bar{F}_{s,h}^{+P}(\Xi, t)$ in Chapter 4 used in the TD-UTD surface diffraction coefficient. Some of the properties of this function are discussed, but more importantly, a method to compute the $\bar{F}_{s,h}^{+P}(\Xi, t)$ for complex time values t and both positive Ξ and negative Ξ values is presented.

The special function is defined as the analytic time transform (ATT) of the frequency domain Fock type function (or Pekeris's caret function) divided by $\omega^{1/6}$

$$\bar{F}_{s,h}^{+P}(\Xi, t) = \mathcal{A} \left[\frac{1}{\omega^{1/6}} \tilde{P}_{s,h}(\omega^{1/3} \Xi) \right] \quad (\text{E.1})$$

where Ξ is a parameter which depends on the source and observer locations as defined in Chapter 4. One Ξ parameter is used (instead of Ξ and Ξ^L as is in Chapter 4). If $\Xi > 0$ then it is interpreted as the shadow region parameter in (4.11), but if $\Xi < 0$ then it is interpreted as the lit region parameter Ξ^L given in (4.8). This should not cause any confusion, since this appendix is solely concerned with the computation of the function in (E.1) with little regard to its actual physical significance.

From the definition in (E.1) it can be shown that the $\bar{F}_{s,h}^{+P}(\Xi, t)$ function satisfies the following scale change property for $b > 0$

$$\bar{F}_{s,h}^{+P}(\Xi, tb) = \frac{1}{b^{5/6}} \bar{F}_{s,h}^{+P}(\Xi/b^{1/3}, t) \quad (\text{E.2})$$

or

$$\tilde{F}_{s,h}^{\pm P}(b\Xi, t) = \frac{1}{b^{5/2}} \tilde{F}_{s,h}^{\pm P}(\Xi, t/b^3) \quad (\text{E.3})$$

Notice that the above scale change property is the same as for the time domain creeping wave function $\tilde{F}_{cw}^{\pm}(\alpha, t)$ discussed in Appendix D.

E.1 Shadow Region

In the shadow region, the Ξ parameter is positive $\Xi > 0$. When the observer is deep within the shadow region (or when $\omega\Xi^3 \rightarrow \infty$), the frequency domain function of (E.1) may be written as a series of creeping wave modes

$$\frac{1}{\omega^{1/6}} \tilde{P}_{s,h}(\omega^{1/3}\Xi) \sim \begin{cases} -\frac{1}{\sqrt{\pi}} \sum_{n=1}^{N_s} \frac{1}{2[\text{Ai}'(-q_n)]^2} \frac{\exp[-(j\omega)^{1/3}\Xi q_n]}{(j\omega)^{1/6}} \\ -\frac{1}{\sqrt{\pi}} \sum_{n=1}^{N_h} \frac{1}{2\bar{q}_n[\text{Ai}(-\bar{q}_n)]^2} \frac{\exp[-(j\omega)^{1/3}\Xi \bar{q}_n]}{(j\omega)^{1/6}} \end{cases} \quad (\text{E.4})$$

This creeping wave mode series of (E.4) is asymptotically valid as $\omega\Xi^3 \rightarrow \infty$ therefore one can use (E.4) to find an expansion of the analytic time transform of (D.1) which is asymptotically valid as $|t/\Xi^3| \rightarrow 0$. The corresponding analytic time creeping wave mode series is

$$\tilde{F}_{s,h}^{\pm P}(\Xi, t) \sim \begin{cases} -\frac{1}{\sqrt{\pi}} \sum_{n=1}^{N_s} \frac{\tilde{F}_{cw}^{\pm}(\Xi q_n, t)}{2[\text{Ai}'(-q_n)]^2} \\ -\frac{1}{\sqrt{\pi}} \sum_{n=1}^{N_h} \frac{\tilde{F}_{cw}^{\pm}(\Xi \bar{q}_n, t)}{2\bar{q}_n[\text{Ai}(-\bar{q}_n)]^2} \end{cases} \quad (\text{E.5})$$

where q_n is the n^{th} zero of the Airy function, $\text{Ai}(-q_n) = 0$, and \bar{q}_n is the n^{th} zero of the derivative of the Airy function $\text{Ai}'(-\bar{q}_n) = 0$. See Table E.1 for a list of some of these roots and the associated values of the Airy function. Using the table and asymptotic formulas in (E.6) through (E.13) [29] one can continue the list in Table E.1 ad infinitum. The asymptotic formulas for the roots of the Airy function are [29]

$$q_n = f[3\pi(4n-1)/8] \quad (\text{E.6})$$

$$\bar{q}_n = g[3\pi(4n-1)/3] \quad (\text{E.7})$$

$$\text{Ai}'(-q_n) = (-1)^{n-1} f_1[3\pi(4n-1)/3] \quad (\text{E.8})$$

$$\text{Ai}(-\bar{q}_n) = (-1)^{n-1} g_1[3\pi(4n-1)/3] \quad (\text{E.9})$$

Table E.1: Zeros of the Airy function and associated values of the Airy function.

n	q_n	$\text{Ai}'(-q_n)$	\bar{q}_n	$\text{Ai}(-\bar{q}_n)$
1	2.33811	+0.70121	1.01879	+0.53566
2	4.08795	-0.80311	3.24820	-0.41902
3	5.52056	+0.86520	4.82010	+0.38041
4	6.78671	-0.91085	6.16331	-0.35791

where

$$f(z) \sim z^{2/3} \left(1 + \frac{5}{48}z^{-2} - \frac{5}{36}z^{-4} + \frac{77125}{82944}z^{-6} - \frac{108056875}{6967296}z^{-8} + \frac{162375596875}{334430208}z^{-10} \right) \quad (\text{E.10})$$

$$g(z) \sim z^{2/3} \left(1 - \frac{7}{48}z^{-2} - \frac{35}{288}z^{-4} - \frac{181223}{207360}z^{-6} + \frac{18683371}{1244160}z^{-8} - \frac{91145884361}{191102976}z^{-10} \right) \quad (\text{E.11})$$

$$f_1(z) \sim \frac{z^{1/6}}{\sqrt{\pi}} \left(1 + \frac{5}{48}z^{-2} - \frac{1525}{4608}z^{-4} + \frac{2397875}{663552}z^{-6} \right) \quad (\text{E.12})$$

$$g_1(z) \sim \frac{z^{1/6}}{\sqrt{\pi}} \left(1 - \frac{7}{96}z^{-2} - \frac{1673}{6144}z^{-4} - \frac{84394709}{26542080}z^{-6} \right) \quad (\text{E.13})$$

For observation locations near the shadow boundary (or if we let $\omega\Xi^3 \rightarrow 0$) we can use a power series representation. This is obtained by first using

$$\frac{1}{\omega^{1/6}} \tilde{P}_{s,h}(\omega^{1/3}\Xi) = \tilde{F}_{p,q}(\Xi, \omega) - \frac{1}{2\sqrt{\pi}\Xi} \frac{1}{\sqrt{j\omega}} \quad (\text{E.14})$$

where

$$\tilde{F}_{p,q}(\Xi, \omega) = \frac{e^{-j\pi/6}}{(j\omega)^{1/6}} \begin{Bmatrix} p^*(\omega^{1/3}\Xi) \\ q^*(\omega^{1/3}\Xi) \end{Bmatrix} \quad (\text{E.15})$$

Now, using the work of Logan [63] we can derive the following power series for $\tilde{F}_{p,q}(\Xi, \omega)$

$$\tilde{F}_{p,q}(\Xi, \omega) = \sum_{n=0}^{\infty} \frac{1}{n!} \begin{Bmatrix} \rho_n \\ \sigma_n \end{Bmatrix} \Xi^n (j\omega)^{(\frac{n}{3} - \frac{1}{6})} \quad (\text{E.16})$$

Table E.2: Constants used in the power series expansion of the Pekeris functions $p(x)$ and $q(x)$ and therefore also in the expansion of $\tilde{F}_{p,q}(\Xi, \omega)$ and $\tilde{F}_{p,q}^+(\Xi, t)$

n	ρ_n	σ_n
0	3.54064e-01	-3.07177e-01
1	-1.50139e-01	2.63755e-01
2	-1.91020e-02	-4.02720e-02
3	2.07797e-01	-2.52283e-01
4	-3.04017e-01	4.17454e-01
5	-1.68300e-02	-3.34820e-02
6	1.16557e+00	-1.37979e+00
7	-2.61483e+00	3.13568e+00
8	-5.03520e-02	-8.66800e-02
9	1.77043e+01	-1.99933e+01
10	-5.10111e+01	5.73522e+01
11	-3.12482e-01	-4.75105e-01
12	5.15502e+02	-5.64431e+02
13	-1.77677e+03	1.93449e+03
14	-3.27929e-01	-4.55469e+00
15	2.45097e+04	-2.62961e+04
16	-9.71193e+04	1.03833e+05
17	-5.20334e+01	-6.78254e+01
18	1.72330e+06	-1.82875e+06
19	-7.67284e+06	8.10881e+06
20	-1.16244e+03	-1.44881e+03

Table E.2: (continued)

n	ρ_n	σ_n
21	1.68425e+08	-1.73093e+08
22	-8.27602e+08	8.67552e+08
23	0.00000e+00	0.00000e+00
24	2.18280e+10	-2.23551e+10
25	-1.16876e+11	1.19558e+11
26	0.00000e+00	0.00000e+00
27	3.62274e+12	-3.69876e+11
28	-2.09315e+13	2.13544e+13
29	0.00000e+00	0.00000e+00
30	7.49321e+14	-3.87390e+14
31	-4.63552e+15	4.71980e+15
32	0.00000e+00	0.00000e+00
33	1.88985e+17	-1.69216e+17
34	-1.24387e+18	1.26448e+18
35	0.00000e+00	0.00000e+00
36	5.70892e+19	-5.79813e+19
37	-3.97672e+20	4.03714e+20
38	0.00000e+00	0.00000e+00
39	2.03497e+22	-2.06426e+22

Table E.2: (continued)

n	ρ_n	σ_n
40	-1.49357e+23	7.57602e+22
41	0.00000e+00	0.00000e+00
42	8.45181e+24	-8.65857e+24
43	-6.51126e+25	6.66674e+25
44	0.00000e+00	0.00000e+00
45	4.04588e+27	-4.13808e+27
46	-3.26101e+28	3.33365e+28
47	0.00000e+00	0.00000e+00
48	2.21139e+30	-2.25854e+30
49	-1.85943e+31	1.89825e+31

The late time expansion corresponding to the power series expansion in (E.14) and (E.16) is

$$\overset{+}{F}_{s,h}^P(\Xi, t) = \overset{+}{F}_{p,q}(\Xi, t) - \frac{e^{-j\pi/4}}{2\pi\Xi(-jt)^{1/2}} \quad (\text{E.17})$$

where

$$\overset{+}{F}_{p,q}(\Xi, t) = \frac{e^{-j\pi/12}}{\pi(-jt)^{5/6}} \sum_{n=0}^{\infty} \begin{Bmatrix} \rho_n \\ \sigma_n \end{Bmatrix} \frac{\Gamma(n/3 + 5/6)e^{jn\pi/6}}{n!} \frac{\Xi^n}{(-jt)^{n/3}} \quad (\text{E.18})$$

E.2 Lit Region

In the lit region, the parameter Ξ is negative $\Xi < 0$. In Chapter 4, the lit region parameter is denoted by Ξ^L and is defined in (4.8). Here the notation Ξ is used to denote both $\Xi > 0$ for the shadow region and $\Xi = \Xi^L < 0$ for the lit region.

For an observer in the lit region near the shadow boundary (or late time where $|t/\Xi^3| \rightarrow \infty$), one can use the power series in (E.17) and (E.18).

For an observer deep in the lit region (or for early time) where $|t/\Xi^3| \rightarrow 0$ one can use an early time asymptotic series derived from a high frequency asymptotic series

in Logan [63]. Note that the high frequency creeping wave mode expansion in (E.4) is not valid in the lit region where $\Xi < 0$. The high frequency asymptotic series valid in the lit region $\Xi < 0$ is

$$\begin{aligned} \frac{1}{\omega^{1/6}} \tilde{P}_{s,h}(\omega^{1/3}\Xi) \sim & \pm \frac{\sqrt{-\Xi}}{2} e^{-j\omega(-\Xi)^3/12} \\ & + \frac{e^{-j\omega(-\Xi)^3/12}}{2(-\Xi)^{5/2}} \sum_{n=0}^N \left\{ \begin{matrix} s_n \\ h_n \end{matrix} \right\} \frac{1}{[(-\Xi)^3 j\omega]^{n+1}} \end{aligned} \quad (\text{E.19})$$

where $\{s_n\} = \{2, -20, 560, \dots\}$ and $\{h_n\} = \{2, -28, 896, \dots\}$. Assuming that the ATT can be applied to (E.19) term-by-term (see Chapter 2) then the early time expansion for the lit region ($\Xi < 0$) is

$$\tilde{F}_{s,h}^{\pm P}(\Xi, t) \sim \pm \frac{\sqrt{-\Xi}}{2} \delta^{\pm}(\tau) + \frac{1}{2(-\Xi)^{5/2}} \sum_{n=0}^N \left\{ \begin{matrix} s_n \\ h_n \end{matrix} \right\} \tilde{H}_n^{\pm}(\Xi, \tau) \quad (\text{E.20})$$

for $|\tau/\Xi^3| \rightarrow 0$, where

$$\tau = t - (-\Xi)^3/12 \quad (\text{E.21})$$

$$\begin{aligned} \tilde{H}_n^{\pm}(\Xi, t) = & \frac{1}{2n!} \left(\frac{t}{(-\Xi)^3} \right)^n \\ & + j \frac{1}{\pi n!} \left(\frac{t}{(-\Xi)^3} \right)^n \left\{ \ln \left[-j \left(\frac{t}{(-\Xi)^3} \right) \right] - \psi(n+1) \right\} \end{aligned} \quad (\text{E.22})$$

$$\psi(1) = -\gamma \quad (\text{E.23})$$

$$\psi(n+1) = -\gamma + \sum_{m=1}^{n-1} \frac{1}{m} \quad \text{for } n > 0 \quad (\text{E.24})$$

with $\gamma = 0.5772\dots$ being Euler's constant. Notice that the expansion in (E.20) is centered at $\tau = 0$ or $t = (-\Xi)^3/12$. Because of this, the expansion in (E.20) is less useful for numerical purposes, because it is not centered at the same t value as the late time expansion in (E.18). So, an alternate early time representation may be needed.

An alternate early time expansion can be obtained by using the following power series form

$$\tilde{F}_{s,h}^{\pm P}(\Xi, t) \approx \pm \frac{\sqrt{-\Xi}}{2} \delta^{\pm}[t - (-\Xi)^3/12] + \frac{1}{(-\Xi)^{5/2}} \sum_{n=1}^N B_n^{s,h} \left(\frac{-jt}{(-\Xi)^3} \right)^{N-n} \quad (\text{E.25})$$

From the results in Chapter 2, it is known that (E.25) has the proper form for an early time representation centered at $t = 0$, the problem lies in obtaining the values of the coefficients. Notice that the early time series centered at $t = 0$ in (E.25) is an expansion of $\tilde{F}_{s,h}^{\pm P}(\Xi, t)$ minus the geometrical optics (GO) term containing the analytic delta function. This formulation is very effective since the GO term is dominant in the deep lit region (where $|[t - (-\Xi)^3]/\Xi^3| \rightarrow 0$) and the early time series in (E.25) therefore represents a remainder which becomes important for intermediate time values. Also, notice that the expansion in (E.25) explicitly satisfies the scale properties in (E.2) or (E.3). It is known by numerical experimentation that the late time series in (E.18) can be trusted (to within at least 3 significant digits) for $|t/(\Xi)^3| > 0.15$. Because of this, an approximation of the coefficients $\{B_n^{s,h}\}$ in the early time series of (E.25) is obtained by setting the early time expansion in (E.25) equal to the late time expansion in (E.17) with (E.18) at $|t/\Xi^3| = 0.15$ and $0 < \arg(t) < \pi$ in a least squares sense. This provides approximate values of the coefficients $\{B_n^{s,h}\}$ which are most accurate at $|t/\Xi^3| = 0.15$. This is very desirable, since one can use the late time series representation for $|t/\Xi^3| > 0.15$ and then switch over to the early time representation for $|t/\Xi^3| < 0.15$ without any significant discontinuities. Table E.3 lists the coefficients $\{B_n^{s,h}\}$ obtained in this least squares sense. Now, since the coefficients $\{B_n^{s,h}\}$ are obtained in this approximate manner to minimize the error at $|t/\Xi^3| = 0.15$, the early time series in (E.25) may not work as $|t/\Xi^3| \rightarrow 0$. In fact, it is known from numerical experimentation that the early time power series in (E.25) may not be accurate when $|t/\Xi^3| < 0.15$ and $\text{Im}(t/(-\Xi)^3) < 0.002$. Nonetheless, when the imaginary part of t is this small ($\text{Im}(t/(-\Xi)^3) < 0.002$) the analytic delta function (i.e. the GO term) in (E.25) is the dominant term so for practical applications this representation works quite well. On the other hand, if one is interested in computing an impulse response, where $\text{Im}(t) = 0$ it is difficult to compute the early time behavior besides the dominant impulse time function.

Table E.3: Coefficients $\{B_n^s\}$ used in the early time representation in (E.25) used in the lit region $\Xi < 0$ and for soft polarization

n	Re $[B_n^s]$	Im $[B_n^s]$
1	-2.082816029604068e+09	- 1.934225071410909e+09
2	2.231501364264926e+09	+ 2.248973125688412e+09
3	-1.252865898123653e+09	- 1.373344664977570e+09
4	4.788187068366086e+08	+ 5.744350921182956e+08
5	-1.371893503363450e+08	- 1.820181556200502e+08
6	3.078719411539325e+07	+4.590574642077959e+07
7	-5.503967634776822e+06	- 9.456164234707374e+06
8	7.803327956948597e+05	+ 1.609576880445286e+06
9	-8.475429971667759e+04	- 2.264583143400559e+05
10	6.299138967200948e+03	+ 2.600865565917071e+04
11	-1.674918333321921e+02	- 2.357302083687360e+03
12	-2.947872815842084e+01	+ 1.543029977826218e+02
13	4.483644084797442e+00	- 4.980881275349820e+00
14	-6.216333948603559e-02	- 4.140469301332007e-01

Table E.4: Coefficients $\{B_n^h\}$ used in the early time representation in (E.25) used in the lit region $\Xi < 0$ and for hard polarization

n	Re $[B_n^h]$	Im $[B_n^h]$
1	-1.145347064563553e+09	+ 2.321104859253427e+08
2	1.247217383801985e+09	- 6.159421376984853e+07
3	-7.075526321707213e+08	- 7.680045275028466e+07
4	2.716051094355760e+08	+ 7.653405928940107e+07
5	-7.758226975004484e+07	- 3.753779340973016e+07
6	1.717005587168613e+07	+ 1.266153768031792e+07
7	-2.972294299624093e+06	- 3.237541175734916e+06
8	3.933478822263941e+05	+ 6.531900019204784e+05
9	-3.619503051989348e+04	- 1.054006228018756e+05
10	1.374538560322166e+03	+ 1.350912057659442e+04
11	2.200490845152954e+02	- 1.327895365123774e+03
12	-5.070700867343560e+01	+ 9.003798728735892e+01
13	5.004751143977662e+00	- 2.421287171291755e+00
14	-7.860467067425439e-02	- 3.708472052078492e-01

E.3 Numerical Algorithm

This section presents an algorithm using the results of this appendix for the computation of the $\overset{+}{F}_{s,h}^P(\Xi, t)$ for any real value of Ξ and for any complex value of t for $\text{Im}(t) > 0$.

Before the numerical algorithm for the computation of the $\overset{+}{F}_{s,h}^P(\Xi, t)$ is presented, a small correction term for the creeping wave series of (E.5) is derived. In general, one would like to use the early time representation in (E.5) up to some time, say $|t/\Xi^3| = T_0$, and then switch over to the late time representation in (E.17) (with (E.18)) for $|t/\Xi^3| \geq T_0$. But, in order to do this the two representations (late time and early time) must overlap at $|t/\Xi^3| = T_0$ so that the resulting function does not contain a discontinuity. It is known from numerical experimentation that the creeping wave mode series of (E.5) for soft polarization is not accurate enough for large $|t/\Xi^3|$ values even when 50 creeping wave modes are included in the summation. An estimate for the infinite number of remaining creeping wave modes (from the 51st on to infinity) can be obtained as follows. First, write the following creeping wave mode summation for soft polarization as

$$S_{N_0} = \sum_{n=N_0}^{\infty} \frac{\overset{+}{F}_{cw}(\Xi q_n, t)}{2 [\text{Ai}'(-q_n)]^2} \quad (\text{E.26})$$

where $N_0 = 51$ for the numerical algorithm to be described shortly. Now, from the asymptotic formula in (E.6) with (E.10),

$$q_n \sim \left(\frac{3\pi(4n-1)}{8} \right)^{2/3} \quad (\text{E.27})$$

and for $n \geq 51$ this is accurate to five significant figures. From the asymptotic formula in (E.8) with (E.12),

$$\text{Ai}'(-q_n) \sim \frac{(-1)^{n-1}}{\sqrt{\pi}} \left(\frac{3\pi(4n-1)}{8} \right)^{1/6} \quad (\text{E.28})$$

which is accurate to six significant figures when $n \geq 51$. When $|t/\Xi^3| < 1$ and $n \geq 51$ the creeping wave mode function $\overset{+}{F}_{cw}(\alpha, t)$ may be approximated with the first term in the power series expansion of (D.12) as

$$\overset{+}{F}_{cw}(\alpha, t) \sim \frac{-3j\Gamma(5/2)}{\pi\alpha^{5/2}} \quad (\text{E.29})$$

which is accurate to within 0.1 percent. Equations (E.27), (E.28) and (E.29) can be substituted into (E.26) to obtain

$$S_{N_0} \sim \frac{-3j\Gamma(5/2)}{2\Xi^{5/2}} \left(\frac{8}{3\pi}\right)^2 \sum_{n=N_0}^{\infty} \frac{1}{(4n-1)^2} \quad (\text{E.30})$$

which is approximate for $N_0 = 51$ and asymptotically valid as $N_0 \rightarrow \infty$. The Euler-Maclaurin summation formula can be used to approximate the infinite summation in (E.30) [57].

$$\sum_{n=N_0}^{\infty} \frac{1}{(4n-1)^2} \approx \frac{1}{4(4N_0-1)} + \frac{1}{2(4N_0-1)^2} + \frac{8}{12(4N_0-1)^3} - \frac{1536}{720(4N_0-1)^5} \dots \quad (\text{E.31})$$

which gives

$$\sum_{n=51}^{\infty} \frac{1}{(4n-1)^2} \approx 1.243740E - 3 \quad (\text{E.32})$$

Finally, the infinite summation of remaining time domain creeping wave mode functions is

$$S_{N_0} \approx \frac{-j1.786878E - 3}{\Xi^{5/2}} \quad \text{for } N_0 = 51 \quad (\text{E.33})$$

Now, the numerical algorithm which can be used to compute the $\bar{F}_{s,h}^{+P}(\Xi, t)$ function is

- For observers in the shadow region, $\Xi > 0$:
 - When $|t/\Xi^3| < 1$ use the creeping wave mode summation in (E.5), with $N_h = 20$ and $N_s = 50$. Also, add the extra term in (E.33) times $(-1/\sqrt{t}\pi)$ to the creeping wave mode sum in (E.5) for the soft polarization case, approximating an infinite creeping wave mode sum.
 - When $|t/\Xi^3| \geq 1$ use the late time inverse power series in (E.17) with (E.18) including 50 terms in the series.
- For observers in the lit region, $\Xi < 0$:
 - When $|t/\Xi^3| < 0.15$ use the approximate early time representation in (E.25) including 14 terms in the power series.

- When $|t/\Xi^3| \geq 0.15$ use the late time inverse power series in (E.17) with (E.18) including 50 terms in the series.

The algorithm described above is not the most efficient method of using the equations of this Appendix, but it is robust and works well as long as $\text{Im}(t) > 0.002|\Xi^3|$. Future research can be done on more efficient representations, such as rational function approximations and so forth. The challenge of approximating the analytic time function $F_{s,h}^{+P}(\Xi, t)$ lies in the ability to compute this function for all complex time values in the upper half time plane ($\text{Im}(t) > 0$). This is a more difficult task than the more common problem of approximating a given function of a real variable.

Figures E.1 and E.2 show a comparison between the late time representation for $F_{s,h}^{+P}(\Xi, t)$ found in (E.17) and (E.18) versus the early time creeping wave mode representation for $F_{s,h}^{+P}(\Xi, t)$ found in (E.5) when the observer is in the shadow region ($\Xi > 0$). The geometry parameter Ξ is set equal to $\Xi = 1$ for Figures E.1 and E.2 without loss of generality, since a different Ξ value only causes a simple scale change as in (E.3) but leaves the comparison valid. Notice the the two representations overlap very closely, except when $|t|$ is very small such as $|t/\Xi^3| < 0.1$. Recall, in the numerical algorithm outlined earlier that, in the shadow region, the early time creeping wave mode representation of (E.5) is used for $|t/\Xi^3| < 1.0$ while the late time inverse power series of (E.17) with (E.18) is used when $|t/\Xi^3| \geq 1.0$.

Figures E.3 and E.4 show a comparison between the late time representation for $F_{s,h}^{+P}(\Xi, t)$ found in (E.17) and (E.18) versus the approximate early time power series representation in (E.25) when the observer is in the lit region ($\Xi < 0$) and the imaginary part of time is held constant at $\text{Im}(t/(-\Xi)^3) = 0.01$. The geometry parameter Ξ is set equal to $\Xi = -1$ for these figures without loss of generality, since different Ξ values simply cause a change in scale. Notice that the two representations overlap very closely when $\text{Re}(t)/(-\Xi)^3 \approx 0.15$ and more generally they overlap very closely whenever $|t/\Xi^3| = 0.15$. Also, the early time representation breaks down violently as $|t/\Xi^3| \rightarrow 0$ and the approximate early time representation breaks down as $|t/\Xi^3| \rightarrow \infty$.

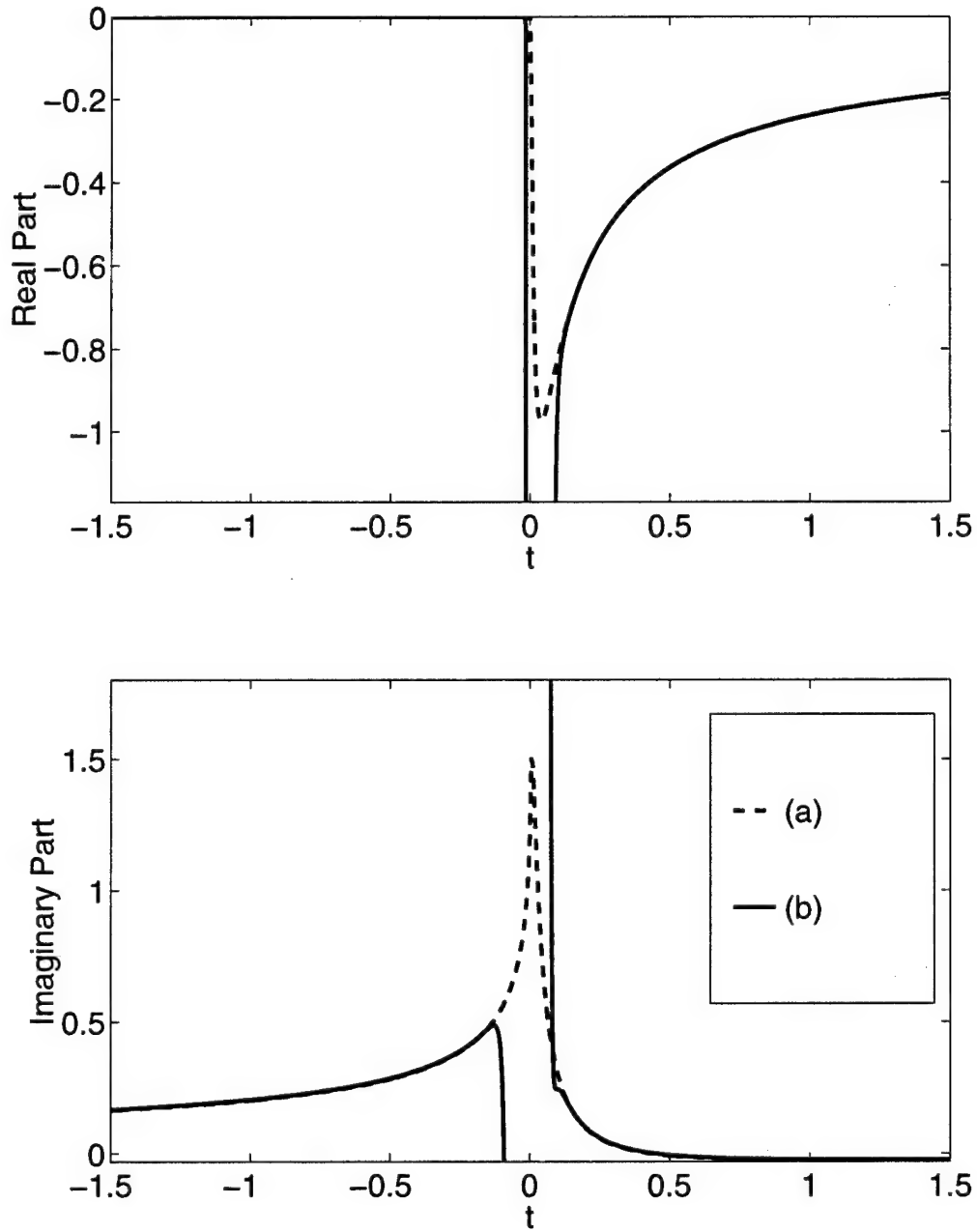


Figure E.1: The special function $\bar{F}_h^{+P}(\Xi, t)$ when the observer is in the shadow region and $\Xi = 1$. The polarization is hard. Comparison between (a) the “early time” creeping wave mode series in (E.5) and (b) the “late time” representation in (E.17) with (E.18).

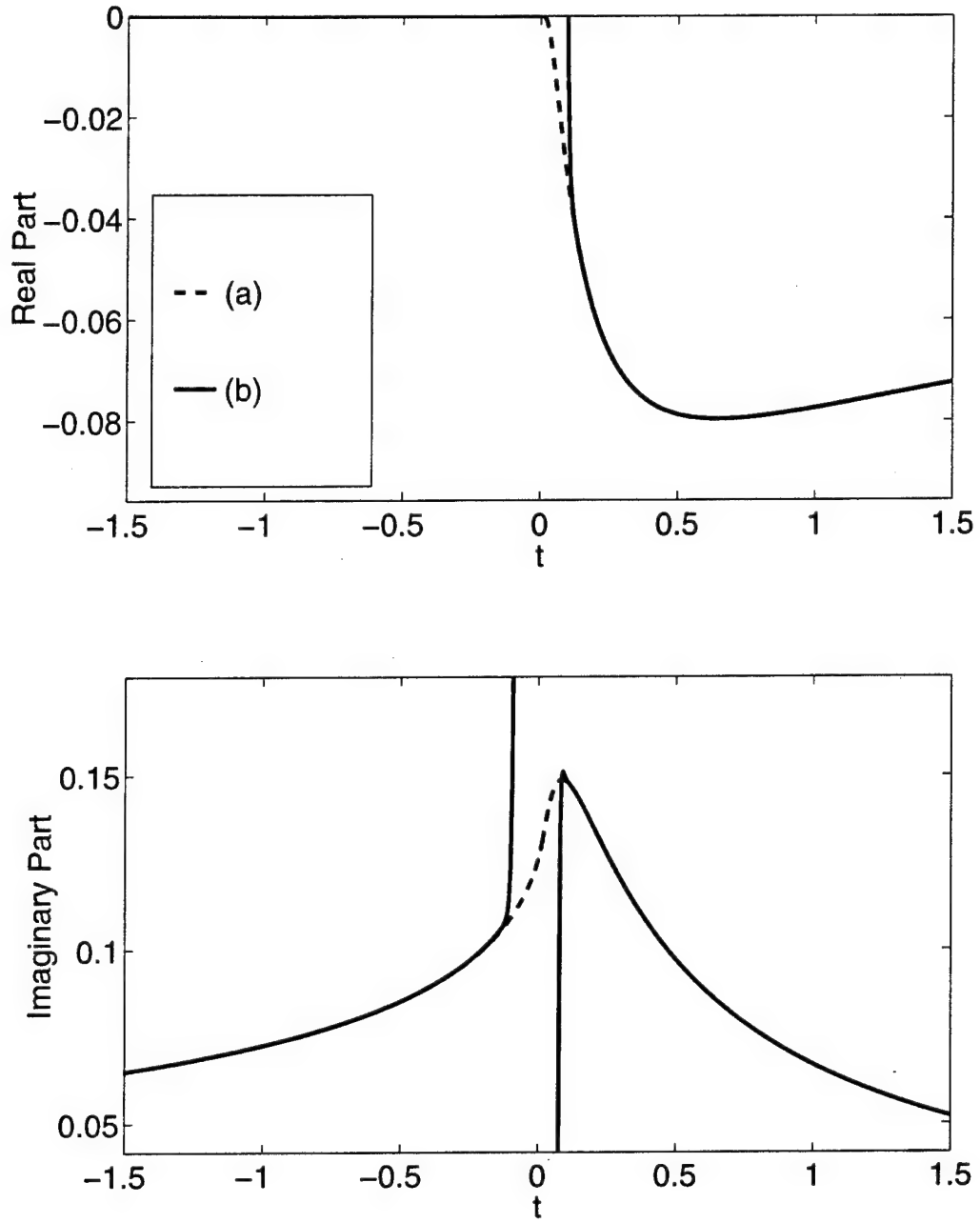


Figure E.2: The special function $\bar{F}_s^{+P}(\Xi, t)$ when the observer is in the shadow region and $\Xi = 1$. The polarization is soft. Comparison between (a) the “early time” creeping wave mode series in (E.5) (plus $-\pi^{-0.5}$ times (E.33)) and (b) the “late time” representation in (E.17) with (E.18).

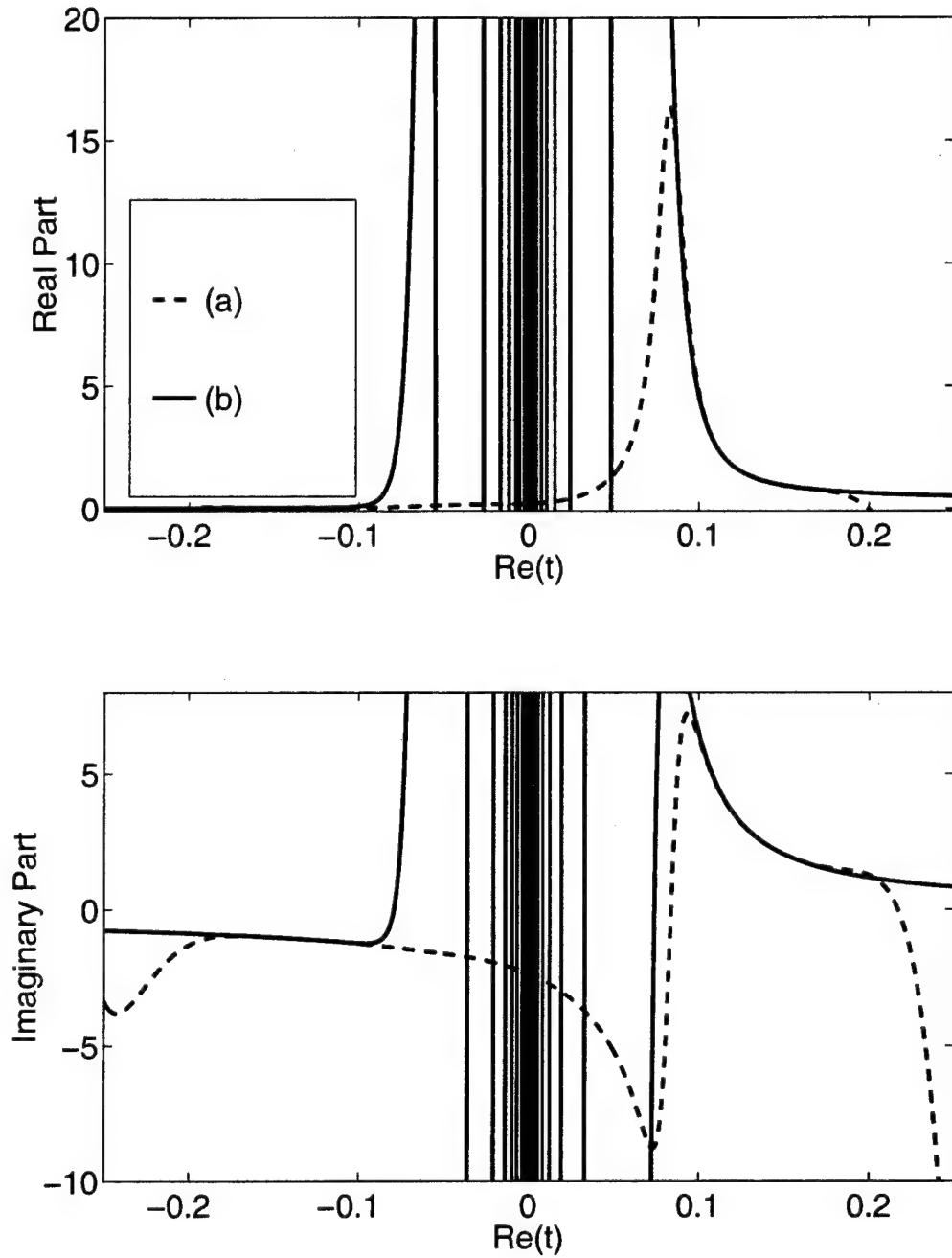


Figure E.3: The special function $F_s^{+P}(\Xi, t)$ when the observer is in the lit region and $\Xi = -1$. The polarization is soft. Comparison between (a) the “early time” representation in (E.25) and (b) the “late time” representation in (E.17) with (E.18).

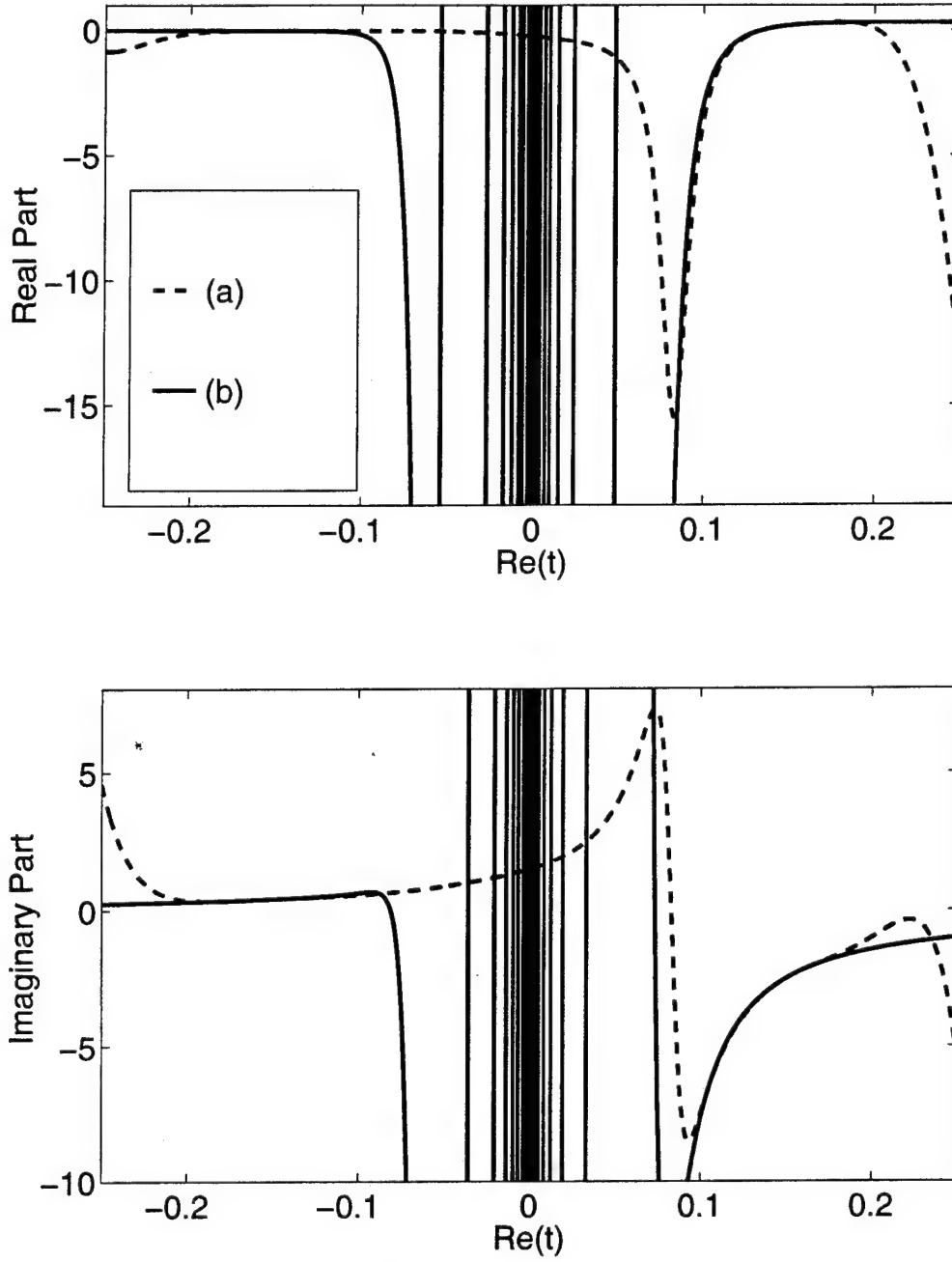


Figure E.4: The special function $F_h^{+P}(\Xi, t)$ when the observer is in the lit region and $\Xi = -1$. The polarization is hard. Comparison between (a) the “early time” representation in (E.25) and (b) the “late time” representation in (E.17) with (E.18).

Bibliography

- [1] D. L. Moffatt, "Interpretation and Application of Transient and Impulse Response Approximations in Electromagnetic Scattering Problems," Technical Report 2415-1, The Ohio State University ElectroScience Laboratory, 1968.
- [2] R. G. Kouyoumjian and P. H. Pathak, "A Uniform Geometrical Theory of Diffraction for an Edge in a Perfectly Conducting Surface," *Proc. IEEE*, vol. 62, pp. 1448-1461, November 1974.
- [3] P. H. Pathak, W. D. Burnside and R. J. Marhefka, "A Uniform GTD Analysis of the Diffraction of Electromagnetic Waves by a Smooth Convex Surface," *IEEE Trans. Antennas Propagat.*, vol. AP-28, pp. 631-642, Sept. 1980.
- [4] P. H. Pathak, "Techniques for High Frequency Problems," in *Antenna Handbook: Theory, Application and Design* (Y. T. Lo and S. W. Lee, eds.), ch. 4, Van Nostrand Reinhold Company, 1988.
- [5] L. C. Potter, D.-M. Chiang, R. Carrière and M. J. Gerry, "A GTD-Based Parametric Model for Radar Scattering," *IEEE Trans. Antennas Propagat.*, vol. 43, Oct. 1995.
- [6] M. J. Gerry and P. R. Rousseau, "TD-GTD Parametric Model for Radar Data Analysis," In preparation.
- [7] F. G. Friedlander, *Sound Pulses*. Cambridge University Press, 1958.
- [8] M. Kline and I.W. Kay, *Electromagnetic Theory and Geometrical Optics*. Interscience Publishers, 1965.
- [9] L. B. Felsen, "Propagation and Diffraction of Transient Fields in Non-Dispersive and Dispersive Media," in *Transient Electromagnetic Fields* (L. B. Felsen, ed.), Springer-Verlag, 1976.
- [10] T. Jirapunth (Veruttipong) and R. G. Kouyoumjian, "The Early-Time Responses of Currents and Charges on Wedges and Strips," in *APS Symposium Digest*, vol. 2, pp. 590-593, IEEE Antennas and Propagation Society, 1979. Presented at 1979 IEEE APS Symposium, Seattle, WA.
- [11] T. Jirapunth (Veruttipong), "The Early-Time Response of Currents and Charges Induced on Perfectly-Conducting Wedges by Transient Waves," M.S. Thesis, Dept. Elec. Eng., Ohio State Univ., Columbus, OH, 1979.

- [12] T. W. Veruttipong, "Time Domain Version of the Uniform GTD," *IEEE Trans. Antennas Propagat.*, vol. AP-38, pp. 1757-1764, November 1990.
- [13] E. Heyman and L. B. Felsen, "Nondispersive Closed Form Approximation for Transient Propagation and Scattering of Ray Fields," *Wave Motion*, vol. 7, pp. 335-358, 1985.
- [14] E. Heyman and L. B. Felsen, "Weakly Dispersive Spectral Theory of Transients (STT), Part I: Formulation and Interpretation," *IEEE Trans. Antennas Propagat.*, vol. AP-35, pp. 80-86, January 1987.
- [15] E. Heyman and L. B. Felsen, "Weakly Dispersive Spectral Theory of Transients (STT), Part II: Evaluation of the Spectral Integral," *IEEE Trans. Antennas Propagat.*, vol. AP-35, pp. 574-580, May 1987.
- [16] E. Heyman, "Weakly Dispersive Spectral Theory of Transients (STT), Part III: Applications," *IEEE Trans. Antennas Propagat.*, vol. AP-35, pp. 1258-1987, November 1987.
- [17] E. Heyman and R. Iancu, "Pulsed Field Diffraction by a Perfectly Conducting Wedge: Local Scattering Models," *IEEE Trans. Antennas Propagat.*, vol. 43, pp. 519-528, May 1995.
- [18] R. Iancu and E. Heyman, "Pulsed Field Diffraction by a Perfectly Conducting Wedge: Exact Solution," *IEEE Trans. Antennas Propagat.*, vol. 42, pp. 1377-1385, Oct. 1994.
- [19] R. Iancu and E. Heyman, "Pulsed Field Diffraction by a Perfectly Conducting Wedge: A Spectral Theory of Transients Analysis," *IEEE Trans. Antennas Propagat.*, vol. 42, pp. 781-789, June 1994.
- [20] T. Veruttipong, "Diffraction at Edges and Convex Surfaces Illuminated by Fields with a Rapid Spatial Variation," Ph.D. Dissertation, Dept. Elec. Eng., Ohio State Univ., Columbus, OH, 1982.
- [21] Y. M. Hwang and R. G. Kouyoumjian, "A Dyadic Diffraction Coefficient for an Electromagnetic Wave Which is Rapidly Varying at an Edge," USNC-URSI, 1974. Presented at the USNC-URSI Annual Meeting, Boulder, CO, October 1974.
- [22] L. B. Felsen, "Diffraction of the Pulsed Field from an Arbitrarily Oriented Electric or Magnetic Dipole by a Perfectly Conducting Wedge," *SIAM J. Appl. Math.*, vol. 26, pp. 306-312, March 1974.
- [23] A. Zemanian, *Distribution Theory and Transform Analysis*. Dover Publications, 1965.
- [24] H. Bremermann, *Distributions, Complex Variables and Fourier Transforms*. Addison-Wesley, 1965.

- [25] E. Beltrami and M. Wohlers, *Distributions and the Boundary Values of Analytic Functions*. Academic Press, 1966.
- [26] G. Doetsch, *Guide to the Applications of the Laplace and Z Transforms*. Van Nostrand Reinhold Company, 1971.
- [27] C. H. Chapman, "A New Method for Computing Synthetic Seismograms," *Geophys. J. R. Astr. Soc.*, vol. 54, pp. 481-518, 1978.
- [28] A. Erdélyi, ed., *Tables of Integral Transforms*. Bateman Manuscript Project, McGraw-Hill Book Company, Inc., 1954.
- [29] M. Abramowitz and I. A. Stegun, ed., *Handbook of Mathematical Functions*. Dover, 1972.
- [30] H. S. Carslaw and J. C. Jaeger, *Operational Methods in Applied Mathematics*. Oxford University Press, 2nd ed., 1953.
- [31] N. Bleistein and R. A. Handelsman, *Asymptotic Expansions of Integrals*. Dover, 1986. Reprint of 1975 publication by Holt, Rinehart and Winston.
- [32] M. R. Spiegel, *Laplace Transforms*. Schaum's Outline, McGraw-Hill Book Company, 1965.
- [33] S.W. Lee, V. Jamnejad and R. Mittra, "An Asymptotic Series for Early Time Response in Transient Problems," *IEEE Trans. Antennas Propagat.*, pp. 895-899, Nov. 1973.
- [34] L. B. Felsen and N. Marcuvitz, *Radiation and Scattering of Waves*. Englewood Cliffs, NJ: Prentice-Hall, 1973.
- [35] M. Lighthill, *Fourier Analysis and Generalised Functions*. Cambridge University Press, 1958.
- [36] D. S. Jones, *The Theory of Generalised Functions*. Cambridge University Press, 1982.
- [37] R. Carmichael and D. Mitrovic, *Distributions and Analytic Functions*. John Wiley and Sons, 1989.
- [38] P. H. Pathak, "High-Frequency Techniques for Antenna Analysis," *Proc. IEEE*, vol. 80, pp. 44-65, January 1992.
- [39] J. B. Keller and A. Blank, "Diffraction and Reflection of Pulses by Wedges and Corners," *Comm. Pure Appl. Math.*, vol. 4, pp. 75-94, June 1951.
- [40] K. I. Nikoskinen, M. E. Ermutlu and I. V. Lindell, "Transient Image Theory for 2-D and 3-D Conducting Wedge Problems," *IEEE Trans. Antennas Propagat.*, vol. 42, pp. 1515-1520, Nov. 1994.

- [41] D. Zheng, "A Modified Slope Diffraction for a Curved Wedge or Screen," M.S. Thesis, Dept. Elec. Eng., Ohio State Univ., Columbus, Ohio, 1985.
- [42] V. H. Weston, "Pulse Return from a Sphere," *IRE Trans. Antennas Propagat.*, vol. AP-7, pp. S43-S51, Dec. 1959.
- [43] J. R. Wait and A. M. Conda, "On the Diffraction of Electromagnetic Pulses by Curved Conducting Surfaces," *Can. J. Phys.*, vol. 37, pp. 1384-1396, 1959.
- [44] Y. M. Chen, "The Transient Behavior of Diffraction of Plane Pulse by a Circular Cylinder," *Int. J. Enging. Sci.*, vol. 2, pp. 417-429, 1964.
- [45] H. Überall, R. D. Doolittle and J. V. McNicholas, "Use of Sound Pulses for a Study of Circumferential Waves," *Journal of the Acoustical Society of America*, vol. 39, no. 3, pp. 564-578, 1966.
- [46] D. L. Moffatt, "Impulse response waveforms of a perfectly conducting right circular cylinder," *Proc. IEEE*, pp. 816-817, May 1969.
- [47] J. R. Wait, "Transient response of the penumbral currents for plane wave diffraction by a cylinder," *Canadian Journal of Physics*, vol. 47, pp. 1307-1312, 1969.
- [48] R. H. Schafer, "Transient Currents on a Perfectly Conducting Cylinder Illuminated by Unit-Step and Impulsive Plane Waves," Technical Report 2415-2, The Ohio State University ElectroScience Laboratory, 1968.
- [49] R. H. Schafer and R. G. Kouyoumjian, "Transient Currents on a Cylinder Illuminated by an Impulsive Plane Wave," *IEEE Trans. Antennas Propagat.*, vol. AP-23, pp. 627-638, Sept. 1975.
- [50] E. Heyman and L. B. Felsen, "Creeping Waves and Resonances in Transient Scattering by Smooth Convex Objects," *IEEE Trans. Antennas Propagat.*, vol. AP-31, pp. 426-437, May 1983.
- [51] J. Ma and I. R. Ciric, "Early-Time Currents Induced on a Cylinder by a Cylindrical Electromagnetic Wave," *IEEE Trans. Antennas Propagat.*, vol. 39, pp. 455-463, April 1991.
- [52] K. Naishadham and H.-W. Yao, "An Efficient Computation of Transient Scattering by a Perfectly Conducting Cylinder," *IEEE Trans. Antennas Propagat.*, vol. 41, pp. 1509-1515, Nov. 1993.
- [53] R. F. Harrington, *Time Harmonic Electromagnetic Fields*. New York, NY: McGraw-Hill, 1961.
- [54] L. G. Weiss, "Wavelets and Wideband Correlation Processing," *IEEE Signal Proc. Magazine*, pp. 13-32, Jan. 1994.
- [55] O. Rioul and M. Vetterli, "Wavelets and Signal Processing," *IEEE Signal Proc. Magazine*, Oct. 1991.

- [56] G. Kaiser, *A Friendly Guide to Wavelets*. Boston, MA: Birkhäuser, 1994.
- [57] W.H. Press, S.A. Teukolsky, W.T. Vetterling and B.P. Flannery, *Numerical Recipes in Fortran: the Art of Scientific Computing*. Cambridge University Press, 2nd ed., 1992.
- [58] J. A. Stratton, *Electromagnetic Theory*. McGraw-Hill, 1941.
- [59] C. A. Balanis, *Antenna Theory: Analysis and Design*. New York: Wiley, 1982.
- [60] A. Erdelyi, *Asymptotic Expansions*. Dover, 1956.
- [61] R. W. Hamming, *Numerical Methods for Scientists and Engineers*. Dover, 2nd ed., 1973.
- [62] S. M. Kay, *Modern Spectral Estimation*. Prentice-Hall, 1987.
- [63] N. A. Logan, "General Research in Diffraction Theory," Technical Report LMSD-288087, Lockheed Missiles and Space Division, 1959.

